

Czech Technical University in Prague
Faculty of Electrical Engineering
Department of Computer Science

Doctoral thesis

Locomotion Control and Environment Interactions Handling for Multi-legged Walking Robots

Ing. Petr Čížek

Prague, May 2023



Faculty of Electrical Engineering
Department of Computer Science

Doctoral thesis

Locomotion Control and Environment Interactions Handling for Multi-legged Walking Robots

Ing. Petr Čížek

Prague, May 2023

Supervisor: prof. Ing. Jan Faigl, Ph.D.

Ph.D. programme: Electrical Engineering and Information Technology

Branch of study: Information Science and Computer Engineering

Acknowledgements

First of all, I would like to thank my supervisor and mentor, Jan Faigl, for giving me the opportunity to do a Ph.D. at the Computational Robotics Laboratory (CRL). I would like to express my sincere thanks for his advisory, continuous support, and for providing unprecedented conditions for me to focus on what I wanted to do, which was not always in-line with my Ph.D. study. I most admire his wisdom, his attention to detail, and the high standards that he always maintains.

I would also like to thank my colleagues for the enjoyable time we spent either solving various problems, discussing more or less relevant topics, or just plainly having fun on various occasions. Big thanks goes to the administrative staff of the department for supporting our, sometimes hasty, requests.

A special thanks goes to my wife and my family for their endless tolerance and continuous support during my studies at the Czech Technical University in Prague.

During my Ph.D. studies, my work had been supported by the taxpayers of the Czech Republic through a Ph.D. scholarship. My work had been supported by the Czech Technical University grant SGS16/235/OHK3/3T/13 and by the Czech Science Foundation (GAČR) under research projects No. 15-09600Y, No. 18-18858S, and No. 21-33041J. I would also like to acknowledge the support of structural funds project CZ.02.1.01/0.0/0.0/16 019/0000765 Research Center for Informatics, and DARPA grant no. HR00112190014 - SUBTERRANEAN (SUBT) CHALLENGE - PHASE 3.

Abstract

The ability of legged robots to mimic the natural way of animal locomotion that does not rely on a continuous path of support makes them ideal candidates for performing complex tasks in a variety of different environments, including natural, urban, or industrial settings. However, the legged machines have to be able to safely interact with their surroundings and readily change their behavior based on the assigned task and given circumstances, to fully realize their potential.

This thesis addresses the development of locomotion skills for legged robots utilizing only proprioceptive sensing in explicit handling of environment interaction events. The dissertation contributes to the state of the art by formulating a model-based leg-contact detection method for anyangle tactile sensing for sensory-restricted robots utilizing the position feedback only and a model-based external wrench estimation method for continuous estimation of external wrench acting on the robot during the locomotion.

The contact detection approach utilizes a derived inverse dynamics model to monitor the joint torques and measure the virtual elasticity in the robot's kinematically controlled joints. The deviation of the set joint configuration and modeled joint configuration is used in detection of the leg contact events and further utilized in the force threshold-based locomotion controller to achieve locomotion in irregular terrains. Furthermore, we demonstrate that the approach can be adjusted to monitor the collisions of a robotic manipulator driven by stepper motors. The proposed model-based external wrench estimation method utilizes the derived whole-body dynamic model and the virtual work principle to allow continuous estimation of the ground reaction forces together with the external wrench acting on the robot.

Both methods are studied within the developed decoupled and closed-form locomotion controllers and thoroughly validated with five different multi-legged walking robots.

Keywords: Multi-legged robots, locomotion control, environment interaction, external wrench estimation

Abstrakt

Využití pohybových schopností kráčejících robotů vyžaduje schopnost bezpečně interagovat s okolím a pohotově měnit chování v závislosti na zadaném úkolu a daných okolnostech. Bezpečná fyzická interakce je základním předpokladem nasazení robotů v kolaborativních scénářích a v pracovním prostředí sdíleném s lidmi.

Tato disertační práce se zabývá zlepšením pohybových dovedností kráčejících robotů a jejich schopností interagovat s prostředím a to pouze na základě zpracování dat z proprioceptivních senzorů. Práce přispívá k dosavadnímu stavu poznání ve dvou hlavních směrech. První směr formuluje metodu detekce dotyku nohou robotu s terénem nebo překážkami pouze na základě poziční zpětné vazby z aktuátorů robotu. Metoda využívá odvozený dynamický model nohy robotu, který zachycuje i dynamiku použitých servomotorů a jejich nízkoúrovňového řízení. Porovnáním konfigurace nohy robotu ze servomotorů s konfigurací predikovanou dynamickým modelem je detekován okamžik kontaktu nohy s překážkou nebo terénem, a to v kterékoli fázi pohybu. Práce zároveň ukazuje, že metoda je dostatečně obecná na to, aby fungovala i s robotickými manipulátory, což je demonstrováno nasazením na malém robotickém ramenu poháněným krokovými motory.

Jakákoli interakce robotu s prostředím vyvolává momenty a síly působící na konstrukci robotu v místě interakce. Tyto síly mohou být pro robot očekávané, nebo neočekávané. Mezi očekávané síly patří například reakční síly působící mezi podložkou a chodidly robotu, prostřednictvím kterých se robot pohybuje. Mezi neočekávané síly patří například náraz robotu tělem do překážky. Druhým hlavním příspěvkem této práce je formulace metody pro detekci a odhadování kumulativního působení vnějších momentů a sil působících na robot. Metoda využívá formulovaný dynamický model celého robotu a princip virtuálních prací pro odhadování vnějších momentů a sil působících na robot společně s reakčními silami od podložky.

Obě metody jsou testovány v rámci dvou vyvinutých systémů pro řízení chůze robotu a nasazeny na pěti různých kráčejících robotech.

Keywords: Vícenohé kráčející roboty, řízení pohybu, interakce s prostředím, odhad vnějších momentů a sil


Contents

Acronyms	vi
Notation and Symbols	viii
1 Introduction	1
1.1 Approach, Contributions, and Thesis Organization	3
2 Multi-legged Robotic Systems	7
2.1 Overview of Multi-legged Robots	7
2.2 Developed Multi-legged Robots	17
2.3 Multi-legged Robots Locomotion Control	19
2.4 Environment Interaction Approaches	28
3 Multi-legged Robot Modeling	31
3.1 Kinematic Model	32
3.1.1 Forward Kinematics	32
3.1.2 Velocity Kinematics	34
3.1.3 Inverse Kinematics	35
3.2 Dynamic Model	36
3.2.1 Leg Dynamic Model	36
3.2.2 Actuator Dynamic Model	40
3.2.3 Whole-Body Dynamic Model	42
4 Multi-legged Locomotion Control	47
4.1 Decoupled Locomotion Controller	48
4.2 Closed-form Locomotion Controller	56
4.3 Controllers Evaluation	59
4.3.1 Body Speed Profile	60
4.3.2 Slope Adaptation	60
4.3.3 Locomotion Performance	64
5 Model-based Contact Detection	67
5.1 Position Feedback-based Terrain Sensing	67
5.1.1 Approach Limitations	74
5.2 Anyangle Contact Detection	74
5.3 Model-based Contact Detection within Locomotion Control	75
5.4 Contact Detection with Robotic Manipulator	77

6	Model-based External Wrench Estimation	83
6.1	External wrench estimation	83
6.2	Benchmarking Setup for External Wrench Estimation	84
6.3	Verification of the Dynamic Model Simplifications	85
6.4	External Wrench Estimation on the SCARAB II Robot	87
6.5	External Wrench Estimation on the HEBI Lily Robot	94
7	Conclusion & Future Directions	97
A	Experimental Platforms' Parameters	99
	List of Figures	103
	List of Tables	105
	References	106
	Author's Core Publications	106
	Author's Thesis-related Publications	106
	Author's Thesis-unrelated Publications	107
	Author's Publications in Review	109
	Cited references	109
	Citations of Author's Publications	123
	Short Biography	137

Acronyms

AHRS	Attitude and Heading Reference System
CoM	Center of Mass
CoT	Cost of Transport
CPG	Central Pattern Generator
CRL	Computational Robotics Laboratory
CTU	Czech Technical University
DARPA	Defense Advanced Research Projects Agency
DD	Direct Drive
DH	Denavit-Hartenberg
DoF	Degrees of Freedom
FKT	Forward Kinematics Task
FPGA	Field-Programmable Gate Array
FtBW	Force to Body Weight ratio
GS	Google Scholar
GRF	Ground Reaction Force
HYDR	Hydraulic Drive
IEEE	Institute of Electrical and Electronics Engineers
IKT	Inverse Kinematics Task
IMU	Inertial Measurement Unit
LA	Linear Actuation
LiDAR	Light Detection and Ranging
LRG	Large Reduction Gearbox
MPC	Model Predictive Control
RBD	Rigid Body Dynamics
PRM	Probabilistic Roadmap
QDD	Quasi-Direct Drive



RRT	Rapidly-Exploring Random Tree
SEA	Series Elastic Actuation
SLIP	Spring-Loaded Inverted Pendulum
VMC	Virtual Model Control
WBC	Whole-Body Control
WoS	Web of Science
w.r.t.	with respect to
ZMP	Zero Moment Point

Notation and Symbols

Vectors and matrices

- x, α Scalars – regular letters.
 $\mathbf{x}, \boldsymbol{\alpha}$ Vectors – bold lower case.
 \mathbf{A}, \mathbf{B} Matrices – bold upper case.

Subscripts, superscripts, and operators

- ${}^B \bullet$ Notation of reference coordinate frame.
 \bullet_b, \bullet_j Pertaining to body and joints, respectively.
 \bullet_l Pertaining to the l -th leg, $l \in \{1, \dots, 6\}$.
 $\bullet_{l,i}$ Pertaining to the l -th leg's i -th member (coxa, femur, tibia), $i \in \{c, f, t\}$.
 \bullet_M Designation of the joint actuator model related variables.
 $\bullet_x, \bullet_y, \bullet_z$ Designation of x, y, and z axis components of the vector.
 \bullet_{def} Designation of the default value of the variable.
 \bullet_{des} Designation of the immediate desired value of the variable.
 \bullet_{real} Designation of the actual measured value of the variable.
 \bullet_{est} Designation of the estimated value of the variable.
 \mathbf{x}^\times Skew-symmetric matrix representation of cross-product of vector \mathbf{x} .
 $\hat{\bullet}$ Reference (true) value of the variable.
 $\|\mathbf{x}\|$ Euclidean norm of the vector \mathbf{x} .
 $\text{Var}(\bullet)$ Variance of the variable.

System modeling

- $\theta_{l,i}$ l -th leg's i -th joint angle.
 \mathbf{q}_l Leg generalized coordinates – joint angles of l -th leg.
 $\mathbf{q}_l = [\theta_{l,c}, \theta_{l,f}, \theta_{l,t}]^T$.
 \mathbf{q}_j Joint generalized coordinates – joint angles of all the robot joints.
In case of our six-legged robot: $\mathbf{q}_j = [\mathbf{q}_1^T, \mathbf{q}_2^T, \dots, \mathbf{q}_6^T]^T$.
 \mathbf{r}_b Body position vector.
 $\boldsymbol{\Phi}$ Body orientation vector in Tait-Bryan angle representation:
 $\boldsymbol{\Phi} = [\Phi_x, \Phi_y, \Phi_z]^T$.
 \mathbf{q}_b Body generalized coordinates – position and orientation of the robot body. $\mathbf{q}_b = [\mathbf{r}_b^T, \boldsymbol{\Phi}^T]^T$.
 \mathbf{r}_l l -th leg foot-tip position vector.
 $\mathbf{r}_{c,l,i}$ l -th leg's i -th member CoM position vector.
 $\boldsymbol{\tau}_l$ l -th leg joint torques.

$\boldsymbol{\tau}_j$	All joint torques. In case of our six-legged robot: $\boldsymbol{\tau}_j = [\boldsymbol{\tau}_1^T, \boldsymbol{\tau}_2^T, \dots, \boldsymbol{\tau}_6^T]^T$.
${}^X\mathbf{T}_Y$	SE(3) transformation from coordinate frame $\{X\}$ to coordinate frame $\{Y\}$, ${}^X\mathbf{T}_Y \in \mathbb{R}^{4 \times 4}$.
${}^X\mathbf{R}_Y$	Rotation matrix part of ${}^X\mathbf{T}_Y$ transformation from coordinate frame $\{X\}$ to coordinate frame $\{Y\}$, ${}^X\mathbf{R}_Y \in \mathbb{R}^{3 \times 3}$.
\mathbf{J}_b	Body Jacobian.
\mathbf{J}_l	l -th leg Jacobian.
\mathbf{M}_b	Body inertia matrix.
$\mathbf{M}_{l,i}$	l -th leg's i -th member inertia matrix.
$\mathbf{f}_{\text{GRF},l}$	l -th leg Ground Reaction Force (GRF).
$\boldsymbol{\tau}_{e,b}$	External wrench $\boldsymbol{\tau}_{e,b} = [F_x, F_y, F_z, \tau_x, \tau_y, \tau_z]^T$.

System parameters

$a_{l,i}$	l -th leg's i -th member link length.
$\alpha_{l,i}$	l -th leg's i -th member link twist.
$d_{l,i}$	l -th leg's i -th member joint distance.
$m_{l,i}$	l -th leg's i -th member link mass.
m_b	Body mass.
\mathbf{g}	Gravitational acceleration vector. $\ \mathbf{g}\ = g = 9.81 \text{ m s}^{-2}$.

Locomotion control and sensing variables and parameters

N_{gp}	Number of gait phases in gait cycle.
T	Gait cycle period.
T_{sp}	Swing phase period.
T_{con}	Actuator control period.
\mathcal{G}	Sequence of sets of leg IDs of concurrently swinging legs. $\mathcal{G} = \{\mathcal{G}_k \mid k \in \{1, \dots, N_{\text{gp}}\}\}$
$\mathcal{G}_{\text{swing}}$	Set of actively swinging leg IDs
e_{thld}	Static error threshold for the contact detection in the position feedback-based terrain sensing approach.



Chapter 1

Introduction

“... Although we take motivation from the need to travel on rough terrain, the running experiments reported here have not yet ventured beyond our very flat laboratory floor.”

– Marc Raibert, Legged Robots that Balance, 1986

Years of technological and theoretical advancements in the research on autonomous walking machines have paved the path for the legged robots to venture out of the laboratory environment to the outside world and into practical applications, although still somewhat scarce in numbers. Motivated by the ability of the legged systems to mimic the natural way of locomotion, it remains a challenge to realize the potential and design and control the legged systems that can move autonomously and safely through the environment with similar efficiency as humans or animals.

A key feature of the legged locomotion and also its main source of complexity is its discrete nature. It allows adapting to terrain through deliberate stepping supported by single contact points, enabling operation in highly unstructured terrains. Furthermore, the legged systems do not require a continuous path of support, unlike their wheeled or tracked counterparts. They can use isolated footholds that are separated by terrain unusable to provide the robot support. It does include avoiding hazardous, unstable, or collapsible terrains, gaps, and ridges. Besides, the areas not supposed to be stepped on include plants, seedlings, or saplings in the farmlands or technological infrastructure in the factories, like cables or pipes, see Figure 1.1 for examples.

However, the legged robot interaction with the environment is not limited to the footholds, although it is the fundamental one. Especially in cluttered environments or confined spaces, the robot can interact with its environment through its whole morphology regardless of whether it bumps into obstacles, pushes through the vegetation, or squeezes through narrow passages. Further, legged robots can be an excellent choice for performing tasks in areas specifically designed for legged organisms – humans. Therefore they have to be able to safely handle the interaction with humans as well. Failing to deal with these interactions may have potentially fatal consequences. Not only it affects the robot stance and stability and may lead to permanent damage to the robot, but the robot may damage the property, or its actions may lead to injuries.

In this work, we are motivated by the need to handle the aforementioned complex interactions, which is essential for the successful deployment of the legged robots in real-world applications out of the robotic laboratories, zones of automated

1. INTRODUCTION

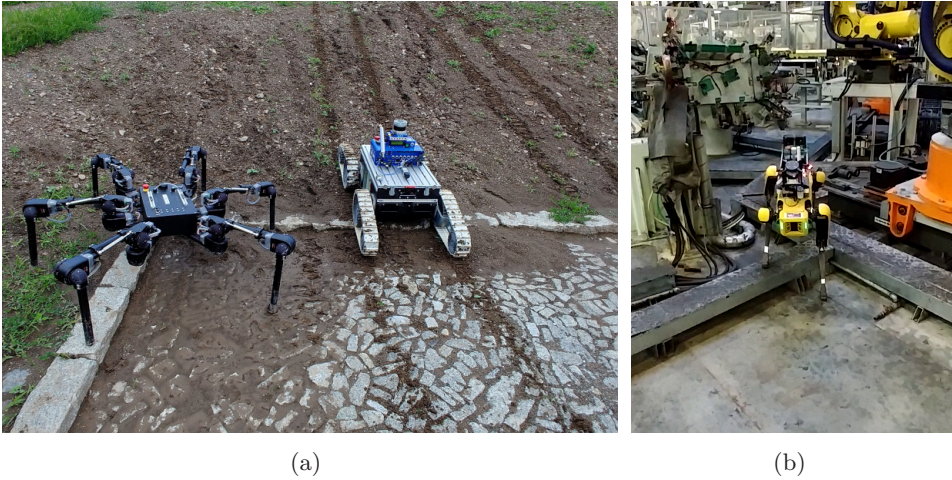


Figure 1.1: Examples of environment interactions. (a) Visibly different impact of traversing sloped muddy terrain by legged robot and tracked robot. The robots are of similar weight and traversed the muddy slope side by side once in the direction straight towards the camera. (b) Robot locomotion at automated car assembly line. The environment features number of both traversable and untraversable obstacles.

industrial plants, or closed perimeters with well-controlled operation conditions. While there is a vast diversity in source, magnitude, and effect of these interactions, they all manifest as an external wrench acting on the robot. The expected reaction of the robot also differs depending on the task at hand, ranging from dodging or avoiding obstacles, or reacting to the movement of the object during collaborative manipulation or manual guidance. While it is a common practice with multi-legged robots to incorporate the interaction handling as an implicit integral part of their control architecture, we believe that the explicit handling of these events is of particular value in environment perception and building spatial awareness of the robot surroundings and its own state. Therefore, we focus on the explicit handling of these events, which is in line with the well-established pipeline for collision detection and resolution studied within the collaborative manipulators [32].

We approach the explicit interaction handling by formulation of a model-based leg-contact detection method for anyangle tactile sensing and model-based external wrench estimation method for estimating the external forces and torques acting on the robot during the locomotion at any point of its morphology. Both of these methods are studied within the developed position-based decoupled and closed-form locomotion controllers, that utilize proprioceptive measurements from the robot joints only. It makes the methods suitable for the deployment even with less capable affordable robotic platforms using only limited sensing. In particular, we study the models and methods with six-legged crawling machines. The presented methods have been field-deployed and tested on five different multi-legged robotic

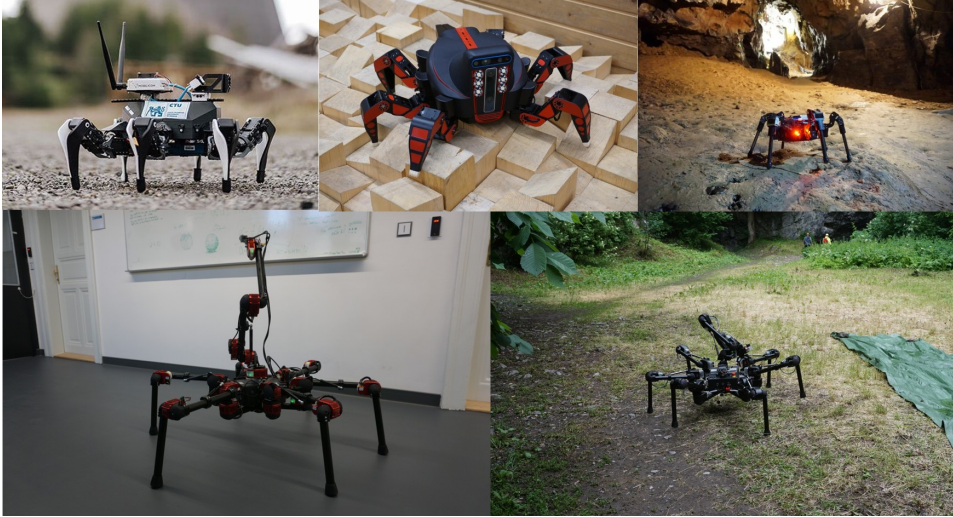


Figure 1.2: Multi-legged platforms used to verify the approaches presented in this work. From left to right, top to bottom: SCARAB I, SCARAB II, HAntR, HEBI Daisy, and HEBI Lily.

platforms, shown in Figure 1.2, from which three of them have been developed during the years of working on the topic. Although the platforms are not the main focus of the thesis, the presented results would not have been possible without this concurrent development. Besides, we further show that the developed model-based collision detection method is applicable to robotic manipulators as it shares common characteristics with the legs of legged systems.

The main goal of our work is to improve the locomotion capabilities of the multi-legged robots and allow them more complicated environment interactions by incorporating proprioceptive sensory feedback in their environment perception.

■ 1.1 Approach, Contributions, and Thesis Organization

During the Ph.D. studies the author has authored and co-authored 30 publications, which are referenced throughout the text with suffix *c* and *a* marking core publications and other author’s publications, respectively. Our work includes a number of contributions to the field of autonomous legged robot locomotion control and environment perception, including hardware-accelerated exteroceptive perception, localization and mapping, precise motion planning, and prospective research on bio-inspired neural-based locomotion control and sensing, all summarized in the author’s peer-reviewed publications. These contributions are briefly mentioned in the thesis. The core of the thesis summarizes our research and development

1. INTRODUCTION

of locomotion control and proprioceptive environment perception for multi-legged robots with the following key contributions considered.

Decoupled and closed-form locomotion controllers

We propose two kinetostatics-based approaches for blind locomotion control based on repetitive gait pattern generation to satisfy the desired input twist command. The first approach is a decoupled locomotion controller approach [1c] that utilizes projection of the leg footholds followed by the iterative body pose calculation and joint angle calculation for each leg using the inverse kinematics.

The second approach is a closed-form locomotion controller, which presents a method for the motion generation and motion control by formalizing the relationship between the leg motion and body motion into a single equation. Both of the controllers allow for seamless integration of the environmental feedback through foot-contact and external wrench sensing to support locomotion over irregular terrain and active environment interactions.

Model-based leg-contact detection

We contribute a novel model-based contact detection approach based on monitoring of virtual elasticity in joints using position feedback only. The proposed method relies on the derived leg dynamics model, including the actuator and controller model, to estimate the leg motion, which is compared with the actual configuration of the leg to detect the contact events. The method allows for the detection of tactile events anywhere along the leg morphology while it utilizes position feedback only, and thus represents a minimalistic approach to the problem applicable to a wide range of robotic platforms. We demonstrate the effectiveness of our approach on two different multi-legged platforms and also on a small robotic manipulator equipped with stepper motors.

Model-based external wrench estimation

We contribute a model-based approach for continuous explicit estimation of cumulative external wrench acting on the robot. We derive a whole-body dynamic model of the robot using the Euler-Lagrange method and by using the virtual work principle we formulate the analytical equations for estimation of Ground Reaction Force (GRF) and external wrench. As a simplification, the whole approach assumes non-sliding foot-tips and negligible centripetal and Coriolis terms of the legs dynamic model formulation due to their low velocities. A thorough experimental evaluation, including the deployment on two different multi-legged platforms, supports the feasibility of the proposed approach.

The structure of the thesis follows the individual outlined contributions, that are supported by the author’s publications, but provides additional details and results, and unifies the used mathematical notation.

First, a review of the existing multi-legged robotic platforms, their environment sensing, locomotion control approaches, and approaches to the environment interaction handling is presented in Chapter 2. Chapter 3 details the forward kinematic model, inverse kinematic model, and velocity kinematics of the robot, followed by the formulation of the developed high-fidelity dynamic model of the robot leg and the whole-body dynamic model. The proposed locomotion control approaches are described in Chapter 4, with the proposed decoupled locomotion controller described in Section 4.1 and the closed-form locomotion controller described in Section 4.2, followed by the experimental evaluation of both the controllers in Section 4.3. Chapter 5 and Chapter 6 present the proposed model-based contact detection method and the model-based external wrench estimation method together with the results of their deployment on the different multi-legged platforms, respectively. The concluding remarks and the description of possible future work directions are dedicated to Chapter 7.

1. INTRODUCTION

Chapter 2

Multi-legged Robotic Systems

Research in the domain of autonomous walking machines is a rapidly evolving field with the objective of developing intelligent and autonomous systems deployable in increasingly complex scenarios and environments. A key feature of legged robots is their ability to locomote over complex terrain. It is based on decoupling the body from environment by the legs, as the motion of the robot's body can be made largely independent of the roughness of the terrain within the kinematic limits of the articulated legs. Thus, walking systems combine complex hardware designs supported by appropriate locomotion control. This chapter gives an overview of the relevant research on multi-legged robot design, locomotion control, and environment interaction handling. First, an overview of existing multi-legged robot platforms in terms of their mechanical design is given in Section 2.1, followed by a brief description of our own developed multi-legged platforms in Section 2.2. Section 2.3 describes different approaches to locomotion control. Approaches to environment interaction handling of multi-legged platforms are described in Section 2.4.

2.1 Overview of Multi-legged Robots

In the following summary of the literature review, we do not aim to provide an exhaustive survey but rather introduce the reader to the basic characteristics, properties, and performance indicators of multi-legged robots together with the selected distinguished platforms. We outline the mechanical design factors and discuss their influence on the expected and achievable locomotion performance.

Multi-legged robots are often designed according to natural archetypes [33] and are characterized by the high number of Degrees of Freedom (DoF). The key characteristics of the multi-legged robots include the number of legs, the DoF per leg, the leg morphology, and the platform actuation principle [33], [34].

Regarding the number of legs, the current research focuses mainly on two-, four-, and six-legged robots [34] with the main difference being the required locomotion control approach to maintain the platform stability. For the legged robots, statically stable locomotion requires that the projected Center of Mass (CoM) lies within the support polygon. The support polygon is a horizontal region given as the vertical projection of the convex hull of the contact points in the direction of the gravitational acceleration vector \mathbf{g} as visualized in Figure 2.1. When the precondition for static stability is met, and the joints suddenly freeze, the robot

2. MULTI-LEGGED ROBOTIC SYSTEMS

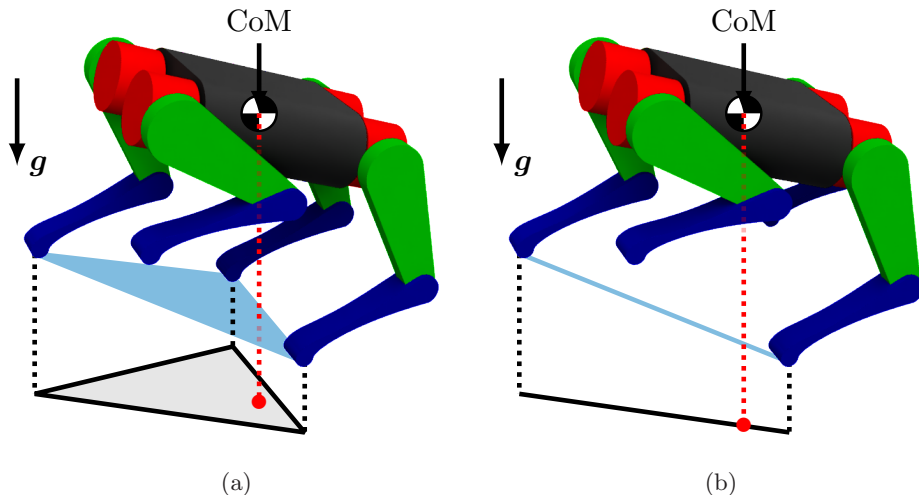


Figure 2.1: Visualization of the contact polygon (blue) and support polygon (gray) and the projection of the robot CoM (red) in the direction of the gravitational acceleration vector g for (a) the four-legged robot with single leg raised and (b) two legs raised. Note that for the example (b) the support polygon collapses to a single line.

remains statically stable. Conversely, dynamic stability requires maintaining the robot balance continuously.

Bipedal locomotion requires continuous dynamic balancing to maintain the stability of the platform. For the four-legged platforms, it depends on the number of simultaneously raised legs given by the locomotion pattern used, as shown in Figure 2.1. Six legs is the minimum number of legs for two-phase statically stable locomotion.

The number of DoF used per leg mainly influences the kinematic capabilities, the overall maneuverability of the robot [35], [36] and its ability to negotiate steep slopes [1c], [37]. Although high terrain mobility can be achieved even with a single DoF per leg, as demonstrated by the RHex family of robots [38], [39], the robot cannot rely on precise locomotion control as it cannot negotiate individual footsteps or optimize its posture. Three controllable DoF represent a good trade-off between the leg maneuverability and the overall complexity and cost of the platform. The existing platforms with three DoF per leg include four-legged research platforms Cheetah 3 [40], Spot [41], ANYmal [42], HyQ [43], and Magneto [44], as well as six-legged platforms Ambler [45], SCARAB robots [3a], [4a], Messor II [46], DLR-Crawler [47], Corin [48], Alpha [49], MORF [50], Snake Monster [51], or Lily and Daisy [52].

The platforms with three DoF per leg are only able to control the position and not the orientation of the feet, while the four-legged Pleurobot[53], or the six-

legged disaster response robot LAURON V [37], extraterrestrial Crater Explorer (CREX) [54], Crabot [55], or HAntR [1c] use four controllable DoF in leg design to increase their kinematic capabilities and terrain maneuverability. Finally, examples of the most complex multi-legged robots include Weaver [36] and Mantis [56] with five controllable DoF per leg and NASA ATHLETE [57] with seven DoF per leg.

The legged robots rely on friction between the feet and the ground to propel the robot. With a lower number of DoF, only the position of the feet is controllable and not its orientation, which is determined by the mutual position of the feet and the body. Therefore, there is an inherent twisting motion of the feet during the body motion that changes the location of the exact ground contact point, negatively influences the friction at the foothold, and thus its overall stability and reliability [58]. Pointy foot-tips or additional passive ankle joints [44], [59], [60] are used in the design of the multi-legged robots to reduce the uncertainty in the position of the actual ground contact point and to provide passive adaptation to terrain irregularities. Pointy foot-tips, further reduce the base of support, and thus the robot can generate and experience only GRF and not moments through the feet. Furthermore, several platforms use an additional controllable DoF in the body of the robot [53], [54], [56] or an actuated tail [61] to further increase the maneuverability of the robot.

In terms of leg morphology, we distinguish the bio-inspired legs, which can be further subdivided to mammalian and reptilian/arachnoid legs, and non-zoomorphic legs that include under-actuated, telescopic, or parallel-mechanism legs [33]. The mammalian legs are characterized by their position below the body (as with Cheetah 3 [40], ANYmal [42], Spot [41], or HyQReal [43] robots), which reduces the joint torques required for maintaining erected posture of the robot, and thus the power consumption of the robot. Conversely, they provide less support to the body due to the narrow posture and higher placed CoM. The reptilian (Pleurobot [62]) and arachnoid (as with SCARAB robots [3a], [4a], HAntR [1c], Magneto [44], Lauron V [37], or Mantis [56]) morphologies are characterized by a wide posture ensuring platform stability at the cost of higher joint torques and greater leg momentum, which can negatively affect the motion of the robot due to the coupling between the legs and the body of the robot. The non-zoomorphic legs utilize morphologies that do not occur naturally, including under-actuated legs with continuously revolving joints (as with the RHex family of robots [38], [39], [63]), legs with prismatic joints (as with Ambler [45], or Octopus [64]), or parallel-mechanism legs (as with Minitaur [65]). Examples of different leg morphologies are shown schematically in Figure 2.2.

Further, the shape of the robot and the orientation of the legs with respect to (w.r.t.) the body affect the directional performance of the legged robot locomotion [66] and stability margins, and characterize its maximum walking speed by limiting the leg reach [67], [68]. Legs distributed axi-symmetrically around the body with a hexagonal or circular shape, such as HAntR [1c], LEMUR [69], and Crabot [55] robots, support the mass distribution better than side-symmetrical

2. MULTI-LEGGED ROBOTIC SYSTEMS

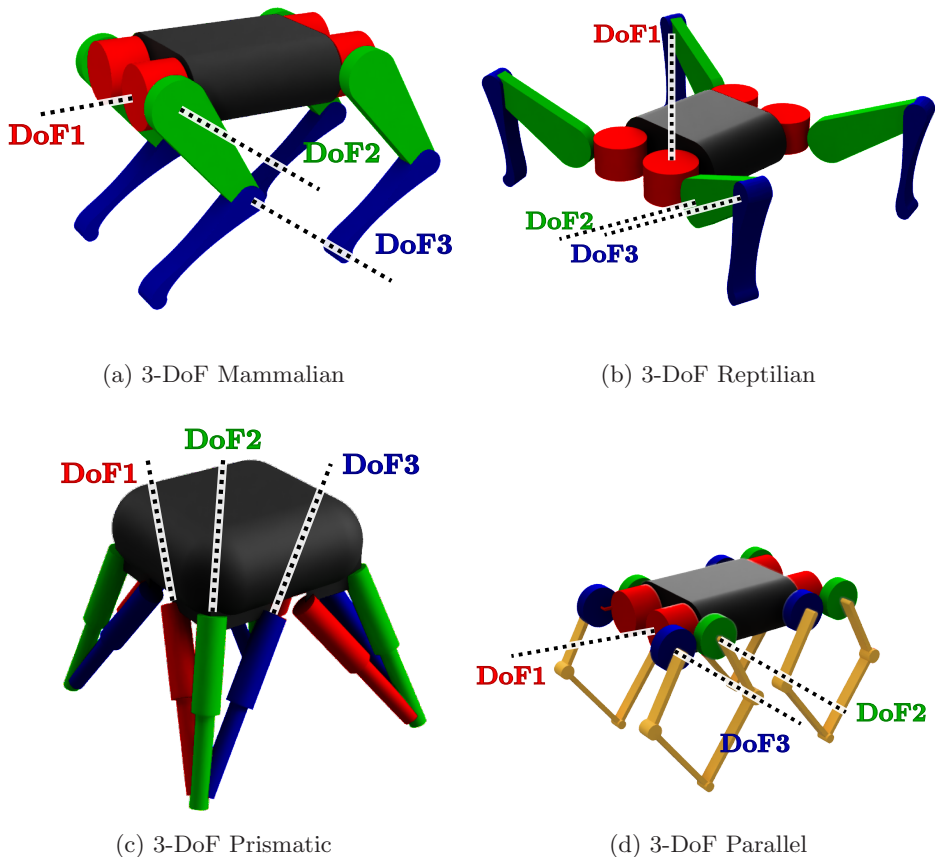


Figure 2.2: Examples of different leg morphologies with three DoF per leg.

robots of a rectangular shape [40], [45], [70]. However, the rectangular-shaped robots can exhibit relatively fast forward locomotion at the cost of reduced lateral turning flexibility [66]. Therefore, specific energy-efficient locomotion is investigated not only for walking [71], [72] but also for turning motion [73].

Existing research and commercially available walking robots range from miniature, cockroach-like robots with piezo actuators [74] up to heavy-duty robots [75], including large marine platforms for underwater inspection [76]. Hence, there is a wide variability in the used actuation principles [77], [78]. The main characteristics of actuators for legged robots are energy efficiency, output stiffness, and shock tolerance [77]. The main actuation principles can be categorized into six groups. Namely, large reduction gearbox, direct and quasi-direct drive, series elastic, linear, pneumatic, and hydraulic actuators.

The Large Reduction Gearbox (LRG) actuators with reduction ratios above 1:100 provide high torque and high output stiffness with low power requirements at the

cost of slower motion. On the other hand, the high output stiffness caused by high friction in the gearbox and high difference between the output inertia and reflected inertia makes the actuator prone to impact damage. The high reflected inertia also causes low control bandwidth as it negatively influences the torque estimates from servomotor current, and thus the ability to control output torque [77].

Direct Drive (DD) actuators and Quasi-Direct Drive (QDD) actuators are tolerant to mechanical impacts, as the motor shaft is connected to the joint either directly or through a single-stage low-ratio gearbox. They feature high torque density, and the output torque is equivalent to the regulation of the motor current [77], which makes it straightforward to control [79]. However, direct and quasi-direct drive actuators are power inefficient, require high currents [65], and have inaccurate position tracking [80].

Series Elastic Actuation (SEA) [81] adds series elasticity, such as spring, to LRG actuators. By measuring the deflection of the elastic element SEA turns torque control into position control. The elastic element can protect the gearbox from shock damage and it supports storing energy and increasing peak power while the spring and servo motor are working in the same direction. SEA represents a force-controllable actuator with low impedance and low friction, that can achieve high-quality force control [81]. The drawback of SEA is low bandwidth due to the LRG part of the actuator. Further, it needs continuous assessment of the non-linear mechanical properties of the elastic element, which are affected by many factors such as wear, current temperature, or humidity.

Pneumatically and hydraulically actuated multi-legged platforms are mechanically complex. Both require a pressure source, that can be realized by a battery powered compressor unit [77]. Pneumatic actuation is studied in context of soft robots [82]. Hydraulic actuators provide high power density and high-level force controllability when using high-frequency servo valves with precise pressure sensors. On the other hand, the main drawbacks of hydraulic actuation are the design complexity, excessive weight, increased service requirements, and virtually infinite stiffness which generates high impact loads. It is also energetically highly inefficient. Examples of hydraulically actuated legged platforms are the four-legged HyQReal [43] and BigDog [83] platforms, or Atlas [84] bipedal platform.

With the large variance in multi-legged robots construction and actuation, it is desirable to allow for comparison of their performance. Unfortunately, the performance indicators and characteristics are generally not standardized [85] as each platform is designed with different use case in mind; however, the commonly used properties are the locomotion speed, Cost of Transport (CoT) metric [86], and the Force to Body Weight ratio (FtBW) introduced by [40].

From a mechanical point of view, the locomotion speed of legged robots is mainly influenced by the maximum leg reach and the speed at which the leg can move between two footholds. The maximum leg reach is given by the leg working envelope where it does not experience self-collisions [67], which depends on the

2. MULTI-LEGGED ROBOTIC SYSTEMS

leg morphology and body shape. The leg transfer speed is influenced by the used actuators and the leg inertia given by the robot design. The leg inertia can be reduced by moving the heavy actuators closer to the robot CoM and utilizing coaxial motor design [40], pantograph legs [65], chain drive [41], or offset linear actuators [87] to actuate distant joints [77]. It reduces the impact energy loss on touchdown, but increases the complexity of the mechanical design, its manufacturing cost, and introduces possible points of failure [60], [65]. Elastic elements decouple actuators and joints, and thus make the system inherently robust to landing collisions, allow passive adaptation, and provide temporary energy storage [42], [77].

The CoT metric [86] is closely related to the locomotion speed and it is defined as the ratio between the electric input and mechanical output power of the system as

$$\text{CoT} = \frac{\bar{P}}{m g \bar{s}}, \quad (2.1)$$

where \bar{P} is the mean electrical power consumption, m is the mass of the robot, \bar{s} is the mean speed of the robot, and $g = \|\mathbf{g}\| = 9.81 \text{ ms}^{-2}$ is the gravitational constant. Note that the metric is a measure of the locomotion efficiency in a particular terrain, and therefore, it benchmarks both the platform together with the locomotion control approach in use. Therefore, multiple values of CoT depending on the terrain and employed locomotion controller can be reported [85].

The FtBW [40] is a performance indicator for highly dynamic motions. It is given as

$$\text{FtBW} = \frac{\max(F_z)}{N_l m g} \quad (2.2)$$

where $\max(F_z)$ is the maximum vertical force the robot can exert and N_l is the number of legs. It evaluates the ability of the robot to carry heavy weights or perform highly dynamic maneuvers.

Based on the review of the existing multi-legged platforms, we have selected notable and distinctive designs and robots in the similar weight and size category as our developed robots, collected their main characteristics, and listed them in Table 2.1 ordered by the number of controllable DoF of the platform and robot mass. The table also lists the actuation principle of the robot and its operating characteristics (if known). Namely the energy density calculated from the robot mass and battery capacity, the reported operating time, and the maximum locomotion speed of the platform. Figure 2.3 complements Table 2.1 and showcases selected distinctive robot designs for reference. Notable observations follow.

Among the four-legged robots, the dominant leg morphology is mammalian, and the main research focus is on fast and highly dynamic locomotion control [77], [78] supported by fast actuation and lightweight leg design. The six-legged robots typically use reptilian/arachnoid leg morphology to benefit from stable posture, and the main research focus is on deployment in rough terrains [88]. They are also slower than similarly sized four-legged platforms. Six-legged robots are also designed

with the increased number of DoF to support both rough terrain locomotion and manipulation tasks, where the static stability and locomotion of the robot remains supported by four legs, while two legs/arms are used for manipulation tasks [37], [56].

Table 2.1 shows that achieving high energy density together with high locomotion speed and long operating time is a daunting task. In this sense, the RHex family of robots [38], [63] offers the best performance; however, they feature only a single DoF per leg, which limits their deployment in rough terrains with sparse footholds.

The effects of mechanical design on robot performance can be directly compared for SCARAB II [4a] and MORF [50], and Crabot [55] and HAntR [1c] robots, which are pairs of platforms with similar size, actuators, and energy density. While SCARAB II and MORF are both designed with packed morphology, the elongated design of MORF's body allows for faster locomotion compared to SCARAB II. HAntR's packed design, with actuators concentrated towards the body, significantly improves the robot performance and operating time compared to Crabot, which has a wider default posture.

Despite its low energy density, Daisy [52] is capable of locomotion for over an hour. It is due to the additional springs at hip joints, which reduce the joint torques, and thus the energy consumption of the robot.

Finally, the ATHLETE [57] platform has actuated wheels instead of feet, that overcome the trade-off between mobility and efficiency, since the addition of wheels to the robot's legs allows moving both efficiently on flat terrains and agilely on difficult terrains. It marks a direction in legged-wheeled robot design [89].

Table 2.1: Main characteristics of selected multi-legged platforms.

Platform (N_l)	DoF [†]	Size [‡]		Mass [kg]	Actuation principle [§]	Energy density [#] [W h kg ⁻¹]	Operation time [#] [h]	Maximum speed [#] [m s ⁻¹]
		LxWxH [m]	LxWxH					
X-RHex [39] (6)	6	0.6 × 0.3 × 0.1	9.5	LRG	30.3	3.0	1.54	
AmphiHex-II [63] (6)	6	0.5 × 0.3 × 0.1	14.0	LRG	41.2	-	-	
Mimitaur [65] (4)	8	0.4 × 0.3 × 0.2	5.0	DD	18.1	0.3	1.45	
Magneto [44] (4)	12	0.6 × 0.6 × 0.3	5.5	LRG	-	-	-	
A1 [90] (4)	12	0.6 × 0.3 × 0.4	12.7	QDD	7.0	1.0	3.70	
Spot [41] (4)	12	1.1 × 0.5 × 0.7	32.0	SEA	17.6	1.5	1.60	
Cheetah 3 [40] (4)	12	0.6 × 0.3 × 0.4	45.0	QDD	10.0	~2.0	1.60	
ANYmal C [91] (4)	12	0.9 × 0.6 × 0.9	50.0	SEA	18.6	2.0	1.30	
HYQ Real [43] (4)	12	1.3 × 0.7 × 0.9	130.0	HYDR	-	2.0	1.50	
SCARAB I [3a] (6)	18	0.5 × 0.5 × 0.2	2.6	LRG	18.5	2.0	0.29	
Messor II [46] (6)	18	0.5 × 0.5 × 0.2	2.6	LRG	-	-	-	
DLR Crawler [47] (6)	18	0.5 × 0.5 × 0.2	3.5	LRG	-	-	0.20	
MORF [50] (6)	18	0.4 × 0.6 × 0.3	4.2	LRG	30.6	1.5	0.70	
Corin [48] (6)	18	0.5 × 0.6 × 0.2	4.6	LRG	-	-	0.10	
SCARAB II [4a] (6)	18	0.3 × 0.4 × 0.3	4.7	LRG	24.6	1.5	0.40	
Snake Monster [51] (6)	18	0.7 × 0.7 × 0.3	4.6	SEA	-	-	-	

Continued on next page.

Table 2.1: Main characteristics of the selected multi-legged platforms – (Continued).

Platform (N_l)	DoF [†]	Size [‡]		Mass [kg]	Actuation principle [‡]	Energy density [#] [W h kg ⁻¹]	Operation time [#] [h]	Maximum speed [#] [m s ⁻¹]
		LxWxH [m]						
Daisy [52] (6)	18	1.1 × 1.1 × 0.4	25.0	SEA	8.0	1.5	0.35	
MAX [87] (6)	18	2.4 × 2.1 × 1.5	60.0	LA,LRG	18.0	~2.0	0.12	
Ambler [45] (6)	18	4.5 × 3.0 × 6.0	2500.0	QDD,LRG	–	21.0	0.08	
HAntR [1c] (6)	24	0.5 × 0.5 × 0.3	2.9	LRG	10.6	1.0	0.43	
Crabot [55] (6)	24	0.7 × 0.7 × 0.3	3.2	LRG	9.0	0.2	0.05	
Lauron V [37] (6)	24	0.9 × 0.8 × 0.7	42.0	LRG	8.5	>2.0	–	
CREX [54] (6)	26	0.8 × 1.0 × 0.2	23.0	LA,SEA	7.7	1.3	0.17	
Pleurobot [53] (4)	27	1.4 × 0.3 × 0.2	4.0	LRG	–	–	1.60	
Weaver [36] (6)	30	0.6 × 0.6 × 0.3	7.0	LRG	16.9	~1.0	0.16	
ATHLETE [57] (6)	48	2.8 × 2.8 × 2.1	850.0	LRG	–	–	2.70	
Mantis [56] (6)	61	2.9 × 1.8 × 0.3	109.0	LA,SEA	4.1	0.7	0.98	

[†] Number of controllable DoF.

[‡] Outline of the robot when standing in the default configuration.

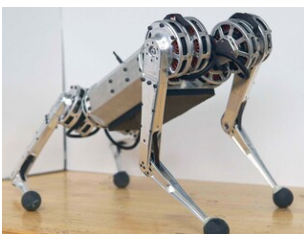
[‡] Actuation principle: LRG – large reduction gearbox, DD – direct drive, QDD – quasi-direct drive, LA – linear actuation, SEA – series elastic actuation, HYDR – hydraulic drive.

[#] Listed values (if known) are reported in the respective cited publications.

2. MULTI-LEGGED ROBOTIC SYSTEMS



(a) Minitaur [65]



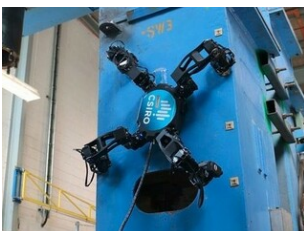
(b) Cheetah 3 [40]



(c) ANYmal C [91]



(d) HyQ Real [43]



(e) Magneto [44]



(f) Pleurobot [53]



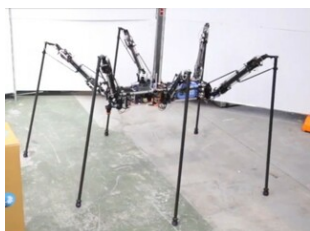
(g) X-RHex [39]



(h) Ambler [45]



(i) Octopus [64]



(j) MAX [87]



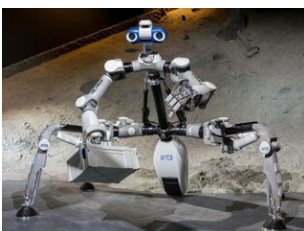
(k) Lauron V [37]



(l) Weaver [36]



(m) CREX [54]



(n) Mantis [56]



(o) ATHLETE [57]

Figure 2.3: Showcase of multi-legged robotic platforms.

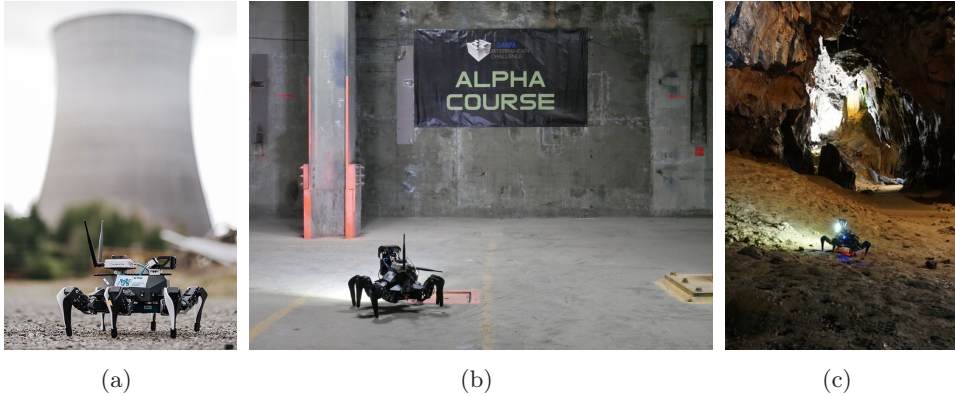


Figure 2.4: Deployments of SCARAB I robot. (a) and (b) DARPA Subterranean Challenge – Urban Circuit, Satsop, Elma, USA. (c) Bull rock cave, Czechia.

2.2 Developed Multi-legged Robots

During the work on the thesis, we have progressively developed three six-legged walking platforms over the past four years, namely, SCARAB I [3a], HAntR [1c], and SCARAB II [4a]. The platforms are briefly introduced in the following paragraphs.

The SCARAB I robot is a small six-legged walking robot with a mass of 2.6 kg and three joints per leg actuated by Dynamixel AX12-A servomotors with 4 ms control loop [5a] and position feedback only. Its design is based on the commercially available Trossen Robotics PhantomX AX robot. It has the same body dimensions, but we have modified the morphology of its legs to reduce the mass, and thus the joint torques, by 3D printing entire structure and moving the actuators closer to the robot body. We also equipped the robot with a Nvidia Tegra TX2 onboard computer to enable a fully autonomous exploration mission [10a] and we successfully deploy our exteroceptive sensor rig [92] consisting of the Intel RealSense T265 tracking camera and the Intel RealSense D435 depth camera. The robot participated in the scored runs of the DARPA Subterranean Challenge Urban Circuit (see Figure 2.4) where one unit was used as a remotely operated communication retransmission node connected by cable to the operator’s base station, and another unit was deployed in fully autonomous exploration mode. However, with its maximum locomotion speed of 0.1 ms^{-1} using the adaptive locomotion control approach [2c] it was deployed as the last system and only explored areas in the immediate vicinity of the entry gate.

HAntR represents an evolution in the robot design, surpassing its predecessor and the concurrent six-legged platforms of similar size in both endurance and locomotion capabilities [1c]. Its packed design (shown in Figure 2.5), with the actuators placed as close as possible to the CoM of the robot, allows locomoting for

2. MULTI-LEGGED ROBOTIC SYSTEMS

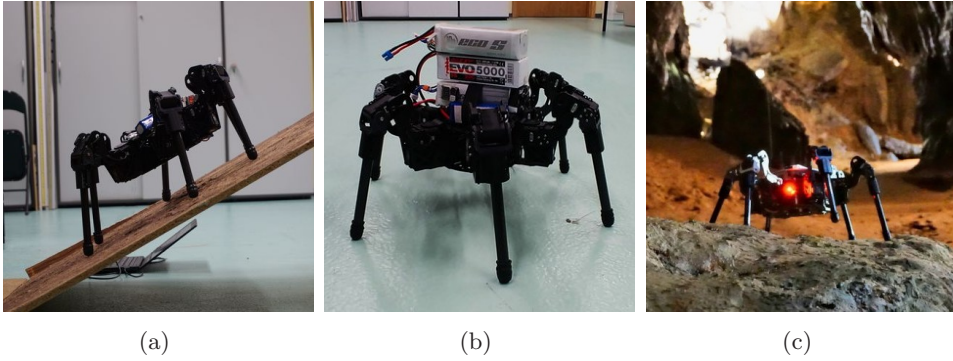


Figure 2.5: Deployments of HAntR robot. (a) Slope adaptation testing on inclined surface. (b) Endurance testing with additional payload. (c) Bull rock cave, Czechia deployment.

over an hour with a payload of 85 % of its own mass at a maximum crawling speed of 0.16 m s^{-1} over the irregular terrains using the developed locomotion controller [1c]. Additionally, its leg design features four DoF, that gives the robot enhanced motion capabilities to traverse rough terrain and negotiate steep slopes up to 31° . The robot is only 0.3 kg heavier than the SCARAB I, because it is fully 3D printed with lightweight carbon-fiber leg tibia links, despite having six additional servomotors of the same type and a battery with about 50 % larger capacity.

Finally, SCARAB II is the further evolution of our robot design that combines the lessons learned from construction of the HAntR robot with new capabilities enabled by more advanced actuators. It is a small, highly integrated, feature-rich six-legged walking robot with three joints per leg actuated by the Dynamixel XM430-W350 servomotors with instantaneous position, velocity, current, and estimated load feedback provided with the 4 ms control loop. The robot weighs 4.7 kg and is approximately 0.25 m long, 0.4 m wide, and 0.25 m height when standing in the default posture. Its monocoque chassis is completely 3D printed, and is equipped with a full featured on-board computer Intel NUC 10i7FNK with 64 GB of RAM and our exteroceptive sensor rig. Its 115.4 Wh battery provides power for more than one hour of autonomous operation.

The developed multi-legged robots are used for verification and benchmarking of the locomotion control and environment interaction approaches proposed in this thesis. Hence, their main characteristics, kinematic, and dynamic parameters are collected in Appendix A for reference.

■ 2.3 Multi-legged Robots Locomotion Control

The complex morphology of multi-legged robots needs to be supported by appropriate locomotion control to take advantage of their kinematic capabilities. In this section we outline the main principles and review existing approaches to locomotion control of legged robots.

Legged robots belong to the class of floating-base systems that are not rigidly attached to their environment and for which the body cannot be directly actuated. Therefore, legged robots are underactuated with the total DoF always higher than the number of controllable DoF. The desired body motion is generated by the reaction forces with the environment under the following constraints, which makes the legged locomotion a challenging problem [93].

- Reaction forces are generated only at the contact points and nowhere else.
- For locomotion without slipping, the locations of the contact points are immovable.
- Changing the contact point and thus repositioning the generated force requires swinging the leg to the new foothold whilst it does not significantly contribute to moving the body.
- Physically, only unilateral pushing forces can be generated, not pulling forces, making some body accelerations physically impossible.
- Tangential forces that move the body forward must not overcome the static friction and remain within the friction cone, otherwise, slippage occurs.

Thus, the locomotion of the robot is achieved by the interaction of the robot with its environment through the discrete contact points mentioned above. In legged locomotion, the feet are considered to be known contact points of GRF application at footholds.

The main goal of the locomotion control is to provide such control outputs to the actuated joints of the robot that drive the robot into the desired state. The discrete nature of the legged locomotion requires each leg alternate between the support phase, when it actively supports the mass of the robot, and the swing phase, when it is reaching a new foothold enabling another support phase. In the support phase, the legs are coupled to one another through the robot body and also through the ground forming a closed kinematic chain. During the swing phase, legs are connected to one another only through the body forming an open kinematic chain. Forces and moments transmit through these kinematic chains between the body and legs; hence, dynamic coupling exists [70].

The motion gait prescribes the order in which the swing and support phases alternate for individual legs. Hence, all the legs must work in coordination to

2. MULTI-LEGGED ROBOTIC SYSTEMS

simultaneously achieve the desired behavior. With multi-legged robots, we distinguish periodic and aperiodic motion gaits [70]. Periodic gaits alternate the leg phases periodically. They are biologically-inspired [94], [95] and include amble, walk, gallop, or trot for the four-legged platforms and pentapod, ripple, or tripod for the six-legged platforms to name a few. These gaits are most suitable for flat and irregular terrains where local optimization of footholds is sufficient to overcome the obstacles.

Periodic motion gaits are characterized by the duty factor β , which is the ratio of the support phase duration T_{support} and the whole gait cycle duration including both the swing phase and the support phase $T = T_{\text{swing}} + T_{\text{support}}$ given as

$$\beta = \frac{T_{\text{support}}}{T}. \quad (2.3)$$

Gaits with $\beta \geq 0.5$ are referred to as walking gaits, whereas gaits with $\beta < 0.5$ inherently incorporate a fly phase when no leg is touching the ground, and therefore they are referred to as running gaits.

In contrast, sparsity of suitable footholds in rough terrain necessitate their careful selection and planning. Here, it is the terrain that dictates the motion of the system. A gait-free locomotion does not rely on a prescribed order of leg swings; hence, the swinging legs are selected aperiodically according to the motion plan [57], [96], [97] or reactively based on kinematic margin [98].

Further, static gaits are characterized to be stable at any point of time and hence preferred when it comes to slow walking or challenging terrain. Also, from the theory of momentum conservation, for the robot just to maintain its body height, the total vertical impulse F_z from legs over the whole gait cycle must support the weight of the robot as

$$\int_0^T F_z dt = mgT. \quad (2.4)$$

From Equation (2.4) it can be found that the GRF increase with the decrease of the duty factor. Hence, a faster locomotion requires stronger actuation and implies increased impact forces that necessitate a high mechanical shock tolerance. Figure 2.6 illustrates the concept of the legged-locomotion control.

There are three principal layers to control a multi-legged robot: (i) motion generation, (ii) motion control, and (iii) actuator control [99], which represent a hierarchical abstraction of locomotion control. Motion generation generates the overall behavior of the system, including gait generation, foothold selection, or whole-body motion planning. Motion control translates the desired behavior into high-level actuator commands such as joint position or torque, by motion tracking of the generated commands and possibly implement reactive behaviors. Finally, actuator control regulates each joint independently, which is strongly coupled with the actuator type and robot mechatronic design. The layers can also be seen as a separation of the high-level perception and motion algorithms from low-level control and communication with different requirements on the control rate. An

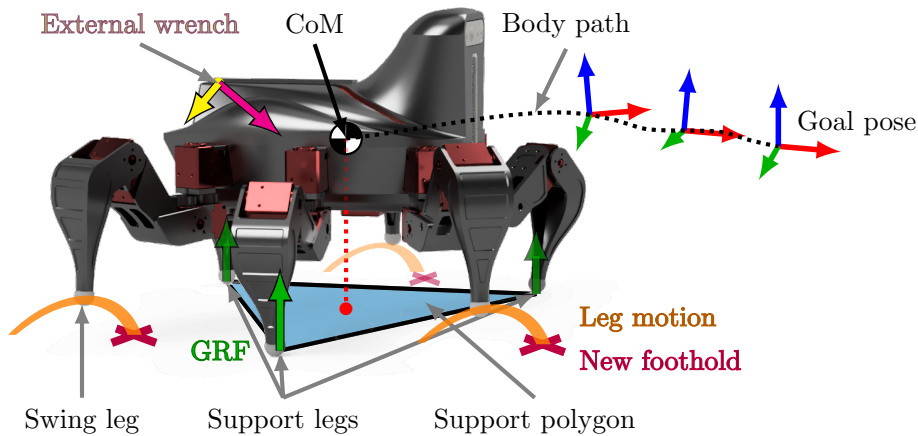


Figure 2.6: Illustration of multi-legged robot locomotion control concept. The support legs forming the support polygon hold the weight of the robot body and propel the robot through the action of GRF, while the swinging legs are moving to new footholds. The goal pose prescribes the desired position and orientation w.r.t. the inertial frame.

overview of the components of the multi-layered locomotion control architecture for electrically actuated multi-legged robots is shown schematically in Figure 2.7.

Motion control strategies [101] include force control [42], [58], impedance control [67], or position control [1c], [2c], but it is also possible to combine different control strategies for different locomotion phases. For example in [79], the authors use impedance control for leg swing phase and force control for stance. The force control methods control the contact forces directly; however, force control behaves poorly when the robot legs are not in contact with the ground, as it can lead to rapid movements followed by large impact forces at foot-strike. Impedance control methods [102] control the ratio of the force output to motion input, allowing the robot to behave like mechanical impedance with virtual damping and stiffness of the system. However, both these methods require either a force sensor at each joint or a predictable relationship between the contact forces and joint torques [77], [102]. These conditions can be met relatively easily by robots with DD or QDD actuators [79]. High forces can be applied by position control methods, as they try to reach the commanded position at all costs [77]. Such excessive forces negatively affect the robot posture and consequently increase load and wear on the joint actuators, which can lead to permanent robot damage.

An open-loop motion control is sufficient for locomotion on flat surfaces and for robots with low output stiffness and high shock tolerance [38]. However, on irregular and rough terrains, finer closed-loop motion control with interaction handling including foot-contact resolution relying on proprioception is of the utmost

2. MULTI-LEGGED ROBOTIC SYSTEMS

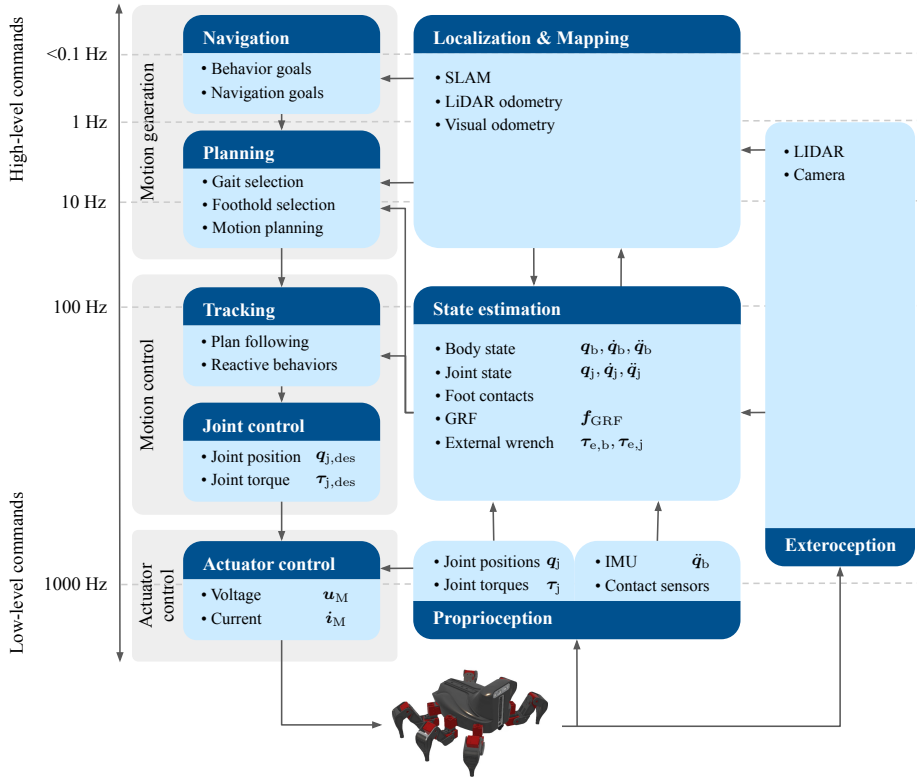


Figure 2.7: Overview of the multi-layer locomotion control architecture for electrically actuated multi-legged robots, with an outline of the three control layers. The main building blocks are accompanied by examples of related processes, methods, output variables, and typical required control rate; however, note that the particular locomotion control approach does not have to implement all of the building blocks listed, or might combine multiple building blocks together. Inspired by [100].

importance. For position control approaches, the explicit detection and handling of foot-contact events is required to safely negotiate individual steps. On the other hand, with force and impedance control methods, the reaction to foot contact is implicit as the foot-contact occurs emergently as a result of the control process. Explicit estimation of the leg-state, to determine whether the leg is supporting the body or not, is beneficial for methods to synchronize the gait phases between the legs [40], [58], [103]. Furthermore, explicit leg contact detection improves the accuracy of the legged odometry [104]–[106] and it is used to synchronize oscillations in bio-inspired controllers based on neural oscillators [107]–[109], or to trigger reflexive behaviors [109]–[111].

Various methods of explicit foot-contact detection and leg-state estimation have been presented in the literature, using different sensory modalities. One straight-

forward approach is to sense the foot contact at the leg foot-tips, which can be implemented using microswitches [46], [112], [113], pressure sensors [114], or ground contact optical force sensors [115]. Another method is to estimate or measure GRF. It can be accomplished by measuring joint torques at each joint directly [116], [117], estimate them using a linear model of the servomotor’s current [36], [67], or by utilizing strain-gauges [118], force-sensitive resistors [119], [120], or dedicated force-torque sensors [121], [122] mounted at the leg foot-tips. Besides, an additional compliant actuator can be added to individual legs to measure the GRF in the kinematic chain [123], [124]. An even more minimalistic setup can be based on the position feedback from the servomotors used for the locomotion that has been first presented in [125] and further extended in [2c]. Last but not least, in our work [6a], we have successfully utilized inertial data from leg-mounted accelerometers for foot-contact detection using a learned detector.

As can be seen, various methods can be utilized on top of the motion control to help negotiate individual footsteps by either implicitly or explicitly handling the interactions between the terrain and robot feet. However, purely blind locomotion control methods are missing look-ahead feature, which is enabled by the exteroceptive sensing. Exteroceptive sensing allows building a robot-centric local map of the environment [126] using stereo vision [127], RGB-D [7a], [128], or LiDAR [129], and plan the robot motion for an extended horizon as a part of motion generation. As the direct whole-body motion planning for legged robots is computationally demanding [130] due to the total number of DoF and huge set of possible foothold locations, the existing planning approaches introduce simplifications to the motion planning. The approaches differ in whether they consider body motion before footfalls [7a], [131]–[133], or footfalls before the body motion [57].

The body motion before footfalls methods plan the trajectory through the map as a sequence of robot body poses and subsequently plan the leg motions. Their drawback becomes apparent when two neighboring body poses cannot be connected with the leg planner. However, the method is suitable for navigating confined spaces [133]. Planning footfalls before body motion utilizes the reversed approach where first the foot placements are planned and then a body trajectory is synthesized that follows those footfalls. The method is suitable for terrains with a lack of suitable footholds [93]. Motion can also be planned using predefined motion primitives for different terrains, such as for advanced motions like wall walking or chimney climbing [48].

The three layers of motion generation, motion control, and actuator control form a hierarchical perspective of the locomotion control. However, they can be addressed together in particular locomotion control approaches. There are three main directions described in the literature [88], [134] for combined motion generation and motion control. Namely bio-inspired control, engineering-based control, and machine learning-based control. Main principles observed within the individual directions are described in the following paragraphs. For more exhaustive review, we kindly forward the reader to recent surveys [34], [77], [88], [134].

2. MULTI-LEGGED ROBOTIC SYSTEMS

Bio-inspired control relies on the Central Pattern Generator (CPG) artificial neural networks [62], [134]. In biological systems, CPGs are special neural circuits responsible for breathing, walking, and other repetitive processes in animals and insects [135], [136]. There are many different more or less biologically accurate implementations of CPGs [62], [134]; however, the main property of CPGs related to the locomotion control is stable CPG rhythm and its synchronization to external perturbations. Its dynamics can be described as a system containing a limit-cycle attractor, which, in turn, improves the overall robustness of the system to disturbances. It allows to smooth transition between different locomotion gaits [137] by changing the model parameters, such as the neural network weights. In locomotion control, a single [11a] or multiple coupled [107], [138] CPGs can be used to generate synchronized rhythmic outputs that are fed to the joints either through shaping neural networks or models [138], [12a], [8a] or by following the joint trajectory precomputed using Inverse Kinematics Task (IKT) [137], [11a].

Interlimb and intralimb synchronization denote synchronization between motion of individual legs and leg joints respectively. Together with reflexive behaviors, they are achieved by mutual inhibition and excitation of the individual CPG, that comply to behavioral rules observed in insects [139] or animals [53]. Figure 2.8 shows an example of the locomotion control architecture [12a] of a six-legged walking robot with six coupled CPGs together with an example of oscillator outputs with transition effect from steady-state to stable oscillations. It also show a transition between different locomotion gaits and corresponding leg trajectory, which stride length is influenced by the parameterisation of the output-shaping neural network.

However, with CPGs it is particularly hard to find a proper parameterisation of the network as the non-linear dynamic systems can adapt many behaviors from being static to being chaotic or divergent [134]. The parameters can be either hand-tuned [137], [141], learned in simulation [49] or from existing walking pattern using back-propagation [8a], or adapted using artificial hormone mechanism in a real-world lifelong continuous adaptation [142].

The engineering-based control relies on using an analytical model of the robot to achieve interlimb and intralimb coordination. We can distinguish kinetostatics-based control and dynamics-based control [77], [88]. Kinetostatics-based control is suitable for static gaits to control the projection of the CoM w.r.t. the support polygon [77]. A straightforward approach utilizing position-based motion control is to generate desired foot-tip trajectories in the body reference frame, use the IKT to translate the trajectory into the robot joint angles, and execute them in an open-loop fashion. However, such a method is only suitable for locomotion on flat terrain.

Considering the body motion together with the CoM projection, the static stability criteria states that the vertical projection of the CoM shall remain in the support polygon. The Zero Moment Point (ZMP) approach [143] is an extension of the static CoM stability criteria for dynamic locomotion. The ZMP takes into account

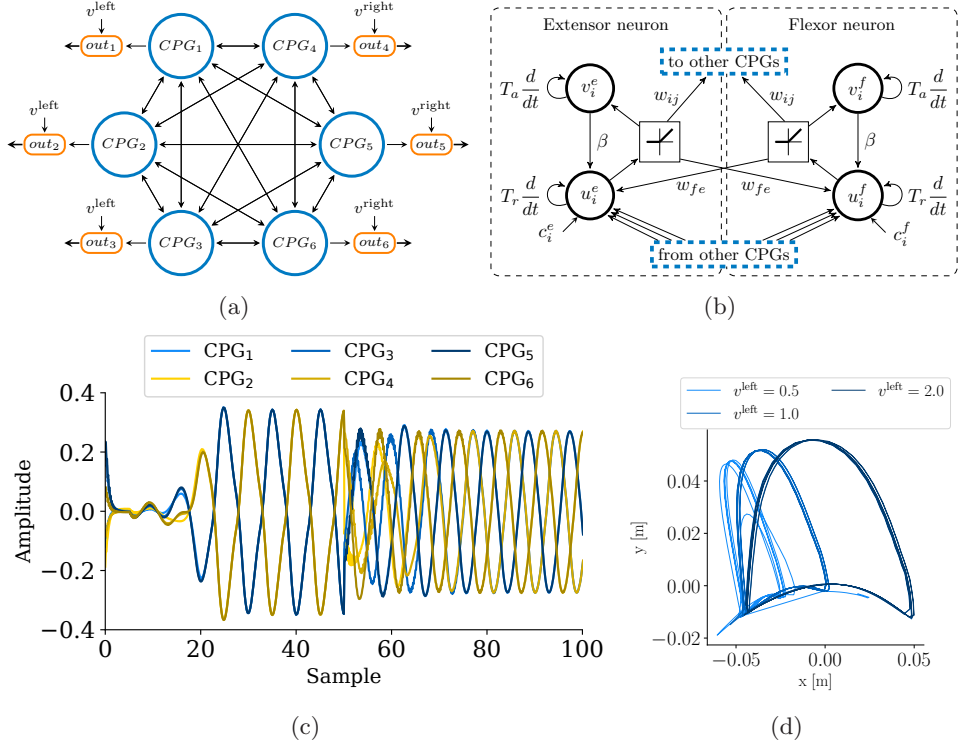


Figure 2.8: Example of bio-inspired locomotion control [12a]. (a) Schema of the CPG network with output shaping neural networks parameterised by the steering input $v^{\text{left}}, v^{\text{right}}$. (b) Schema of a single CPG unit (Matsuoka’s oscillator [140]). (c) Plot of CPG oscillations for a tripod gait and transition to amble gait with three legs and two legs swinging simultaneously, respectively. (d) Leg foot-tip trajectory plotted in the robot body reference frame for different v^{left} parameters.

the robot inertia, and represents a point on the ground where the resultant net moment of the inertial and gravity forces has no component along the horizontal axes [143]. When the ZMP is located within the support polygon, the legged robot is dynamically stable. Stable locomotion using the ZMP criterion has been shown for slow crawling six-legged robot [72] and it can be used for bipedal locomotion [144]. However, it is not suitable for running gaits as there is no obvious polygon for the ZMP calculation [77].

The motion of the body and the legs can be concurrent or nonconcurrent. With the nonconcurrent locomotion control, the leg motion phase, when the legs are swinging into new footholds and body is stationary, is followed by the body motion phase, in which the body moves to a new pose. It is advantageous in terms of stability [44], [2c], [103] as the robot can move its body between two stances with the maximum support provided by all its legs.

2. MULTI-LEGGED ROBOTIC SYSTEMS

On the other hand, the drawback of the method is the need to accelerate and decelerate the robot body with each transition between stances, which is energy inefficient and increases robot joints wear. The concurrent locomotion control controls the body motion and leg motion simultaneously.

The dynamics-based control approaches are based on the modeling and analysis of the deviation of motion caused by the environment interaction forces and torques applied on the robot. Dynamics-based control methods include [77] the Spring-Loaded Inverted Pendulum (SLIP) model [145], Virtual Model Control (VMC) [132], [146], [147], Model Predictive Control (MPC) [40], [148], and Whole-Body Control (WBC) [149]. The methods are detailed in the following paragraphs.

SLIP represents a simplistic representation of the robot by a point mass atop a spring [145]. In the model, the body tracks a ballistic trajectory and the spring is assumed to be compressed during the support phase of the gait cycle and to be stretched during the swing phase, releasing the stored energy. The main objective is to maximize the energy efficiency of the robot. However, the SLIP model does not take into account the complex dynamics of real legged robots.

The VMC is suitable for torque controlled robots [146]. It represents the dynamics and kinematics of the robot using a virtual model comprising of simple virtual components of mass, spring, and dampers between the CoM and contact points. Virtual forces and moments are calculated to produce the desired acceleration of the CoM, and transformed to the feedforward torques for the joint actuation [132]. Multiple virtual models can be combined to achieve line walking and balancing [147] with low-dimensional virtual model to generate balancing actions, and CoM controller to drive the robot along the desired path.

The MPC is an optimization approach based on forward dynamic model of the robot to predict its future motion and generates control signals to minimize a given cost-function over a fixed time horizon. Conventionally, the MPC minimizes the tracking error between the desired and actual motion [40], [148], [150]. The control strategy assumes exact dynamic model, ideal force-tracking actuators, and no external disturbances. While those are rather strong assumptions, the repeated optimization provides a feedback mechanism that can correct for modeling errors provided that the control loop can be executed at a sufficiently high rate [150], which is usually between 15 Hz to 30 Hz for highly dynamic legged robots [40], [150]. Also, the computational complexity allows for time horizon of a few hundreds of milliseconds only.

The WBC is a control framework that is accounting for the dynamics and kinematics of the entire robot, including all its bodies, joints, and actuators. It is based on the idea of controlling the entire robot as a single entity using inverse dynamics model of the whole robot [149], [151]. However, solving the optimization problem of inverse dynamics calculation in real-time is computationally challenging.

Engineering-based approaches to the multi-legged locomotion control perform well on structured grounds, but their real-world corner cases include whole-body inter-

action with the environment, slip detection and fall recovery, walking on collapsible or moving terrain, gait adaptation to specific terrain, or response to robot damage or morphology changes, which often require a specific control response [100].

An alternative way to creating heuristics and dedicated controllers to each of edge cases is to generate robot gaits and entrain system responses using machine learning [152]. High-fidelity computer simulations support learning locomotion policies [100], [153]; however, they require to deal with the reality gap due to different factors such as unaccounted dynamics, incorrect model parameters, and numerical instability of the simulations [153], [154]. On the other hand, simulations provide a safe sandbox for learning different behaviors without the risk of damaging the physical platform. Besides, it can take advantage of available privileged information that is not available to the real robot, such as the binary contact-states [155], or contact-states, GRF, and friction coefficients in a reinforcement learning-based control policy [152].

Besides, data-driven methods learn the controller behavior from real-world experimental deployments, such as learning the actuator model [152], black-box forward dynamics model of the robot leg [3a], or distinguishing foot-contact events detection from the inertial data [6a].

In this thesis, we present two kinetostatics-based locomotion control approaches for position-controlled multi-legged walking robots. The first approach [1c] follows the three layer architecture. It is based on projection of the desired leg footholds followed by the iterative body pose calculation and joint angle calculation for each leg using the IKT with position of the CoM projection taken into account to cope with locomotion in steep inclines. The second approach presents a method for the motion generation and motion control by formalizing the relationship between the leg motion and body motion into a single equation. Both of the controllers allow for seamless integration of the environmental feedback through foot-contact and external wrench sensing to support locomotion over irregular terrain and active environment interactions.

2.4 Environment Interaction Approaches

Any interaction of the legged robot with the environment induces forces and torques on the robot construction. Their contributions can be modeled using the Rigid Body Dynamics (RBD) model under the assumption that the mechanical bodies do not deform when forces are applied. The whole-body dynamics of the floating-base platform with total N_j controllable DoF can be expressed as [156]

$$\mathbf{M} \begin{bmatrix} \ddot{\mathbf{q}}_b \\ \ddot{\mathbf{q}}_j \end{bmatrix} + \begin{bmatrix} \boldsymbol{\eta}_b \\ \boldsymbol{\eta}_j \end{bmatrix} = \begin{bmatrix} \mathbf{0} \\ \boldsymbol{\tau}_j \end{bmatrix} + \sum_{i=1}^{N_C} \begin{bmatrix} \mathbf{J}_{b,i}^T \\ \mathbf{J}_{j,i}^T \end{bmatrix} \begin{bmatrix} \mathbf{f}_i \\ \mathbf{n}_i \end{bmatrix}, \quad (2.5)$$

where $\mathbf{q}_b = [r_{b,x}, r_{b,y}, r_{b,z}, \Phi_x, \Phi_y, \Phi_z]^T$ is the robot position and orientation in the global reference frame, $\mathbf{q}_j \in \mathbb{R}^{N_j}$ is the vector of the generalized joint coordinates, $\mathbf{M} \in \mathbb{R}^{(N_j+6) \times (N_j+6)}$ is the system inertia matrix, $\boldsymbol{\eta}_b \in \mathbb{R}^6$ and $\boldsymbol{\eta}_j \in \mathbb{R}^{N_j}$ are the joined Coriolis, centripetal, and gravity effects of the body and joints, respectively. $\boldsymbol{\tau}_j \in \mathbb{R}^{N_j}$ is the vector of generalized joint forces, $\mathbf{J}_{b,i} \in \mathbb{R}^{6 \times 6}$ and $\mathbf{J}_{j,i} \in \mathbb{R}^{6 \times N_j}$ are the contact Jacobian w.r.t. the body and joints, respectively, and $\mathbf{f}_i \in \mathbb{R}^3$ and $\mathbf{n}_i \in \mathbb{R}^3$ represent the individual forces and torques acting on the i -th contact point. N_C represents the number of all contact points.

The interactions are either deliberate, with known location of the interaction, or unintentional. Hence, the total number of contact points N_C can be further divided into the known contact points $N_{C,k}$ and unknown contact points $N_{C,u}$, such that $N_C = N_{C,k} + N_{C,u}$. Thus, we can model the cumulative contribution of external forces and torques on the dynamics of the robot as an additional term in the robot dynamic model [144] by rewriting Equation (2.5) to

$$\mathbf{M} \begin{bmatrix} \ddot{\mathbf{q}}_b \\ \ddot{\mathbf{q}}_j \end{bmatrix} + \begin{bmatrix} \boldsymbol{\eta}_b \\ \boldsymbol{\eta}_j \end{bmatrix} = \begin{bmatrix} \mathbf{0} \\ \boldsymbol{\tau}_j \end{bmatrix} + \sum_{i=1}^{N_{C,k}} \begin{bmatrix} \mathbf{J}_{b,i}^T \\ \mathbf{J}_{j,i}^T \end{bmatrix} \begin{bmatrix} \mathbf{f}_i \\ \mathbf{n}_i \end{bmatrix} + \begin{bmatrix} \boldsymbol{\tau}_{e,b} \\ \boldsymbol{\tau}_{e,j} \end{bmatrix}, \quad (2.6)$$

with separated contributions of forces and torques at known contact points and generalized external forces $\boldsymbol{\tau}_{e,b} \in \mathbb{R}^6$ and $\boldsymbol{\tau}_{e,j} \in \mathbb{R}^{N_j}$ acting on the body and joints, respectively, for which it applies

$$\begin{bmatrix} \boldsymbol{\tau}_{e,b} \\ \boldsymbol{\tau}_{e,j} \end{bmatrix} = \sum_{i=N_{C,k}+1}^{N_C} \begin{bmatrix} \mathbf{J}_{b,i}^T \\ \mathbf{J}_{j,i}^T \end{bmatrix} \begin{bmatrix} \mathbf{f}_i \\ \mathbf{n}_i \end{bmatrix}. \quad (2.7)$$

Equation (2.6) shows that, in the absence of additional information about the unknown acting forces and torques, only their cumulative effect, the external wrench, can be observed. It also shows that each interaction affects the robot acceleration and all the joint torques along the kinematic chain between its point of contact and the ground directly [157] and the whole robot morphology indirectly via the dynamic coupling. The locomotion controller is supposed to handle these interactions and drive the robot accordingly.

Handling of known and anticipated interactions by robot feet is overviewed in Section 2.3. There are two key interaction handling concepts: implicit and explicit. Both of these concepts are applicable in reaction to non-feet interactions as well.

In dynamically controlled multi-legged robots, the explicit estimation of the external wrench is a challenging problem because the GRF is the controlled variable. Although the instantaneous external wrench, together with the sensory and actuator noise, can be estimated through the disturbance observer [158], [159], or momentum observer [160], it is immediately compensated by the controller [43], [160]. Therefore, it is inseparable from the GRF, and the reaction to the contact event is an implicit part of the dynamic control strategy [161]. Under such a control strategy, the robot actively resists changes in its posture regardless of its cause.

The explicit external wrench estimation has been introduced in the context of collaborative manipulators [32] to maintain collision detection and human-robot interaction with safe reaction [162]. The generalized momentum introduced for robotic manipulators [163] can be utilized for contact force and torque estimation [164] using only proprioceptive sensing [165] in real-time [166]. For the floating-base systems, external wrench estimation has been shown for aerial vehicles [167] with follow-up works on aerial manipulation [168] and interaction resolution [169]. However, the floating-base dynamics of legged robots have strong coupling effects between the swing legs and the body, making the external wrench estimation a challenging problem [70].

External wrench plays an important role in stability control and realizing multi-contact scenarios. Notably, the authors of the survey [144] report on the researchers' shift towards external wrench modeling, specifically during the DARPA Robotics Challenge. The existing methods rely on direct sensing of the GRF and torques using dedicated force/torque sensors in robot ankles [170] or force sensing resistors [171] embedded in the robot feet to simplify the estimation of the external wrench. Alternatively, a simplified whole-body dynamics model is used to estimate the centroidal dynamics and, subsequently, the external wrench [172].

In our approach, we derive the whole-body dynamic model of the robot described in the following chapter. Next, we derive an analytical formula to allow continuous GRF and external wrench estimation using the virtual work principle. The external wrench estimation together with the deployment results on two different robotic platforms is detailed in Chapter 6.

2. MULTI-LEGGED ROBOTIC SYSTEMS

Chapter 3

Multi-legged Robot Modeling

This chapter provides the theoretical background for modeling the kinematics and dynamics of a floating-base rigid multibody system of a walking robot. The forward and inverse kinematic models, together with the velocity kinematics used in the proposed locomotion controllers and dynamic model establishment are described in Section 3.1. Section 3.2 covers our approach to modeling the dynamics. Two dynamic models derived using the Euler-Lagrange formulation are presented. One model for the robot leg with three DoF that takes into account the dynamics of the utilized electric actuators and their internal controller. The second is the whole-body model of the robot. The former model is utilized in the model-based leg collision detection approach, while the latter is utilized in the external wrench estimation approach described in Chapter 5 and Chapter 6, respectively.

We consider rigid body kinematics and dynamics of a six-legged walking robot with three DoF per leg and arachnoid leg morphology, which fits our main experimental platforms – SCARAB and HEBI robots. The main used symbols and mathematical notation are listed in Chapter Notation and Symbols. The naming convention for leg members follows the biological nomenclature of anthropod legs. The individual leg members named along the kinematic chain from body to foot-tip are coxa, femur, and tibia, as it is shown in Figure 3.1.

We use the concept of generalized coordinates to represent the motion of floating-base system. System kinematics and dynamics are described as a function of the N_q -dimensional vector of generalized coordinates

$$\mathbf{q} = \begin{bmatrix} \mathbf{q}_b \\ \mathbf{q}_j \end{bmatrix}, \quad (3.1)$$

where $\mathbf{q}_b \in \mathbb{R}^{N_b}$ is the body pose vector given as $\mathbf{q}_b = [\mathbf{r}_b^T, \Phi^T]^T$ with position $\mathbf{r}_b \in \mathbb{R}^3$ and orientation $\Phi \in \mathbb{R}^3$ represented using Tait-Bryan angle representation w.r.t. the world inertial frame $\{A\}$, and $\mathbf{q}_j \in \mathbb{R}^{N_j}$ represents vector of joint angles

$$\mathbf{q}_j = [\mathbf{q}_1^T, \mathbf{q}_2^T, \dots, \mathbf{q}_6^T]^T \quad (3.2)$$

$$= [\theta_{1,c}, \theta_{1,f}, \theta_{1,t}, \theta_{2,c}, \theta_{2,f}, \theta_{2,t}, \dots, \theta_{6,c}, \theta_{6,f}, \theta_{6,t}]^T, \quad (3.3)$$

where $\mathbf{q}_l \in \mathbb{R}^3$ is the vector of the l -th leg individual joint angles $\theta_{l,i} \in \mathbb{R}$, for leg $l \in \{1, \dots, 6\}$ and leg member $i \in \{c, f, t\}$. Further, $N_q = N_b + N_j$ with $N_b = 6$. For the considered walking platforms with six legs and three actuated DoF per leg $N_j = 18$. Figure 3.2 shows a multi-legged robot schematic with the used coordinate frames, parameters and vectors utilized for the kinematic and dynamic modeling.

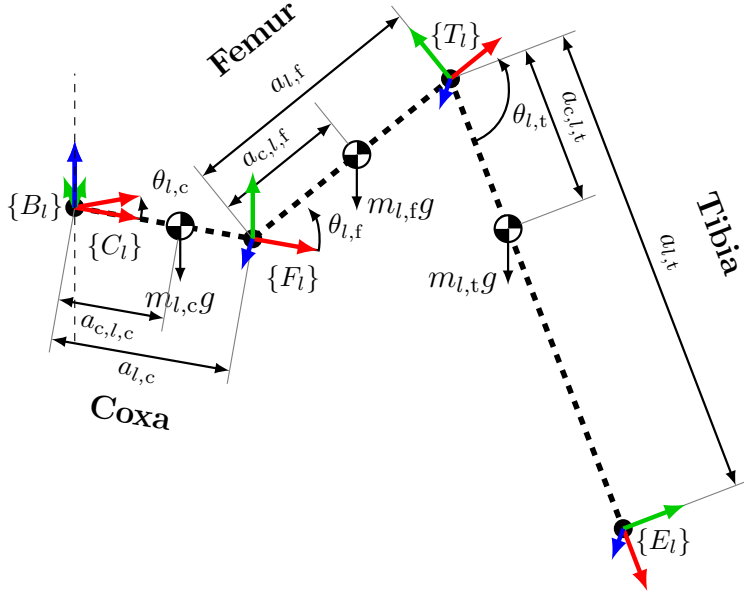


Figure 3.1: The schema of the multi-legged robot leg. From body to foot-tip the individual leg members are coxa, femur, and tibia.

3.1 Kinematic Model

In the kinetostatic locomotion control of position-controlled multi-legged robots, repetitive trajectories for individual legs describe the desired positions of the legs' foot-tips that achieve the desired motion of the robot. The desired trajectories has to be translated to the joint angles, which is approached using the **IKT**. Besides, Forward Kinematics Task (**FKT**) is needed in the body motion generation to adjust the robot posture. Therefore, both the **FKT** and **IKT** are the needed preliminaries. Furthermore, velocity kinematics that relates the joint angular velocities with foot-tip velocities are required for the closed-form model-based controller and establishing of the whole-body dynamic model of the robot. Note that the presented description includes material from publications [2c], [5a], and [31a].

3.1.1 Forward Kinematics

Five Cartesian coordinate systems cover the path from the world coordinate frame $\{A\}$ to the l -th leg foot-tip $\{E_l\}$ with three of them relative to the leg as it is depicted in Figure 3.1. Let ${}^A\mathbf{r}_l$ be the foot-tip position of the l -th leg in the inertial coordinate frame and ${}^{E_l}\mathbf{r}_l$ be the foot-tip position in the foot-tip coordinate system. Then, the mapping between the inertial coordinate frame and the foot-tip

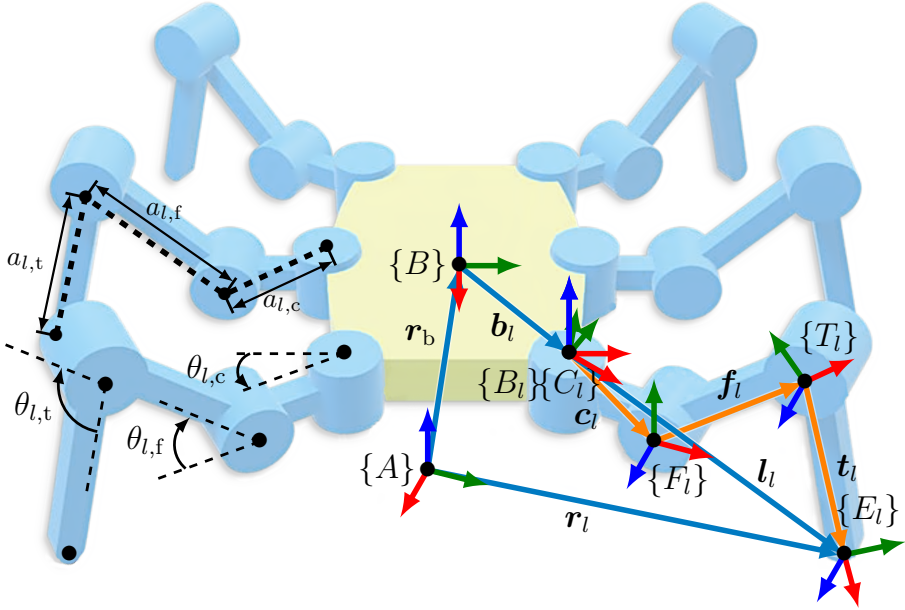


Figure 3.2: The schema of the multi-legged robot with the leg parameters and important vectors utilized for the locomotion controller formulation and dynamic model construction. The individual used coordinate frames $\{A\}, \{B\}, \{B_l\}, \{C_l\}, \{F_l\}, \{T_l\}, \{E_l\}$, are the world inertial coordinate frame, body-attached coordinate frame, and the l -th leg base, coxa, femur, tibia, and endpoint coordinate frames, respectively.

coordinate frame is given by the kinematic chain

$$\begin{bmatrix} {}^A r_l \\ 1 \end{bmatrix} = {}^A T_B {}^B T_{B_l} {}^{B_l} T_{C_l} {}^{C_l} T_{F_l} {}^{F_l} T_{T_l} {}^{T_l} T_{E_l} \begin{bmatrix} {}^{E_l} r_l \\ 1 \end{bmatrix}, \quad (3.4)$$

where ${}^X T_Y$ is a general SE(3) transformation matrix from coordinate frame $\{X\}$ to coordinate frame $\{Y\}$ that can be represented as

$${}^X T_Y = \begin{bmatrix} {}^X R_Y & {}^X t_Y \\ \mathbf{0} & 1 \end{bmatrix}, \quad (3.5)$$

where ${}^X R_Y \in \mathbb{R}^{3 \times 3}$ and ${}^X t_Y \in \mathbb{R}^3$ are the rotation matrix and translation vector that maps coordinate frame $\{X\}$ to the coordinate frame $\{Y\}$. While the first two transformation matrices represent a general transformation according to Equation (3.5), conveniently, each transformation matrix between two adjacent leg

3. MULTI-LEGGED ROBOT MODELING

coordinate systems can be expressed in the Denavit-Hartenberg (DH) convention:

$${}^X T_Y = \begin{bmatrix} \cos \psi_{l,i} & -\sin \psi_{l,i} \cos \alpha_{l,i} & \sin \psi_{l,i} \sin \alpha_{l,i} & a_{l,i} \cos \psi_{l,i} \\ \sin \psi_{l,i} & \cos \psi_{l,i} \cos \alpha_{l,i} & -\cos \psi_{l,i} \sin \alpha_{l,i} & a_{l,i} \sin \psi_{l,i} \\ 0 & \sin \alpha_{l,i} & \cos \alpha_{l,i} & d_{l,i} \\ 0 & 0 & 0 & 1 \end{bmatrix}, \quad (3.6)$$

$$\psi_{l,i} = \theta_{l,i} + \theta_{l,i}^{\text{off}},$$

where the link length $a_{l,i}$, link twist $\alpha_{l,i}$, joint distance $d_{l,i}$, joint angle $\theta_{l,i}$, and joint angle offset $\theta_{l,i}^{\text{off}}$ are the DH parameters of the individual l -th leg members $i \in \{c, f, t\}$. Notice that the transformation ${}^B T_{B_l}$ between the robot body frame $\{B\}$ and the l -th leg mount frame $\{B_l\}$ is fixed, given the mechanical construction of the robot. Therefore, it is convenient to represent the ${}^B T_{B_l}$ transformation using x and y offsets $p_{l,x}, p_{l,y}$, of the B_l joint and orientation β_l of the B_l coordinate frame w.r.t. the B coordinate frame such that

$${}^B T_{B_l} = \begin{bmatrix} \cos \beta_l & -\sin \beta_l & 0 & p_{l,x} \\ \sin \beta_l & \cos \beta_l & 0 & p_{l,y} \\ 0 & 0 & 1 & 0 \\ 0 & 0 & 0 & 1 \end{bmatrix}. \quad (3.7)$$

The particular values of the DH parameters and the leg mount frame transformations for our experimental platforms are listed in Appendix A.

3.1.2 Velocity Kinematics

The formulation of the twist of the feet and body given set of joint angles and joint angular velocities can be derived from forward kinematics expressed as

$${}^A \mathbf{r}_l(t) = f(\mathbf{q}_b(t), \mathbf{q}_l(t)). \quad (3.8)$$

Further, we know that $f(\mathbf{q}_b(t), \mathbf{q}_l(t))$ can be established from the kinematic loop between the legs and the body (according to Figure 3.2) as

$$f(\mathbf{q}_b(t), \mathbf{q}_l(t)) = {}^A \mathbf{r}_b(t) + {}^A \mathbf{b}_l(t) + {}^A \mathbf{c}_l(t) + {}^A \mathbf{f}_l(t) + {}^A \mathbf{t}_l(t). \quad (3.9)$$

The time derivative of Equation (3.8) at the time t can be written using the chain rule [101] as

$$\begin{aligned} \dot{\mathbf{r}}_l &= \frac{\partial f(\mathbf{q}_b, \mathbf{q}_l)}{\partial \mathbf{q}_b} \frac{d\mathbf{q}_b(t)}{dt} + \frac{\partial f(\mathbf{q}_b, \mathbf{q}_l)}{\partial \mathbf{q}_l} \frac{d\mathbf{q}_l(t)}{dt} \\ &= \mathbf{J}_b \dot{\mathbf{q}}_b + \mathbf{J}_l \dot{\mathbf{q}}_l, \end{aligned} \quad (3.10)$$

where $\mathbf{J}_b \in \mathbb{R}^{3 \times 6}$ is the body Jacobian and $\mathbf{J}_l \in \mathbb{R}^{3 \times 3}$ is the leg Jacobian.

The body Jacobian \mathbf{J}_b can be written as

$$\mathbf{J}_b = \begin{bmatrix} -{}^B\mathbf{R}_A & {}^B\mathbf{R}_A ({}^A\mathbf{b}_l + {}^A\mathbf{l}_l)^\times \end{bmatrix}, \quad (3.11)$$

where \mathbf{x}^\times is the skew-symmetric matrix representation of the cross-product of the vector \mathbf{x} .

The leg Jacobian \mathbf{J}_l can be written as

$$\mathbf{J}_l = \frac{\partial l_l}{\partial \mathbf{q}_l} = [{}^A\mathbf{R}_{C_l}[0, 0, 1]^T \quad {}^A\mathbf{R}_{F_l}[1, 0, 0]^T \quad {}^A\mathbf{R}_{T_l}[1, 0, 0]^T]. \quad (3.12)$$

■ 3.1.3 Inverse Kinematics

The inverse kinematics task for the leg with only three DoF has a straightforward analytical solution. Given the l -th leg foot-tip coordinates ${}^A\mathbf{r}_l$ in the inertial frame and knowing the robot pose ${}^A\mathbf{q}_b$ in the inertial frame, we can calculate the joint angles $\mathbf{q}_l = [\theta_{l,c}, \theta_{l,f}, \theta_{l,t}]^T$ as follows. First, we use the kinematic loop closures (shown in Figure 3.2) to calculate the vector ${}^A\mathbf{l}_l = [{}^A l_{l,x}, {}^A l_{l,y}, {}^A l_{l,z}]^T$, which captures the mutual position of the foot-tip frame $\{E\}$ and the leg mount frame $\{B_l\}$ in the inertial frame $\{A\}$ as

$${}^A\mathbf{r}_b + {}^A\mathbf{b}_l + {}^A\mathbf{c}_l + {}^A\mathbf{f}_l + {}^A\mathbf{t}_l - {}^A\mathbf{r}_l = \mathbf{0}, \quad (3.13)$$

$${}^A\mathbf{l}_l - {}^A\mathbf{c}_l - {}^A\mathbf{f}_l - {}^A\mathbf{t}_l = \mathbf{0}. \quad (3.14)$$

Next, we can obtain the coxa joint angle as

$$\theta_{l,c} = \arctan\left(\frac{{}^A l_{l,x}}{{}^A l_{l,y}}\right). \quad (3.15)$$

The vector ${}^A\mathbf{l}_l$ expressed relatively to the femur coordinate frame $\{F\}$ yields

$${}^F\mathbf{l}_l = \left[\sqrt{{}^A l_{l,x}^2 + {}^A l_{l,y}^2} - a_{l,c}, {}^A l_{l,z}, 0 \right]^T. \quad (3.16)$$

The respective femur $\theta_{l,f}$ and tibia $\theta_{l,t}$ joint angles are then given according to the cosine law and the angle above the horizon as one of the two possible solutions

$$\theta_{l,f} = \arccos\left(\frac{a_{l,f}^2 - a_{l,t}^2 + \|{}^F\mathbf{l}_l\|^2}{2a_{l,f}\|{}^F\mathbf{l}_l\|}\right) - \arctan\left(\frac{{}^F l_{l,y}}{{}^F l_{l,x}}\right) - \theta_{l,f}^{\text{Off}}, \quad (3.17)$$

$$\theta_{l,t} = \pi - \arccos\left(\frac{a_{l,f}^2 + a_{l,t}^2 - \|{}^F\mathbf{l}_l\|^2}{2a_{l,f}a_{l,t}}\right) - \theta_{l,t}^{\text{Off}}, \quad (3.18)$$

where $\|\mathbf{x}\|$ represents the Euclidean norm of the vector \mathbf{x} . The singular points of the IKT lie on the vertical line corresponding to the coxa joint axis. The particular implementation of the IKT has to take it into account.

■ 3.2 Dynamic Model

The dynamic equations explicitly describe the relationship between the motions and forces and torques that causes them. Various dynamic models are used to model the dynamics of multi-legged systems [70]. However, models are mere approximations of the actual physics and vary by how many assumptions they require. For example Rigid Body Dynamics (RBD) models assume that the bodies do not deform when forces are applied. Single RBD models that approximate the whole robot dynamics by only a single body additionally assume constant whole-body inertia and negligible momentum produced by the joint velocities.

We present a separate dynamic model of the leg and the whole-body dynamic model of the robot. Both models are derived using Euler-Lagrange formulation [101], [173] under the RBD assumption of non-deforming bodies. In addition, the leg model assumes a fixed leg base. The assumption simplifies the model and allows us to focus on the modeling of the centripetal and Coriolis effects acting on the leg in motion, as well as on the precise model of the joint actuator together with its control policy, which has a major impact on the fidelity of the model. The assumption is valid for the originally used controller with the decoupled body motion and leg motion [2c] in which the leg swing was performed only after the body motion was completed. However, it is also valid for the herein proposed controllers as both are designed to provide smooth motion of constant velocity, which minimizes the dynamic effects of the body on the legs. The whole-body dynamic model takes into account the coupling between the body and the legs, but assumes negligible centripetal and Coriolis effects on the robot legs due to their relatively low velocities as the inertial and gravity effects are more significant for construction of the used robots with more than half of their weight concentrated in the legs.

The dynamic model is presented as follows. Section 3.2.1 describes the leg model followed by the actuator model detailed in Section 3.2.2. Section 3.2.3 describes the whole-body dynamic model of the robot. Validity of the made assumptions has been investigated as a part of the evaluation reported in Chapter 6.

■ 3.2.1 Leg Dynamic Model

The leg dynamic model is derived according to the schema depicted in Figure 3.1 using Euler-Lagrange method under the fixed base and non-deforming bodies assumptions. The presented model follows on paper [2c], where the leg dynamic model for leg with only two DoF is presented, and extends it to incorporate additional DoF.

The Euler-Lagrange equations of motion for the l -th leg are given [101], [173] as

$$\mathcal{L}_l = \mathcal{K}_l - \mathcal{P}_l, \quad (3.19)$$

$$\boldsymbol{\tau}_l = \frac{d}{dt} \left(\frac{\partial \mathcal{L}_l}{\partial \dot{\mathbf{q}}_l} \right) - \frac{\partial \mathcal{L}_l}{\partial \mathbf{q}_l}, \quad (3.20)$$

where \mathcal{K}_l and \mathcal{P}_l are the kinetic and potential energy of the system, respectively. \mathbf{q}_l is a vector of the l -th leg generalized coordinates and $\boldsymbol{\tau}_l$ is the vector of the generalized joint forces. In our case, the generalized coordinates correspond to the joint angles $\mathbf{q}_l = [\theta_{l,c}, \theta_{l,f}, \theta_{l,t}]^T$ and generalized joint forces correspond to the joint torques.

The total kinetic energy \mathcal{K}_l of the l -th leg can be expressed as a sum of kinetic energies of individual leg members as

$$\mathcal{K}_l = \frac{1}{2} \dot{\boldsymbol{\chi}}_{l,c}^T \mathbf{M}_{l,c} \dot{\boldsymbol{\chi}}_{l,c} + \frac{1}{2} \dot{\boldsymbol{\chi}}_{l,f}^T \mathbf{M}_{l,f} \dot{\boldsymbol{\chi}}_{l,f} + \frac{1}{2} \dot{\boldsymbol{\chi}}_{l,t}^T \mathbf{M}_{l,t} \dot{\boldsymbol{\chi}}_{l,t}, \quad (3.21)$$

where $\dot{\boldsymbol{\chi}}_{l,i} \in \mathbb{R}^6$ is the twist vector of the CoM of the l -th leg's i -th member. It can be expressed using the body twist $\dot{\mathbf{q}}_b$ and joint angle rates $\dot{\mathbf{q}}_l$ as

$$\dot{\boldsymbol{\chi}}_{l,i} = \mathbf{J}_{b,l,i} \dot{\mathbf{q}}_b + \mathbf{J}_{j,l,i} \dot{\mathbf{q}}_l, \quad (3.22)$$

where $\mathbf{J}_{b,l,i} \in \mathbb{R}^{6 \times 6}$ and $\mathbf{J}_{j,l,i} \in \mathbb{R}^{6 \times 3}$ are Jacobian matrices that maps the body twist and the joint angle rates to the individual leg members, respectively. Further, $\mathbf{M}_{l,i} \in \mathbb{R}^{6 \times 6}$ is the symmetric and positive definite inertia matrix of the leg member given as

$$\mathbf{M}_{l,i} = \begin{bmatrix} m_{l,i} \mathbf{I}_{3 \times 3} & \mathbf{0}_{3 \times 3} \\ \mathbf{0}_{3 \times 3} & {}^A \mathbf{I}_{l,i} \end{bmatrix}, \quad (3.23)$$

where $\mathbf{I}_{3 \times 3}$ and $\mathbf{0}_{3 \times 3}$ are the identity matrix and zero matrix, respectively. $m_{l,i}$ is the mass of l -th leg's i -th member and ${}^A \mathbf{I}_{l,i}$ is its inertia matrix expressed in the inertial reference frame. The frame can be conveniently expressed in the member's own reference frame $\{X\}$, $X \in \{C_l, F_l, T_l\}$ via a similarity transformation

$${}^A \mathbf{I}_{l,i} = {}^A \mathbf{R}_X {}^X \mathbf{I}_{l,i} {}^A \mathbf{R}_X^T, \quad (3.24)$$

where ${}^A \mathbf{R}_X$ is the rotation matrix from the inertial frame $\{A\}$ to the member coordinate frame $\{X\}$. The particular inertia matrices ${}^X \mathbf{I}_{l,i}$ can be obtained from the 3D model of the leg members assuming the uniform material density of the parts. In our model-based contact detection approach we use the approximation of the leg members by a rigid rod rotating about the respective axis given by the

3. MULTI-LEGGED ROBOT MODELING

leg yaw-pitch-pitch morphology

$${}^c_l \mathbf{I}_{l,c} = \begin{bmatrix} 0 & 0 & 0 \\ 0 & 0 & 0 \\ 0 & 0 & 1/3 m_{l,c} a_{l,c}^2 \end{bmatrix}, \quad (3.25)$$

$${}^f_l \mathbf{I}_{l,f} = \begin{bmatrix} 0 & 0 & 0 \\ 0 & 1/3 m_{l,f} a_{l,f}^2 & 0 \\ 0 & 0 & 1/3 m_{l,f} a_{l,f}^2 \end{bmatrix}, \quad (3.26)$$

$${}^t_l \mathbf{I}_{l,t} = \begin{bmatrix} 0 & 0 & 0 \\ 0 & 1/3 m_{l,t} a_{l,t}^2 & 0 \\ 0 & 0 & 1/3 m_{l,t} a_{l,t}^2 \end{bmatrix}, \quad (3.27)$$

where $m_{l,i}$ and $a_{l,i}$ are the mass and length of the l -th leg's i -th member, respectively.

By substituting $\dot{\mathcal{X}}_{l,i}$ from Equation (3.22) into Equation (3.21), we can get the explicit formulation for the leg kinetic energy w.r.t. the body twist and joint angle rates

$$\mathcal{K}_l = \frac{1}{2} \dot{\mathbf{q}}_b^T \mathbf{M}_{b,l} \dot{\mathbf{q}}_b + \frac{1}{2} \dot{\mathbf{q}}_l^T \mathbf{M}_{j,l} \dot{\mathbf{q}}_l + \dot{\mathbf{q}}_b^T \mathbf{M}_{b,j,l} \dot{\mathbf{q}}_l, \quad (3.28)$$

where the inertia matrices $\mathbf{M}_{b,l} \in \mathbb{R}^{6 \times 6}$, $\mathbf{M}_{j,l} \in \mathbb{R}^{3 \times 3}$, and $\mathbf{M}_{b,j,l} \in \mathbb{R}^{6 \times 3}$ are

$$\mathbf{M}_{b,l} = \sum_{i \in \{c,f,t\}} \mathbf{J}_{b,l,i}^T \mathbf{M}_{l,i} \mathbf{J}_{b,l,i}, \quad (3.29)$$

$$\mathbf{M}_{j,l} = \sum_{i \in \{c,f,t\}} \mathbf{J}_{j,l,i}^T \mathbf{M}_{l,i} \mathbf{J}_{j,l,i}, \quad (3.30)$$

$$\mathbf{M}_{b,j,l} = \sum_{i \in \{c,f,t\}} \mathbf{J}_{b,l,i}^T \mathbf{M}_{l,i} \mathbf{J}_{j,l,i}. \quad (3.31)$$

The fixed base assumption $\mathbf{q}_b = \dot{\mathbf{q}}_b = \mathbf{0}$ reduces Equation (3.28) to

$$\mathcal{K}_l = \frac{1}{2} \dot{\mathbf{q}}_l^T \mathbf{M}_{j,l} \dot{\mathbf{q}}_l, \quad (3.32)$$

with the individual terms $M_{i,j}$ of the inertia matrix $\mathbf{M}_{j,l}$ being

$$M_{1,1} = I_{c,3,3} + I_{f,3,3} + I_{t,3,3} + m_{l,c} a_{l,c}^2 + m_{l,f} (a_{l,c} + a_{l,f} \cos(\theta_{l,f}))^2 + m_{l,t} (a_{l,c} + a_{l,t} \cos(\theta_{l,f} + \theta_{l,t}) + a_{l,f} \cos(\theta_{l,f}))^2, \quad (3.33)$$

$$M_{2,2} = I_{f,2,2} + I_{t,2,2} + m_{l,f} a_{l,f}^2 + m_{l,t} (a_{l,f}^2 + 2a_{l,f} a_{l,t} \cos(\theta_{l,t}) + a_{l,t}^2) + (I_{f,1,1} - I_{f,2,2} + I_{t,1,1} - I_{t,2,2}) \sin(\theta_{l,c})^2, \quad (3.34)$$

$$M_{2,3} = I_{t,2,2} + I_{t,1,1} \sin(\theta_{l,c})^2 - I_{t,2,2} \sin(\theta_{l,c})^2 + m_{l,t} (a_{l,t}^2 + a_{l,f} \cos(\theta_{l,t})), \quad (3.35)$$

$$M_{3,3} = I_{t,2,2} + m_{l,t} a_{l,t}^2 + (I_{t,1,1} - I_{t,2,2}) \sin(\theta_{l,c})^2, \quad (3.36)$$

$$M_{1,2} = M_{2,1} = M_{1,3} = M_{3,1} = 0, \quad (3.37)$$

where $I_{i,j,k}$ corresponds to the element at the position (j, k) of the respective inertia matrix $\mathbf{I}_{l,i}$ of the l -th leg's i -th member.

The potential energy of the l -th leg can be computed assuming the mass $m_{l,i}$ of each leg member is concentrated at its center of mass

$$\mathcal{P}_l = - \sum_{i \in \{c,f,t\}} \mathbf{g}^T \mathbf{r}_{c,l,i} m_{l,i}, \quad (3.38)$$

where \mathbf{g} is the gravitational acceleration vector w.r.t. the inertial frame, and $\mathbf{r}_{c,l,i}$ is the position vector of the l -th leg's i -th member CoM w.r.t. the same coordinate frame as it is shown in Figure 3.1

Substituting for \mathcal{K}_l and \mathcal{P}_l into Equation (3.19), we obtain the Lagrangian that we further substitute into Equation (3.20). Thus we obtain the motion equation

$$\boldsymbol{\tau}_l = \mathbf{M}_{j,l} \ddot{\mathbf{q}}_l + \dot{\mathbf{q}}_l^T \mathbf{C}_{j,l} \dot{\mathbf{q}}_l + \mathbf{G}_l, \quad (3.39)$$

where $\mathbf{C}_{j,l} \in \mathbb{R}^{3 \times 3 \times 3}$ is the matrix of joint Coriolis and centripetal terms, and the product of the quadratic term $\dot{\mathbf{q}}_l^T \mathbf{C}_{j,l} \dot{\mathbf{q}}_l$ should be interpreted [101] as

$$\dot{\mathbf{q}}_l^T \mathbf{C}_{j,l} \dot{\mathbf{q}}_l = \begin{bmatrix} \dot{\mathbf{q}}_l^T \mathbf{C}_{j,l,c} \dot{\mathbf{q}}_l \\ \dot{\mathbf{q}}_l^T \mathbf{C}_{j,l,f} \dot{\mathbf{q}}_l \\ \dot{\mathbf{q}}_l^T \mathbf{C}_{j,l,t} \dot{\mathbf{q}}_l \end{bmatrix}, \quad (3.40)$$

with the individual (j, k) elements $c_{i,j,k}$ of the i -th matrix $\mathbf{C}_{j,l,i}$ being the Christoffel Symbols of the first kind

$$c_{i,j,k} = \frac{1}{2} \left(\frac{\partial D_{ij}}{\partial \theta_k} + \frac{\partial D_{ik}}{\partial \theta_j} - \frac{\partial D_{jk}}{\partial \theta_i} \right). \quad (3.41)$$

The individual elements of $\mathbf{C}_{j,l,i}$ matrices are

$$\mathbf{C}_{j,l,c} = \begin{bmatrix} 0 & -c_1 & -c_2 \\ -c_1 & c_3 & c_4 \\ -c_2 & c_4 & c_4 \end{bmatrix}, \quad (3.42)$$

$$\mathbf{C}_{j,l,f} = \begin{bmatrix} c_1 & -c_3 & -c_4 \\ -c_3 & 0 & -c_5 \\ -c_4 & -c_5 & -c_5 \end{bmatrix}, \quad (3.43)$$

$$\mathbf{C}_{j,l,t} = \begin{bmatrix} c_1 & -c_4 & -c_4 \\ -c_4 & c_5 & 0 \\ -c_4 & 0 & 0 \end{bmatrix}, \quad (3.44)$$

3. MULTI-LEGGED ROBOT MODELING

where

$$c_1 = m_{l,t} (a_{l,t} \sin(\theta_{l,f} + \theta_{l,t}) + a_{l,f} \sin(\theta_{l,f})) (a_{l,c} + a_{l,t} \cos(\theta_{l,f} + \theta_{l,t}) + a_{l,f} \cos(\theta_{l,f})) + m_{l,f} a_{l,f} \sin(\theta_{l,f}) (a_{l,c} + a_{l,f} \cos(\theta_{l,f})), \quad (3.45)$$

$$c_2 = m_{l,t} a_{l,t} \sin(\theta_{l,f} + \theta_{l,t}) (a_{l,c} + a_{l,t} \cos(\theta_{l,f} + \theta_{l,t}) + a_{l,f} \cos(\theta_{l,f})), \quad (3.46)$$

$$c_3 = (I_{f,2,2} - I_{f,1,1} - I_{t,1,1} + I_{t,2,2}) \cos(\theta_{l,c}) \sin(\theta_{l,c}), \quad (3.47)$$

$$c_4 = (I_{t,2,2} - I_{t,1,1}) \cos(\theta_{l,c}) \sin(\theta_{l,c}), \quad (3.48)$$

$$c_5 = m_{l,t} a_{l,f} a_{l,t} \sin(\theta_{l,t}). \quad (3.49)$$

Finally, the gravity term \mathbf{G}_l can be expressed as

$$\mathbf{G}_l = \frac{\partial \mathcal{P}_l}{\partial \mathbf{q}_l} = g \begin{bmatrix} 0 \\ m_{l,t} (a_{c,l,t} \cos(\theta_{l,f} + \theta_{l,t}) + a_{c,l,f} \cos(\theta_{l,f})) + a_{c,l,f} m_{l,f} \cos(\theta_{l,f}) \\ a_{c,l,t} m_{l,t} \cos(\theta_{l,f} + \theta_{l,t}) \end{bmatrix} \quad (3.50)$$

where $g = 9.81\text{m s}^{-2}$ is the gravitational acceleration constant and a_{ci} is the distance between the joint and the CoM of the corresponding link.

3.2.2 Actuator Dynamic Model

The dynamical model formalized in Equation (3.39) considers only the dynamics of an interconnected chain of the ideal rigid bodies. However, there are other influencing physical forces such as the joint friction, deformation of bearings and gears, deflection of the links under load, vibrations. The actuator model is required to complete the dynamic model of the leg to be usable in the developed model-based leg contact detection approach. The full model of the leg dynamics together with the model of the actuators with their controller allow to determine the expected joint angles of the joint actuators influenced by the leg dynamics.

Our developed robotic platforms use actuators with an armature-controlled DC motors composed of the motor and a gearbox. A single actuator dynamics can be expressed based on [174] as

$$I_M \ddot{\theta}_M + B_M \dot{\theta}_M + F_M + \Gamma \tau = K_M u_M, \quad (3.51)$$

where τ is the actuator torque and θ_M is the rotor angle before gear reduction, which is coupled through the gearbox to the joint angle θ as

$$\Gamma \theta_M = \theta. \quad (3.52)$$

I_M is the rotor inertia, B_M is the rotor damping, F_M is a sum of static, dynamic, and viscous friction that depends on the current rotor speed, Γ is the gearbox ratio, K_M is the back electromotive force, and u_M is the motor voltage. The appropriate value of the parameters I_M , B_M , F_M , Γ , and K_M have to be experimentally identified

using the real servomotor or the values specified in the manufacturer data sheet can be utilized. The particular values of the parameters for our utilized actuators are listed in Appendix A.

A standard model with three components is considered to estimate the friction torque F_M . Namely the Coulomb friction τ_{fc} , viscous friction τ_{fv} , and static friction τ_{fs} with the particular terms expressed as

$$\tau_{fc} = \tau_c \operatorname{sgn}(\dot{\theta}_M), \quad (3.53)$$

$$\tau_{fv} = B_M \dot{\theta}_M, \quad (3.54)$$

$$\tau_{fs} = \begin{cases} \tau_e, & \text{if } \dot{\theta}_M = \ddot{\theta}_M = 0, \\ \tau_{fs\max} \operatorname{sgn}(\tau_e), & \text{if } \dot{\theta}_M = 0, \ddot{\theta}_M \neq 0, \\ 0, & \text{otherwise,} \end{cases} \quad (3.55)$$

where τ_c and τ_e are the coefficients of Coulomb and static friction, respectively. $\tau_{fs\max}$ is the maximal static friction, which represents the maximum value of the friction before the motor starts to move. Note that the viscous friction τ_{fv} is already considered as a term in Equation (3.51); hence, we can express the cumulative friction as

$$F_M = \tau_{fc} + \tau_{fs}. \quad (3.56)$$

The P-type position controller of the actuator influences the voltage u_M such that

$$u_M = k_P \operatorname{err}, \quad (3.57)$$

where k_P is the controller gain, and err is the difference between the current desired joint angle $\theta_{M,\text{des}}$ and current joint angle $\theta_{M,\text{real}}$, which is internally updated in the actuator with 1 kHz frequency¹. In high-fidelity modeling and simulation of the actuator, it is also necessary to take into account the discretization of the joint angle given by the used joint encoder with n_{enc} bits resolution, possible hard and soft joint angle limits, and the speed and latency of the communication channel between the actuator and controller.

The vectorized form of Equation (3.51) for the whole l -th leg can be written as

$$\mathbf{I}_{M,l} \ddot{\boldsymbol{\theta}}_{M,l} + \mathbf{B}_{M,l} \dot{\boldsymbol{\theta}}_{M,l} + \mathbf{F}_{M,l} + \boldsymbol{\Gamma}_l \boldsymbol{\tau}_l = \mathbf{K}_{M,l} \mathbf{u}_{M,l}, \quad (3.58)$$

where $\mathbf{I}_{M,l}, \mathbf{B}_{M,l}, \mathbf{F}_{M,l}, \mathbf{K}_{M,l} \in \mathbb{R}^{3 \times 3}$ are the symmetric diagonal matrices with the diagonal entries being the respective coefficients of the i -th joint actuator.

We eliminate $\boldsymbol{\theta}_M$ by substituting for θ_M from Equation (3.52) to Equation (3.51). Further, by substituting for $\boldsymbol{\tau}_l$ from Equation (3.39), we can obtain the desired complete leg dynamics in terms of joint variables

$$(\mathbf{I}_{M,l} + \boldsymbol{\Gamma}_l^2 \mathbf{M}_l) \ddot{\mathbf{q}}_l + (\mathbf{B}_{M,l} + \boldsymbol{\Gamma}_l^2 \mathbf{C}_l) \dot{\mathbf{q}}_l + \boldsymbol{\Gamma}_l \mathbf{F}_{M,l} + \boldsymbol{\Gamma}_l^2 \mathbf{G}_l = \boldsymbol{\Gamma}_l \mathbf{K}_{M,l} \mathbf{u}_{M,l}. \quad (3.59)$$

¹Both Dynamixel and HEBI actuators of our experimental platforms have internal control loop of 1 kHz that is used as a base time step for the leg motion simulation.

3. MULTI-LEGGED ROBOT MODELING

By an appropriate redefinition of symbols, we can further obtain the complete dynamic model in the traditional form

$$\mathbf{M}'_l \ddot{\mathbf{q}}_l + \mathbf{C}'_l \dot{\mathbf{q}}_l + \mathbf{F}'_l + \mathbf{G}'_l = \mathbf{K}'_l \mathbf{u}_{M,l}. \quad (3.60)$$

The particular values of the actuator model parameters are listed in Appendix A.

■ 3.2.3 Whole-Body Dynamic Model

The whole-body dynamic model is derived according to the schema depicted in Figure 3.2 using Euler-Lagrange method under the RBD rigid body assumption with the simplification of neglecting centripetal and Coriolis effects of the legs' dynamics due to their relatively low velocity. The dynamic model is formulated for a walking robot with three degrees of freedom per leg and it is described in generalized coordinates. Further, we approach the formulation of the whole-body dynamic model of the robot by deriving the kinetic and potential energies for the legs and body. Then by combining them into a single model allows us to formulate the analytical expression of the GRF and external wrench estimation.

The kinetic and potential energy of the leg is given by Equation (3.28) and Equation (3.38). Having the l -th leg kinetic energy \mathcal{K}_l , we can determine the terms of the robot dynamic model using the derivations assuming negligible centripetal and Coriolis terms of the leg dynamics as

$$\frac{d}{dt} \left(\frac{\partial}{\partial \dot{\mathbf{q}}_b} \mathcal{K}_l \right) - \frac{\partial}{\partial \mathbf{q}_b} \mathcal{K}_l \simeq \mathbf{M}_{b,l} \ddot{\mathbf{q}}_b + \mathbf{M}_{b,j,l} \ddot{\mathbf{q}}_l, \quad (3.61)$$

$$\frac{d}{dt} \left(\frac{\partial}{\partial \dot{\mathbf{q}}_l} \mathcal{K}_l \right) - \frac{\partial}{\partial \mathbf{q}_l} \mathcal{K}_l \simeq \mathbf{M}_{b,j,l}^T \ddot{\mathbf{q}}_b + \mathbf{M}_{j,l} \ddot{\mathbf{q}}_l. \quad (3.62)$$

By differentiating the potential energy given by Equation (3.38), we can find the gravity terms of the robot dynamic equation

$$\frac{\partial P_l}{\partial \mathbf{q}_l} = - (m_{l,c} \mathbf{J}_{r,l,c}^T + m_{l,f} \mathbf{J}_{r,l,f}^T + m_{l,t} \mathbf{J}_{r,l,t}^T) \mathbf{g} = -\mathbf{M}_{G,j,l} \mathbf{g}, \quad (3.63)$$

$$\frac{\partial P_l}{\partial \mathbf{q}_b} = - (m_{l,c} \mathbf{J}_{b,l,c}^T + m_{l,f} \mathbf{J}_{b,l,f}^T + m_{l,t} \mathbf{J}_{b,l,t}^T) \mathbf{g} = -\mathbf{M}_{G,b,l} \mathbf{g}, \quad (3.64)$$

where $\mathbf{J}_{b,l,i}$ denotes the linear part of the Jacobian matrix of the l -th leg's i -th member's CoM.

The next step is to derive the kinetic energy \mathcal{K}_b of the moving platform. Since the moving platform is a single rigid body, its kinetic energy can be expressed as

$$\mathcal{K}_b = \frac{1}{2} \dot{\mathbf{q}}_b^T \mathbf{M}_b \dot{\mathbf{q}}_b, \quad (3.65)$$

where $\mathbf{M}_b \in \mathbb{R}^{6 \times 6}$ is the body inertial matrix given as

$$\mathbf{M}_b = \begin{bmatrix} m_b \mathbf{I}_{3 \times 3} & \mathbf{0}_{3 \times 3} \\ \mathbf{0}_{3 \times 3} & {}^A \mathbf{I}_b \end{bmatrix}, \quad (3.66)$$

with m_b being the moving platform mass and ${}^A \mathbf{I}_b$ is the inertia matrix of the robot base relative to the inertial frame. It can be conveniently represented w.r.t. the body reference frame $\{B\}$ using

$${}^A \mathbf{I}_b = {}^A \mathbf{R}_B {}^B \mathbf{I}_b {}^A \mathbf{R}_B^T, \quad (3.67)$$

where ${}^A \mathbf{R}_B$ is the rotation matrix from the world coordinate frame $\{A\}$ to the body coordinate frame $\{B\}$.

We can then derive the body related dynamic model terms by differentiating the kinetic energy of the moving platform given by Equation (3.65)

$$\frac{d}{dt} \left(\frac{\partial}{\partial \dot{\mathbf{q}}_b} \mathcal{K}_b \right) - \frac{\partial}{\partial \mathbf{q}_b} \mathcal{K}_b = \mathbf{M}_b \ddot{\mathbf{q}}_b + \mathbf{C}_b \dot{\mathbf{q}}_b, \quad (3.68)$$

where

$$\mathbf{C}_b = \begin{bmatrix} \mathbf{0}_{3 \times 3} & \mathbf{0}_{3 \times 3} \\ \mathbf{0}_{3 \times 3} & \boldsymbol{\omega}_b^\times {}^A \mathbf{I}_b \end{bmatrix} \quad (3.69)$$

and $\boldsymbol{\omega}_b^\times = [\dot{\Phi}_x, \dot{\Phi}_y, \dot{\Phi}_z]^\times$ is the skew-symmetric representation of the body angular velocity.

The potential energy \mathcal{P}_b of the robot body can be expressed as

$$\mathcal{P}_b = -m_b \mathbf{g}^T \mathbf{r}_b, \quad (3.70)$$

where \mathbf{r}_b is the position vector of the body CoM w.r.t. the inertial frame as shown in Figure 3.2. The differentiation of Equation (3.70) gives the gravity term of the body dynamics

$$\frac{\partial \mathcal{P}_b}{\partial \mathbf{q}_b} = \mathbf{G}_b = \begin{bmatrix} -m_b \mathbf{g} \\ \mathbf{0}_{3 \times 1} \end{bmatrix}. \quad (3.71)$$

Next, we can derive the generalized force by calculating the virtual work done by the joint torques $\boldsymbol{\tau}_l$ of each l -th leg, and all the external forces \mathbf{f}_i and torques \mathbf{n}_i acting at N_C different contact points of the robot construction using the d'Alembert principle

$$\delta W = \sum_{l=1}^6 \boldsymbol{\tau}_l^T \delta \mathbf{q}_l - \sum_{i=1}^{N_C} \begin{bmatrix} \mathbf{f}_i \\ \mathbf{n}_i \end{bmatrix}^T \delta \begin{bmatrix} \mathbf{a}_i \\ \boldsymbol{\varphi}_i \end{bmatrix}, \quad (3.72)$$

where $\delta \mathbf{a}_i$ is the infinitesimal displacement of the point of application of the acting force \mathbf{f}_i and $\delta \boldsymbol{\varphi}_i$ is the infinitesimal rotation of the rigid body caused by the acting torque \mathbf{n}_i . The total number of contact points N_C can be divided into the known

3. MULTI-LEGGED ROBOT MODELING

contact points $N_{C,k}$ and unknown contact points $N_{C,u}$, such that $N_C = N_{C,k} + N_{C,u}$. Hence, we can expand Equation (3.72) as

$$\delta W = \sum_{l=1}^6 \boldsymbol{\tau}_l^T \delta \mathbf{q}_l - \sum_{i=1}^{N_{C,k}} \begin{bmatrix} \mathbf{f}_i \\ \mathbf{n}_i \end{bmatrix}^T \delta \begin{bmatrix} \mathbf{a}_i \\ \boldsymbol{\varphi}_i \end{bmatrix} + \sum_{i=N_{C,k}+1}^{N_C} \begin{bmatrix} \mathbf{f}_i \\ \mathbf{n}_i \end{bmatrix}^T \delta \begin{bmatrix} \mathbf{a}_i \\ \boldsymbol{\varphi}_i \end{bmatrix}. \quad (3.73)$$

With multi-legged robots, the feet are considered the known contact points of acting GRF $\mathbf{f}_{\text{GRF},l}$. Furthermore, with our experimental platforms, we consider only the GRF and omit the torques because the robot cannot exert ground moments through the pointy foot-tips. Without additional information about the unknown acting forces and torques, we can observe only their cumulative effect as an external wrench $\boldsymbol{\tau}_{e,b} \in \mathbb{R}^6$ acting on the robot body. Hence, we simplify Equation (3.73) as

$$\delta W = \sum_{l=1}^6 \boldsymbol{\tau}_l^T \delta \mathbf{q}_l - \sum_{l=1}^6 (\mathbf{f}_{\text{GRF},l}^T \delta \mathbf{r}_l) + \boldsymbol{\tau}_{e,b}^T \delta \mathbf{q}_b, \quad (3.74)$$

where \mathbf{r}_l is the position vector of the l -th leg foot-tip as it is shown in Figure 3.2. The vector can be expressed using the generalized coordinates as

$$\delta \mathbf{r}_l = -{}^A \mathbf{R}_B {}^B \mathbf{R}_{B_l} \mathbf{J}_b \delta \mathbf{q}_b + {}^A \mathbf{R}_B {}^B \mathbf{R}_{B_l} \mathbf{J}_l \delta \mathbf{q}_l. \quad (3.75)$$

By substituting for \mathbf{r}_l in Equation (3.74), we can obtain the generalized inertia forces Q_b and Q_l w.r.t. the body \mathbf{q}_b and leg joint \mathbf{q}_l generalized coordinates as Equations (3.77) and (3.78), respectively.

$$\delta W = Q_b \delta \mathbf{q}_b + \sum_{l=1}^6 Q_l \delta \mathbf{q}_l, \quad (3.76)$$

$$Q_b = -\boldsymbol{\tau}_{e,b} + \sum_{l=1}^6 (\mathbf{J}_b^T {}^{B_i} \mathbf{R}_B {}^B \mathbf{R}_A \mathbf{f}_{\text{GRF},l}), \quad (3.77)$$

$$Q_l = \boldsymbol{\tau}_l - \mathbf{J}_l^T {}^{B_i} \mathbf{R}_B {}^B \mathbf{R}_A \mathbf{f}_{\text{GRF},l}. \quad (3.78)$$

By adding the dynamic terms of the legs and body derived earlier, we can formulate the whole dynamics of the robot into two separate differential Equations (3.79) and (3.80).

$$\mathbf{M}_{b,j,l}^T \ddot{\mathbf{q}}_b + \mathbf{M}_{j,l} \ddot{\mathbf{q}}_l + \mathbf{M}_{G,j,l} \mathbf{g} = \boldsymbol{\tau}_l - \mathbf{J}_l^T {}^{B_i} \mathbf{R}_B {}^B \mathbf{R}_A \mathbf{f}_{\text{GRF},l}, \quad (3.79)$$

$$\begin{aligned} & \left(\mathbf{M}_b + \sum_{l=1}^6 \mathbf{M}_{b,l} \right) \ddot{\mathbf{q}}_b + \sum_{l=1}^6 \mathbf{M}_{b,j,l} \ddot{\mathbf{q}}_l + \sum_{l=1}^6 \mathbf{M}_{G,b,l} \mathbf{g} + \mathbf{C}_b \dot{\mathbf{q}}_b + \mathbf{G}_b \\ & = -\boldsymbol{\tau}_{e,b} + \sum_{l=1}^6 \mathbf{J}_b^T {}^{B_i} \mathbf{R}_B {}^B \mathbf{R}_A \mathbf{f}_{\text{GRF},l}. \end{aligned} \quad (3.80)$$

By rewriting Equation (3.79), we can extract the equation for the l -th leg GRF $\mathbf{f}_{\text{GRF},l}$ at the foot-tip as

$$\mathbf{f}_{\text{GRF},l} = {}^A \mathbf{R}_B {}^B \mathbf{R}_{B_i} \mathbf{J}_l^{-T} (\boldsymbol{\tau}_l - \mathbf{M}_{\text{b},j,l}^T \ddot{\mathbf{q}}_{\text{b}} - \mathbf{M}_{j,l} \ddot{\mathbf{q}}_l - \mathbf{M}_{\text{G},j,l} \mathbf{g}). \quad (3.81)$$

Considering these relations, we can derive the whole-body dynamic model of the robot according to the form presented in Equation (2.6) as

$$\mathbf{M} \begin{bmatrix} \ddot{\mathbf{q}}_{\text{b}} \\ \ddot{\mathbf{q}}_j \end{bmatrix} + \begin{bmatrix} \boldsymbol{\eta}_{\text{b}} \\ \boldsymbol{\eta}_j \end{bmatrix} = \begin{bmatrix} \mathbf{0}_{6 \times 1} \\ \boldsymbol{\tau}_j \end{bmatrix} + \sum_{l=1}^6 \begin{bmatrix} \mathbf{J}_{\text{b},l}^T \\ \mathbf{J}_{j,l}^T \end{bmatrix} \begin{bmatrix} \mathbf{f}_{\text{GRF},l} \\ \mathbf{0}_{3 \times 1} \end{bmatrix} + \begin{bmatrix} -\boldsymbol{\tau}_{\text{e},\text{b}} \\ \mathbf{0}_{18 \times 1} \end{bmatrix}, \quad (3.82)$$

where the system inertia matrix $\mathbf{M} \in \mathbb{R}^{24 \times 24}$ is given as:

$$\mathbf{M} = \begin{bmatrix} \left(\mathbf{M}_{\text{b}} + \sum_{l=1}^6 \mathbf{M}_{\text{b},l} \right) & \mathbf{M}_{\text{b},j,1} & \mathbf{M}_{\text{b},j,2} & \cdots & \mathbf{M}_{\text{b},j,6} \\ \mathbf{M}_{\text{b},j,1}^T & \mathbf{M}_{j,1} & \mathbf{0}_{3 \times 3} & \cdots & \mathbf{0}_{3 \times 3} \\ \mathbf{M}_{\text{b},j,2}^T & \mathbf{0}_{3 \times 3} & \mathbf{M}_{j,2} & \cdots & \mathbf{0}_{3 \times 3} \\ \vdots & \vdots & & \ddots & \vdots \\ \mathbf{M}_{\text{b},j,6}^T & \mathbf{0}_{3 \times 3} & \mathbf{0}_{3 \times 3} & \cdots & \mathbf{M}_{j,6} \end{bmatrix}. \quad (3.83)$$

The joined Coriolis, centripetal, and gravity effects of the body $\boldsymbol{\eta}_{\text{b}} \in \mathbb{R}^6$ and the joints $\boldsymbol{\eta}_j \in \mathbb{R}^{18}$ are given as

$$\boldsymbol{\eta}_{\text{b}} = \mathbf{C}_{\text{b}} \dot{\mathbf{q}}_{\text{b}} + \mathbf{G}_{\text{b}} + \sum_{l=1}^6 \mathbf{M}_{\text{G},\text{b},l} \mathbf{g}, \quad (3.84)$$

$$\boldsymbol{\eta}_j = \begin{bmatrix} \mathbf{M}_{\text{G},j,1} \mathbf{g} \\ \mathbf{M}_{\text{G},j,2} \mathbf{g} \\ \vdots \\ \mathbf{M}_{\text{G},j,6} \mathbf{g} \end{bmatrix}. \quad (3.85)$$

$\mathbf{J}_{\text{b},l} \in \mathbb{R}^{6 \times 6}$ and $\mathbf{J}_{j,l} \in \mathbb{R}^{6 \times 18}$ are the contact Jacobian *w.r.t.* the body and joints, respectively.

3. MULTI-LEGGED ROBOT MODELING

Chapter 4

Multi-legged Locomotion Control

In this chapter, we describe two proposed kinetostatics-based locomotion controllers for position-based control of multi-legged robots. Both controllers take the desired body twist command $\dot{\mathbf{q}}_b$ on the input and produce joint angles \mathbf{q}_j on the output. The methods mainly differ in the way they approach the motion generation. The first approach [1c] follows the three layered decomposition with motion generation realized by projection of the desired footholds, followed by the motion control with the iterative body pose and joint configuration calculation using **IKT**, and actuator control incorporating the joint feedback in adaptive reaction to terrain irregularities. In the approach the body motion is determined by the leg motion and thus the velocity command is effectively restricted to the projected locomotion plane, thus only translational components along the x and y axes and rotational component around the z axis are taken into account in the motion generation. The velocity command is also sampled only at the beginning of each gait phase, and thus the robot cannot change the motion direction during the leg swing phase.

On the other hand, the second approach represents a method for the motion generation and motion control by formalizing the relationship between the leg motion and the body motion into a single equation using velocity kinematics. The body motion is generated concurrently with the leg motion, and thus the full body twist command is used in the motion generation and the robot can change the motion direction at any time.

Both controllers allow for seamless integration of the environmental feedback through foot-contact and external wrench sensing to support locomotion over irregular terrain and active environment interactions. Further, both controllers are developed with the assumption of non-sliding feet.

The decoupled locomotion controller is described in Section 4.1 followed by the closed-form locomotion controller described in Section 4.2. Both controllers are derived in the inertial frame; hence, if not explicitly stated otherwise, all poses are considered *w.r.t.* the inertial frame $\{A\}$. The report on the experimental evaluation of the controllers is dedicated to Section 4.3.

4.1 Decoupled Locomotion Controller

The decoupled locomotion controller is based on the controller [2c], extended by implementing the concurrent generation of body motion and legs motion. The proposed controller also implements balance control that takes into account the mutual position of CoM and the support polygon for locomotion over steep inclines and load balancing between the legs. The balance control can be used in the case the robot features an Inertial Measurement Unit (IMU) or Attitude and Heading Reference System (AHRS). The proposed controller works as follows.

During the locomotion, each leg alternates between the support, and swing phase. The order in which legs alternate is defined by the fixed-sequence locomotion gait that can be described as a sequence \mathcal{G} of the sets of concurrently swinging legs. Hence, \mathcal{G} is given as $\mathcal{G} = \{\mathcal{G}_k | k \in \{1, \dots, N_{gp}\}\}$, where \mathcal{G}_k is the set of leg IDs used within a single gait phase k and N_{gp} is the overall number of gait phases. The leg IDs are assigned to the individual legs as shown in Figure 4.1. The utilized and tested locomotion gaits are: the tripod gait $\mathcal{G} = \{\{1, 3, 5\}, \{2, 4, 6\}\}$; tetrapod gait $\mathcal{G} = \{\{1, 5\}, \{2, 4\}, \{3, 6\}\}$; and pentapod gait $\mathcal{G} = \{\{1\}, \{6\}, \{2\}, \{5\}, \{3\}, \{4\}\}$ with the number of gait phases $N_{gp} = 2$, $N_{gp} = 3$, and $N_{gp} = 6$, respectively. Besides, the formulation of the controller can be easily modified to support free-sequence aperiodic gaits [98] for selection of swinging legs.

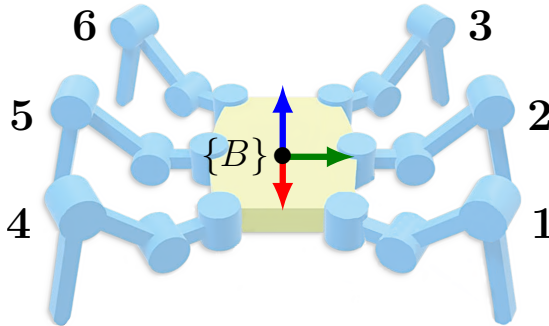


Figure 4.1: Leg IDs assignment to individual legs w.r.t. the body-attached coordinate frame $\{B\}$.

The robot locomotion is controlled using the gait cycle with N_{gp} individual phases and the desired gait cycle execution time T . During each gait cycle phase k , the legs are driven from their original poses \mathcal{P}_{curr} to new poses \mathcal{P}_{new} given w.r.t. the inertial frame within the time $T_{sp} = T N_{gp}^{-1}$, while the body pose \mathbf{q}_b is continuously optimized to cope with the terrain irregularities and current terrain inclination. The formulation of the controller w.r.t. the inertial frame allows for decoupling the control into three separate parts. Namely, the supporting legs are commanded to hold their foot-tip position, the swinging legs are driven to new footholds, and the body follows the current configuration of the legs. The internal control loop

is synchronized with the hardware control period of T_{con} that is given by the maximum achievable communication speed of the employed actuators [5a]. The control period T_{con} is determined, such that a single configuration write and read of all the joint actuators is achieved within each iteration of the control loop. The whole control algorithm is summarized in Algorithm 1 and schematically visualized in Figure 4.2. A detailed description of the control strategy follows.

At the beginning of each gait cycle phase k , a set of the current leg foot-tip positions $\mathcal{P}_{\text{curr}} = \{\mathbf{r}_{l,\text{curr}} \mid l \in \{1, \dots, 6\}\}$ is sampled by reading out the leg joint angles $\mathbf{q}_{l,\text{real}}$ and calculating the positions using the FKT (described in Section 3.1.1) assuming the body pose to be zero, $\mathbf{q}_{\text{b}} = \mathbf{0}$.

A new set of desired foot-tip positions $\mathcal{P}_{\text{new}} = \{\mathbf{r}_{l,\text{new}} \mid l \in \{1, \dots, 6\}\}$ given in the global reference frame is calculated based on the current body pose, the set of the default robot footholds $\mathcal{P}_{\text{def}} = \{\mathbf{r}_{l,\text{def}} \mid l \in \{1, \dots, 6\}\}$, which represents the default positions of the leg endpoints when the robot is standing in the default posture, the input twist command $\dot{\mathbf{q}}_{\text{b}} = [\dot{r}_{\text{b},x}, \dot{r}_{\text{b},y}, \dot{r}_{\text{b},z}, \dot{\Phi}_x, \dot{\Phi}_y, \dot{\Phi}_z]^T$, and the desired gait cycle execution time T . The new desired foothold coordinates of the l -th leg can be expressed as

$$\begin{bmatrix} \mathbf{r}_{l,\text{new}} \\ 1 \end{bmatrix} = \begin{bmatrix} \cos(\dot{\Phi}_z T) & -\sin(\dot{\Phi}_z T) & 0 & \dot{r}_{\text{b},x} T \\ \sin(\dot{\Phi}_z T) & \cos(\dot{\Phi}_z T) & 0 & \dot{r}_{\text{b},y} T \\ 0 & 0 & 1 & 0 \\ 0 & 0 & 0 & 1 \end{bmatrix} \begin{bmatrix} \mathbf{r}_{l,\text{def}} \\ 1 \end{bmatrix}. \quad (4.1)$$

Note that only the translational velocity along the x and y axes and angular velocity around the z axis are used in the generation of the new desired footholds. Also, to prevent self collisions during leg swing, the feasibility of the new desired foothold positions $\mathbf{r}_{l,\text{new}}$ is checked, and the input twist command is updated in the case of possible self-collision is detected. In particular, the input twist command is multiplied by the factor 0.9 and the desired footholds are recalculated and checked for self-collisions again until the motion is collision-free. Note that setting $\mathbf{q}_{\text{b}} = \mathbf{0}$ at the beginning of the gait phase allows projecting the new foothold positions in the current direction of the motion, which copes with the current body attitude, and thus the current terrain slope. Hence the robot maintains the desired twist command even when walking sloped terrain.

Once the new footholds are determined, the swinging legs swing from their current positions to the new foothold positions. The main control loop consists of phases of deciding the immediate desired foot-tip position $\mathbf{r}_{l,\text{des}}$ of each leg in the global reference frame followed by the optimization of the body pose \mathbf{q}_{b} using the sampled gravity vector \mathbf{g} . Then, the immediate desired joint angles $\mathbf{q}_{l,\text{des}}$ for each leg are calculated using the IKT, and are commanded to the joint actuators.

Finally, the current pose of the legs is sampled by reading out the current joint angles $\mathbf{q}_{l,\text{real}}$ that can be used in the foot-contact to adapt to terrain irregularities.

Algorithm 1: Gait cycle execution

Input: \mathcal{G} – fixed-sequence gait prescribed as a sequence of sets of concurrently swinging leg IDs.

Input: N_{gp} – number of gait phases.

Input: T – gait cycle execution time.

Input: T_{con} – control loop period.

Input: $\dot{\mathbf{q}}_b$ – input twist command.

```

1  $N_{sp} \leftarrow T N_{gp}^{-1} T_{con}^{-1}$  // no. of leg swing poses per gait phase
2  $\mathbf{q}_{j,real} \leftarrow \text{ReadAllServoAngles}()$ 
3 foreach gait phase  $k \in \{1, \dots, N_{gp}\}$  do
4    $\mathbf{q}_b \leftarrow \mathbf{0}$  // zero the current body pose
5    $\mathcal{G}_{swing} \leftarrow \mathcal{G}_k$  // select swinging legs
6    $\mathcal{P}_{curr} \leftarrow \text{CalcCurrentFootholdPositions}(\mathbf{q}_b, \mathbf{q}_{j,real})$ 
7    $\mathcal{P}_{new} \leftarrow \text{CalcNewFootholdPositions}(\mathbf{q}_b, \dot{\mathbf{q}}_b)$ 
8    $t \leftarrow 0$  // reset execution timer
9   while not  $\mathcal{G}_{swing}$  empty do // control loop
10    foreach leg  $l \in \{1, \dots, 6\}$  do
11      if  $\{l\} \cap \mathcal{G}_{swing}$  then
12         $\mathbf{r}_{l,des} \leftarrow \text{CalcNextPose}(\mathbf{r}_{l,curr}, \mathbf{r}_{l,new}, N_{sp}, t)$ 
13        // calculate next leg foot-tip pose in inertial frame
14      else
15         $\mathbf{r}_{l,des} \leftarrow \mathbf{r}_{l,des}$  // hold the current desired foot-tip pose
16     $\mathbf{g} \leftarrow \text{SampleIMU}()$ 
17     $\mathbf{q}_{b,des} \leftarrow \text{CalcBodyPose}(\mathbf{r}_{l,des}, \mathbf{g})$ 
18    foreach leg  $l \in \{1, \dots, 6\}$  do
19       $\mathbf{q}_{l,des} \leftarrow \text{CalcLegIKT}(\mathbf{q}_{b,des}, \mathbf{r}_{l,des}, \mathbf{g})$ 
20     $\text{SetAllServoAngles}(\mathbf{q}_{j,des})$ 
21     $\mathbf{q}_{j,real} \leftarrow \text{ReadAllServoAngles}()$ 
22    foreach leg  $l \in \mathcal{G}_{swing}$  do
23      if  $\text{ContactSensed}() = \text{True}$  then
24         $\mathcal{G}_{swing} \leftarrow \mathcal{G}_{swing} \setminus l$ 
25        // change  $l$ -th leg state from swing to support
26     $t \leftarrow t + T_{con}$ 

```

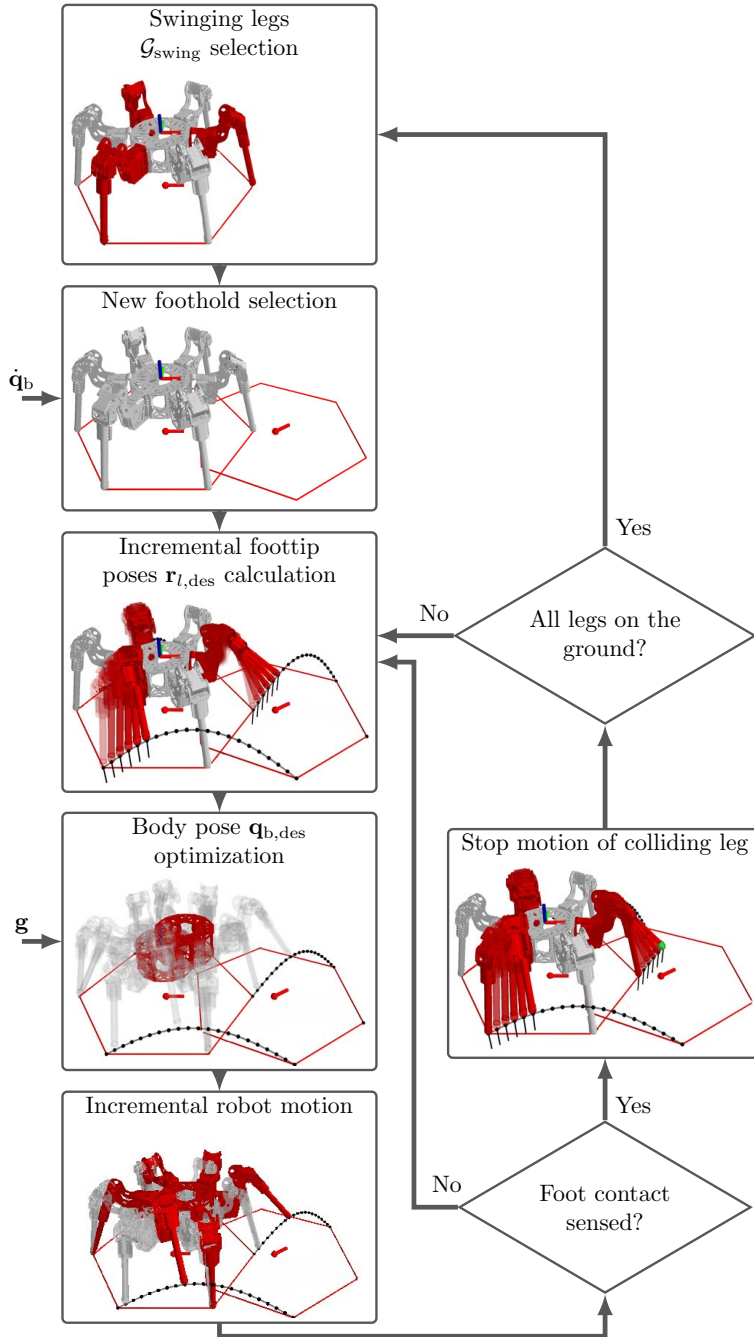


Figure 4.2: Overview of the operation of the proposed decoupled locomotion controller. Note that the actual step length shown in the visualization is unrealizable due to the kinematic constraints and self-collisions; however, it improves the clarity of the explanation. Adapted from [1c].

4. MULTI-LEGGED LOCOMOTION CONTROL

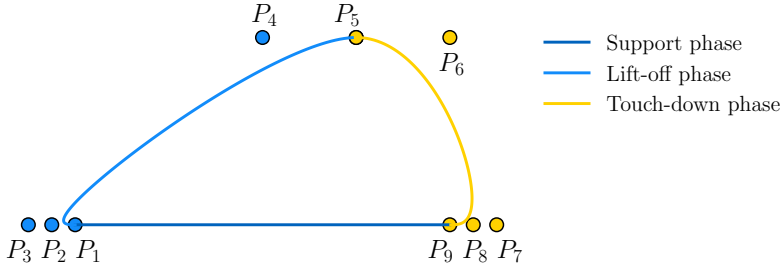


Figure 4.3: The foot tip trajectory as defined by the two Bézier curves and associated control points.

The execution of the gait cycle phase ends when all the legs have swung and their ground contact has been detected. Note that during the continuous locomotion, the joint angles $\mathbf{q}_{l,\text{real}}$ sampled at the end of the previous gait cycle phase are used at the beginning of the next gait cycle phase to calculate the $\mathbf{r}_{l,\text{curr}}$, instead of retrieving new values, as the joint angles readout is due to the communication bandwidth and transport delays the most time-consuming operation.

The immediate desired foot-tip positions $\mathbf{r}_{l,\text{des}}(t)$ at the time t are selected either to hold the current position in the global reference frame when the respective leg is in the support phase, or as one of the intermittent points on the trajectory between the leg current foothold $\mathbf{r}_{l,\text{curr}}$ and the new desired foothold $\mathbf{r}_{l,\text{new}}$. The leg is supposed to reach the new foothold within the time $T_{\text{sp}} = T N_{\text{gp}}^{-1}$. Hence, given the control cycle period T_{con} , there are $N_{\text{sp}} = T N_{\text{gp}}^{-1} T_{\text{con}}^{-1}$ individual poses on the trajectory between $\mathbf{r}_{l,\text{curr}}$ and $\mathbf{r}_{l,\text{new}}$.

We have experimented with different desired leg trajectories, including simple triangle trajectory, square trajectory, the positive amplitude of the sine wave, but the perceivably smoothest motion has been achieved using the Bézier curve trajectory inspired by [67]. More elaborated swing trajectories can be designed considering the leg dynamics, or terrain characteristics [86], [7a]; however, it would require exteroceptive sensing which is not utilized in our setup. Hence, the immediate foot-tip position $\mathbf{r}_{l,\text{des}}(t)$ during the swing phase is computed as two 4th order Bézier curves as it is shown in Figure 4.3.

The desired foot-tip position $\mathbf{r}_{l,\text{des}}(t)$ of the swinging leg at the time t of the gait phase is given as

$$\mathbf{r}_{l,\text{des}}(t) = \begin{cases} s_1^4 P_1 + 4s_1^3 t_1 P_2 + 6s_1^2 t_1^2 P_3 + 4s_1 t_1^3 P_4 + t_1^4 P_5, & \text{for } t \leq \frac{T_{\text{sp}}}{2}, \\ s_d^4 P_5 + 4s_d^3 t_d P_6 + 6s_d^2 t_d^2 P_7 + 4s_d t_d^3 P_8 + t_d^4 P_9, & \text{for } t > \frac{T_{\text{sp}}}{2}, \end{cases} \quad (4.2)$$

$$t_1 = \frac{t}{2T_{\text{sp}}}, \quad \text{and} \quad s_1 = 1 - t_1$$

$$t_d = \frac{t - T_{\text{sp}}}{2T_{\text{sp}}}, \quad \text{and} \quad s_d = 1 - t_d$$

where P_i are the five control points for lift-off and touch-down phases parameterized by the desired swing height h_{swing} , respectively. The control points for the lift-off phase are

$$P_1 = \mathbf{r}_{l,\text{curr}}, \quad (4.3)$$

$$P_2 = \mathbf{r}_{l,\text{curr}} - \frac{1}{16}\Delta\mathbf{r}_l, \quad (4.4)$$

$$P_3 = \mathbf{r}_{l,\text{curr}} - \frac{1}{8}\Delta\mathbf{r}_l, \quad (4.5)$$

$$P_4 = \mathbf{r}_{l,\text{curr}} + \frac{1}{2}\Delta\mathbf{r}_l + [0, 0, h_{\text{swing}}]^T, \quad (4.6)$$

$$P_5 = \mathbf{r}_{l,\text{curr}} + \frac{3}{4}\Delta\mathbf{r}_l + [0, 0, h_{\text{swing}}]^T, \quad (4.7)$$

where $\Delta\mathbf{r}_l = \mathbf{r}_{l,\text{new}} - \mathbf{r}_{l,\text{curr}}$ is the vector between the current and new foothold position. The remaining control points for the touch-down phase are

$$P_6 = \mathbf{r}_{l,\text{curr}} + \Delta\mathbf{r}_l + [0, 0, h_{\text{swing}}]^T, \quad (4.8)$$

$$P_7 = \mathbf{r}_{l,\text{new}} + \frac{1}{8}\Delta\mathbf{r}_l, \quad (4.9)$$

$$P_8 = \mathbf{r}_{l,\text{new}} + \frac{1}{16}\Delta\mathbf{r}_l, \quad (4.10)$$

$$P_9 = \mathbf{r}_{l,\text{new}}. \quad (4.11)$$

The leg foot-tip trajectory is prescribed in the global reference frame, and thus the body pose can be altered without affecting the leg transition in the global reference frame.

The body pose optimization provides the robot body with a smooth motion and distributes its weight evenly among the individual legs, thus reducing the joint torques as it is shown in Figure 4.4. The desired body pose $\mathbf{q}_{b,\text{des}}$ is calculated by exploiting the formulation of kinematics and controller in the inertial reference frame $\{A\}$. The computation of the translational part $\mathbf{r}_{b,\text{des}}$ of the desired body pose reduces to the calculation of the leg foot-tips centroid followed by the projection of CoM in the opposite direction to the normalized gravitational vector \mathbf{g} by the default body height h_{def} as

$$\mathbf{r}_{b,\text{des}} = \frac{1}{6} \sum_{l=1}^6 \mathbf{r}_{l,\text{real}} - h_{\text{def}} \frac{\mathbf{g}}{\|\mathbf{g}\|}. \quad (4.12)$$

The desired rotational part of the body pose Φ_{des} is assigned as the rotation around the z axis by the mean angle between the legs default poses $\mathbf{r}_{l,\text{def}}$ and the current poses $\mathbf{r}_{l,\text{real}}$ as

$$\Phi_{\text{des}} = \begin{bmatrix} 0 \\ 0 \\ \frac{1}{6} \sum_{l=1}^6 \text{atan} \left(\frac{\|\mathbf{r}_{l,\text{def}} \times (\mathbf{r}_{l,\text{real}} - \mathbf{r}_{b,\text{des}})\|}{\mathbf{r}_{l,\text{def}} (\mathbf{r}_{l,\text{real}} - \mathbf{r}_{b,\text{des}})} \right) \end{bmatrix}. \quad (4.13)$$

4. MULTI-LEGGED LOCOMOTION CONTROL

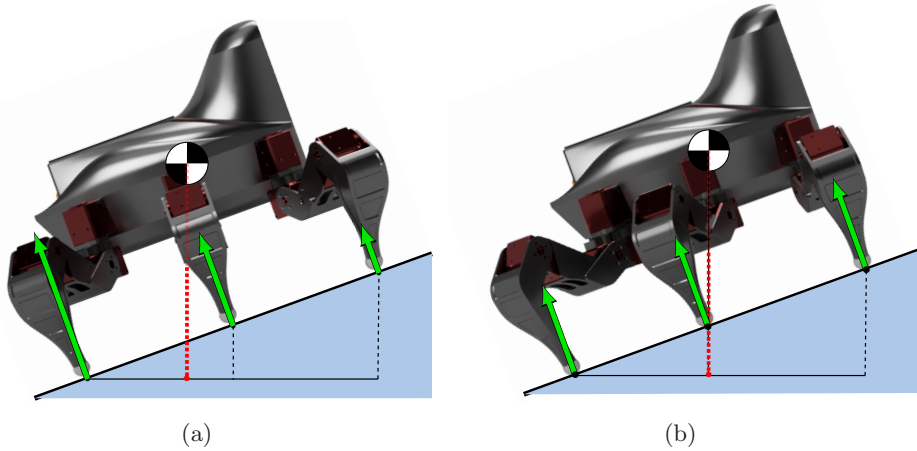


Figure 4.4: The slope adaptation approach and its influence on the robot weight distribution and GRF (visualized as the green arrows). (a) Without the slope adaptation, the CoM is shifted back and the weight is unevenly distributed between the legs. (b) With slope adaptation, the CoM vertical projection is above the legs centroid, and thus the weight is evenly distributed between the legs.

The body pose always follows the legs such that the body movement has a smooth speed profile without abrupt accelerations and decelerations. The mass is distributed evenly among the legs during the stance phase. For the robots with higher number of DoF per leg, like our experimental platform HAntR (depicted in Figure 2.5), a further enhancement is to assign the desired foot-tip orientation vector in the direction of the gravitational vector \mathbf{g} , which is also suggested in [37], [67]. It ensures balanced distribution of the weight between individual legs, and also reduces the joint torques and shear forces applied on the legs. Based on the desired joint angles $\mathbf{q}_{l,\text{des}}$ for each leg and the desired body pose $\mathbf{q}_{b,\text{des}}$, the resulting joint configuration \mathbf{q}_j is calculated using the IKT (see Section 3.1.3), and it is commanded to the joint actuators.

The presented decoupled locomotion approach is specifically developed for position controlled robots and allows seamless integration of different terrain sensing techniques. It also allows for straightforward extension to free-sequence gaits, when the gait sequence \mathcal{G} is not fixed and the selection of the swinging legs is done online. Further, the desired swing trajectory calculation can be readily exchanged for different swing profiles, including profiles computed online based on the perceived terrain irregularities as in the deliberate control approach [7a].

The main drawbacks of the decoupled locomotion control are twofold. Firstly, the input twist command $\dot{\mathbf{q}}_b$ is only sampled once per gait phase at its beginning, which does not allow the robot to change the motion direction mid-phase. Secondly, the execution of the leg swing motion is effectively open-loop, with the contact sensing

being used for stopping the leg motion instantly. Stopping the leg at the instant of contact does not ensure the leg is ready to switch gait phases and support the body in its current configuration, as the contact may occur anywhere along the leg morphology. Hence, despite the behavior works in irregular terrains with majority of the contacts being the expected foot-ground interactions, it is not suitable for heavily cluttered environments. Both of these drawbacks are addressed by the closed-form locomotion controller described in the next section. The experimental evaluation and benchmarking of the proposed controller and its comparison to the closed-form locomotion controller is presented in Section 4.3.

4.2 Closed-form Locomotion Controller

The closed form locomotion controller formalizes the relationship between the leg motion and body motion into a single equation. The controller generates the joint angle trajectory for each individual leg as $\mathbf{q}_l(t) = [\theta_{l,c}(t), \theta_{l,f}(t), \theta_{l,t}(t)]^T$ to satisfy the desired twist vector $\dot{\mathbf{q}}_b(t)$ that defines the locomotion control input as the desired velocity vector.

For each leg $l \in \{1, \dots, 6\}$, we can split the joint angle trajectory to its value and rate using Taylor series

$$\mathbf{q}_l(t + \Delta t) \simeq \mathbf{q}_l(t) + \Delta t \dot{\mathbf{q}}_l(t), \quad (4.14)$$

where we need to establish $\dot{\mathbf{q}}_l$ for the duration of the whole gait cycle including the swing phase and the support phase.

During the support phase, the request for non-slipping feet of the supporting legs yields $\mathbf{r}_l = \mathbf{0}$, and thus given Equation (3.10) we can write

$$\dot{\mathbf{q}}_l = \mathbf{J}_l^{-1} \mathbf{J}_b \dot{\mathbf{q}}_b, \quad (4.15)$$

where \mathbf{J}_l^{-1} is the inverse of the leg Jacobian and \mathbf{J}_b is the body Jacobian.

During the swing phase, the overall leg motion can be expressed as a superposition of the leg forward motion, leg lift motion, and leg stretch control

$$\dot{\mathbf{q}}_l = \mathbf{J}_l^{-1} \mathbf{J}_b \mathbf{Z} \dot{\mathbf{q}}_b + \mathbf{J}_l^{-1} \mathbf{J}_b \mathbf{v}_{sp} + \mathbf{S}(\mathbf{q}_l), \quad (4.16)$$

where \mathbf{Z} is the direction alteration matrix of the twist command $\dot{\mathbf{q}}_b$, as the leg motion during the swing phase is the reverse one of the support phase. Hence, the robot's fore-aft, lateral, and angular velocities are inverted given

$$\mathbf{Z} = \begin{bmatrix} -1 & 0 & 0 & 0 & 0 & 0 \\ 0 & -1 & 0 & 0 & 0 & 0 \\ 0 & 0 & 1 & 0 & 0 & 0 \\ 0 & 0 & 0 & 1 & 0 & 0 \\ 0 & 0 & 0 & 0 & 1 & 0 \\ 0 & 0 & 0 & 0 & 0 & -1 \end{bmatrix}. \quad (4.17)$$

Further, we consider \mathbf{v}_{sp} as the rate along z-axis to lift the legs during the swing phase. The approach allows setting different velocity profiles for the leg swing phase with the constant velocity profile being the straightforward one

$$\mathbf{v}_{sp} = \begin{cases} [0, 0, v_c, 0, 0, 0]^T, & \text{when } t < T_{sp}/2, \\ [0, 0, -v_c, 0, 0, 0]^T, & \text{otherwise,} \end{cases} \quad (4.18)$$

where T_{sp} is the leg swing phase period and the constant v_c determines the upward/downward swing speed.

In addition, we define control function $\mathbf{S}(\mathbf{q}_l)$ to compensate the drift in joint angles and acts as a virtual spring between the current and default leg foothold positions. Without it, the locomotion controller would diverge to singular configurations after several steps.

$$\mathbf{S}(\mathbf{q}_l) = \mathbf{K}_S(\mathbf{q}_{l,\text{def}} - \mathbf{q}_l), \quad (4.19)$$

where $\mathbf{q}_{l,\text{def}}$ is the vector of joint angles at the robot default configuration, and \mathbf{K}_S is the diagonal matrix of the virtual spring coefficients.

Having these terms for each leg and a phase switch function ξ , we can describe a closed-form locomotion controller as

$$\begin{aligned} \mathbf{q}_l(t + \Delta t) \simeq & \mathbf{q}_l(t) + \xi(t)\Delta t \mathbf{J}_l^{-1} \mathbf{J}_b \dot{\mathbf{q}}_b + \\ & \xi(t + T)\Delta t (\mathbf{J}_l^{-1} \mathbf{J}_b \mathbf{Z} \dot{\mathbf{q}}_b + \mathbf{J}_l^{-1} \mathbf{J}_b \mathbf{v}_{\text{swing}} + \mathbf{S}(\mathbf{q}_l)). \end{aligned} \quad (4.20)$$

Note that for any non-singular configuration, the joint trajectories $\mathbf{q}_l(t)$ are generated to satisfy the input twist vector $\dot{\mathbf{q}}_b$. Thus, the locomotion controller supports motion command in all six DoF up to the range of the robot's kinematic capabilities as shown in Figure 4.5.

Switching between the swing and support phases is based on the force threshold-based foot-tip contact detection which monitors the estimated GRF $\mathbf{f}_{\text{GRF},l}$. When the magnitude of the GRF exceeds the given threshold $\|\mathbf{f}_{\text{GRF},l}\| > f_{\text{GRF,thld}}$, the ground is detected and the motion of the leg is stopped, which enables the controller to negotiate terrains with irregular step heights. The gait phase switching is triggered when ground contacts is detected for all the swinging legs.

The main limitation of the controller is inability to select particular footholds. Although the overall posture of the robot can be modified by changing the parameters of the controller, the main idea of the control by the desired twist command is not easily extendable to swing the legs into the particular footholds.

The experimental evaluation of the closed-form controller and its comparison to the decoupled locomotion controller and the groundwork controller [2c] are presented in the following section.

4. MULTI-LEGGED LOCOMOTION CONTROL

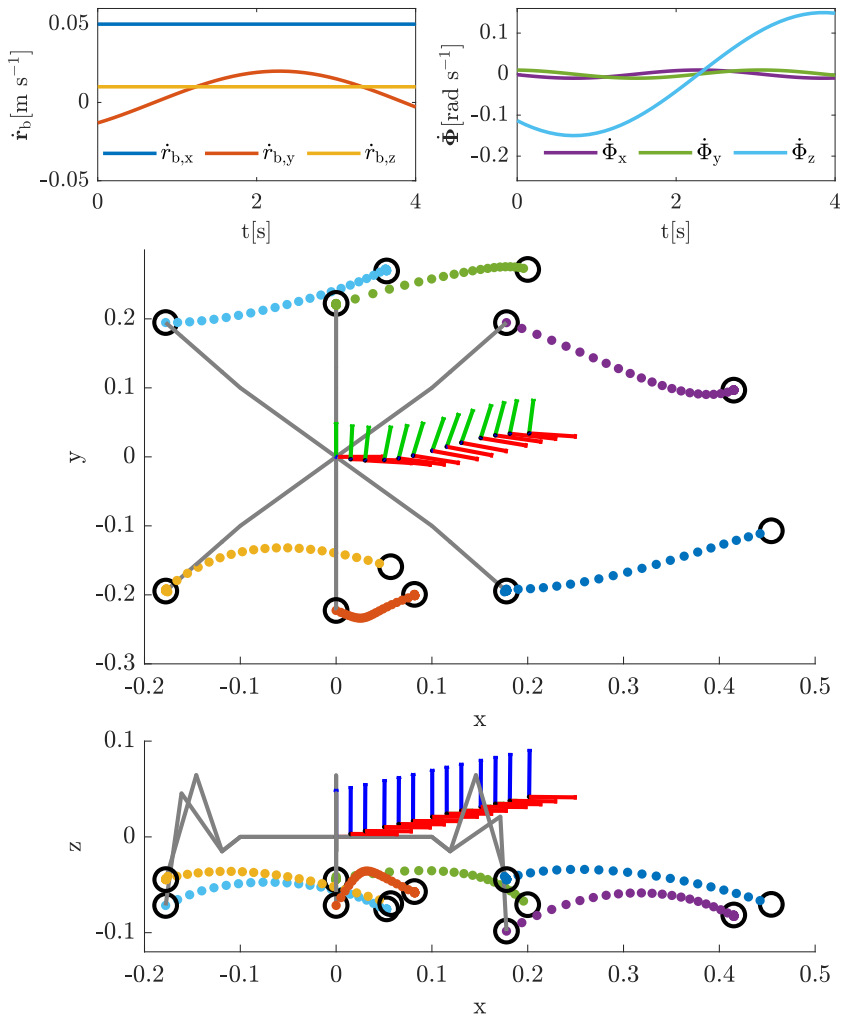


Figure 4.5: Visualization of the robot body and leg motion for a single gait cycle of tripod gait for a complicated velocity command of 4 s duration and irregular terrain locomotion. From top to bottom, there are generated velocity commands; top view of the leg and body trajectories; and side view of the leg and body trajectories. Note, the different start and end heights of the leg trajectories are given by the reaction to the terrain irregularities.

4.3 Controllers Evaluation

The developed locomotion controllers have been implemented and deployed on our experimental platforms. The experimental evaluation of the controllers with evaluation of the smoothness of the body motion is presented in Section 4.3.1. Slope adaptation is presented in Section 4.3.2. Finally, the evaluation of the locomotion performance on flat, irregular, and soft terrains is presented in Section 4.3.3. Note that the quantitative evaluation of the controller performance depends strongly on the used robotic platform, the deployment environment, and the used contact sensing approach. Further, the performance indicators and characteristics are generally not standardized [85]. Therefore, the locomotion control performance has been evaluated with emphasis on highlighting the operation characteristics of the controllers and providing comparison to the groundwork controller [2c].

The decoupled locomotion controller has been deployed on all our experimental platforms, while the closed-form locomotion controller has been deployed only on the SCARAB II platform. Therefore, the quantitative comparison mainly targets the evaluation on SCARAB II platform, but also lists the real-world performance achieved by other platforms. The parameterisation of the controllers used throughout the evaluation is listed in Table 4.1, the other, mostly mechanical, parameters of the experimental platforms are listed in Appendix A. Note that the integral part of the evaluated locomotion controllers is the explicit contact sensing, which allows negotiating individual footsteps and adapting to terrain irregularities. In the following experimental evaluation of the controllers the particular methods of contact sensing do not influence the result as long as their performance is consistent, and thus their detailed description is not a required prerequisite of the presented evaluation. However, for the sake of completeness, we list the used parameterisation of the employed contact sensing approaches in Table 4.1, while their principle of operation and dedicated benchmarking are described in Chapter 5.

Table 4.1: Locomotion control approaches parameterisation.

Parameter		SCARAB I	SCARAB II	HAntR	HEBI Daisy	HEBI Lily
Controller parameters						
Control period T_{con}	[ms]	4.0	4.0	4.0	3.3	3.3
Swing time T_{sp}	[ms]	500.0	500.0	500.0	700.0	700.0
Def. body height h_{def}	[m]	0.12	0.09	0.16	0.21	0.28
Swing height h_{swing}	[m]	0.09	0.09	0.09	0.28	0.28
Swing velocity v_c	[m s ⁻¹]	–	0.1	–	–	–
Contact sensing parameters						
Coxa contact threshold $e_{c,\text{thld}}$	[rad]	0.03	0.03	0.03	–	–
Femur contact threshold $e_{f,\text{thld}}$	[rad]	0.05	0.03	0.05	–	–
Tibia contact threshold $e_{t,\text{thld}}$	[rad]	0.03	0.03	0.03	–	–
Force contact threshold $f_{\text{GRF},\text{thld}}$	[N]	–	1.5	–	3.5	3.5

■ 4.3.1 Body Speed Profile

An important characteristic of rough terrain locomotion is the stability of the robot body and smoothness of its motion. Abrupt motions of the robot’s relatively heavy body can lead to loss of balance due to leg slippage. Abrupt motions also put more stress on the robot’s structure and require higher joint torques for acceleration and deceleration of the platform, which can lead to energy inefficient locomotion.

The body speed profile has been measured on SCARAB II platform as it is currently the only platform implementing the decoupled, closed-form, and groundwork controller [2c] locomotion controllers. During the experiment the robot has been placed on a flat laboratory floor and tasked to locomote for the duration of 30 s with a given velocity command $\dot{\mathbf{q}}_b = [0.1, 0, 0, 0, 0, 0]^T$ using the tripod gait. Parameters of all three controllers were matched according to Table 4.1. The terrain sensing has been disabled during this experiment, assuming the ground contact at the default body height, implying open-loop execution. The motion of the robot has been captured using the external localization system Leica TS-16 total station, which provides ground truth position reference of the robot body \mathbf{r}_b with submillimeter precision and 10 Hz localization rate. The body speed estimate has been computed from the body trajectory as the backward difference using the formula:

$$s(t) \simeq \frac{\|\mathbf{r}_b(t) - \mathbf{r}_b(t - \Delta t)\|}{\Delta t}, \quad (4.21)$$

where $\Delta t = 0.1$ s is the sample time.

Figure 4.6 shows the body speed profiles of the three controllers together with their aggregated statistics represented as five-point summary. The results show a significant improvement between the groundwork controller [2c] and the two proposed controllers with the closed-form controller achieving the smoothest motion. The high variance of the speed for the groundwork controller is caused by its discrete nature with separated body motion and leg motion. For the decoupled controller, the body follows the legs as the CoM projection stays in the leg centroid. Therefore, the particular leg foot-tip trajectory influences the resulting smoothness of the motion given by the speed variance. The closed-form controller formalizes the relationship between the leg motion and body motion with the body motion being prescribed directly by the desired velocity command. Thus, the main source of speed variance is caused by the stiffness of the leg joint actuators and their ability to track the desired joint trajectories.

■ 4.3.2 Slope Adaptation

Dedicated slope adaptation has been proposed for the decoupled locomotion controller. It allows the robot equipped with IMU or AHRS to better cope with the terrain inclinations, slopes, or ridges by adapting the mutual position of the CoM and the support polygon given the direction of the gravitational acceleration

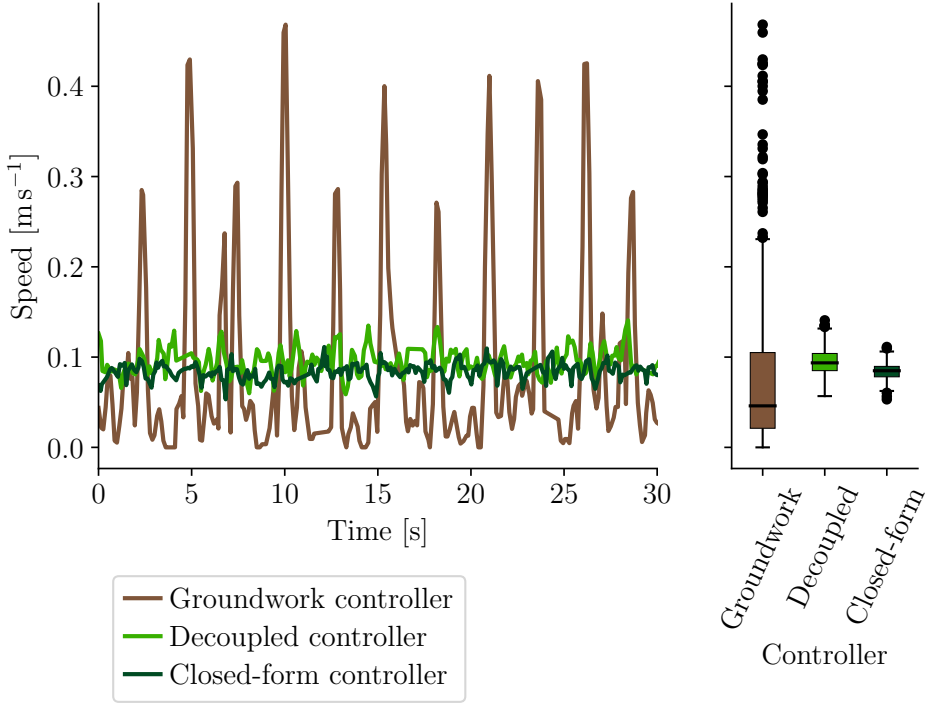


Figure 4.6: Visualization of the robot body speed profiles for the desired robot speed of 0.1 m s^{-1} for the groundwork [2c], decoupled, and closed-form locomotion controllers. (a) body speed *w.r.t.* the time. (b) corresponding aggregated statistics plotted as a five-point summary.

vector \mathbf{g} . The performed experiment evaluates the static and dynamic stability of the SCARAB I, SCARAB II, and HAnTR platforms. During the experimental evaluation, each platform has been placed on a wooden desk with adjustable inclination. The inclination of the desk is monitored with an active marker motion capture system PTI Phoenix Visualeyex III VZ10k with 100 Hz tracking frequency and millimeter accuracy.

During the experiments, the robot has been placed on the desk whose inclination gradually increased until the robot lost its balance. Both the static and dynamic stability of the platforms with the slope adaptation turned on and off have been studied. When the slope adaptation is enabled, the vector of gravitational acceleration \mathbf{g} is obtained by sampling the body mounted [AHRS XSens MTI-30](#), which provides the orientation estimate at a sampling rate of 400 Hz. When the slope adaptation is disabled, the gravitational vector is set to the fixed value of $\mathbf{g} = [0, 0, -9.81]^T$.

During the *static stability test*, the robot does not locomote, while during the *dynamic stability test*, the robot is tasked to locomote in place using the tripod

4. MULTI-LEGGED LOCOMOTION CONTROL

Table 4.2: Slope adaptation evaluation results.

Slope adaptation [†]	<i>Static stability test</i>		<i>Dynamic stability test</i>	
	w/o	w/	w/o	w/
SCARAB I	28°	32°	20°	21°
SCARAB II	25°	30°	21°	23°
HAntR	37°	43°	26°	31°
Lauron V [37] [‡]	–	43°	–	25°
Weaver [36] [‡]	30°	50°	20°	30°

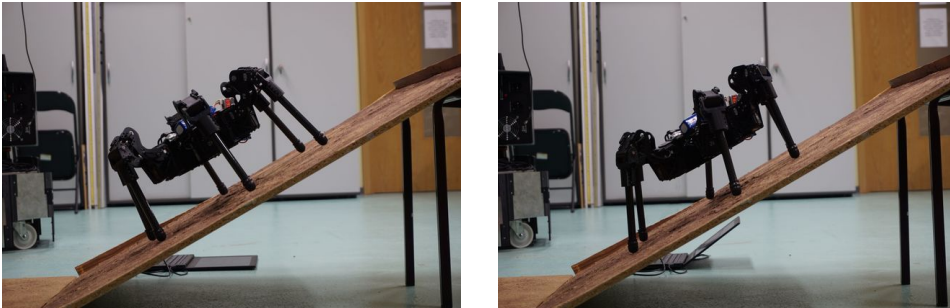
[†] With (w/) and without (w/o) slope adaptation.

[‡] Listed values are reported in the respective cited publications.

gait. All three experimental platforms used the decoupled locomotion controller parameterized according to Table 4.1. The results of the experimental evaluation are reported in Table 4.2 together with the slope adaptation results for comparable six-legged walking robots, Lauron V [37] and Weaver [36], reported by their respective authors.

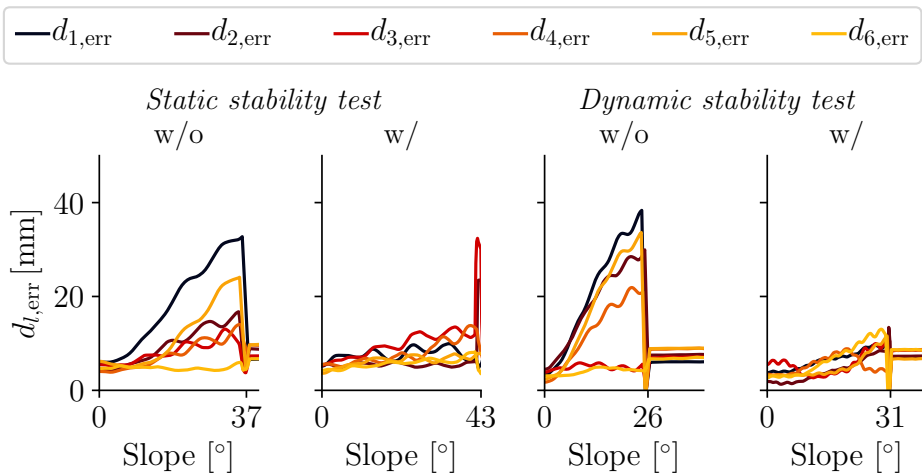
The results show a positive effect of slope adaptation on both the static and dynamic stability of the experimental platforms. Interestingly, during the *static stability test*, SCARAB I achieved better performance than the SCARAB II platform, while in the *dynamic stability test*, the results are opposite. Since SCARAB I is a larger and lighter platform, its legs provide a wider base that benefits static stability. On the other hand, it uses weaker actuators than SCARAB II which most likely causes its comparatively worse performance in the *dynamic stability test*.

The effect is even more noticeable for the kinematically enhanced platforms HAntR and Lauron with four DoF per leg and Weaver with five DoF per leg. On top of the CoM pose adjustment w.r.t. the support polygon, these platforms further allow for setting the ideal foot-tip orientation vector in the direction of the normalized gravitational vector \mathbf{g} . It ensures balanced distribution of the weight between individual legs as suggested and verified by [1c], [36], [37]. The effect of the weight distribution is visualized in Figure 4.7 showing HAntR with and without slope adaptation control enabled together with the corresponding position errors between the desired and current leg poses $d_{l,\text{err}} = \|\mathbf{r}_{l,\text{des}} - \mathbf{r}_{l,\text{real}}\|$. The absolute foot-tip position error is used as the performance indicator because HAntR does not feature force or torque sensors to measure the forces in individual legs directly. Further, at steady-state, the position error is proportional to the joint torque due to the servomotor P-type controller; hence, the chosen performance indicator is valid in such a case. Figure 4.7 supports that the decoupled controller improves the balanced distribution of the weight between the individual legs as there is less variance in the position error between individual legs for the experiment with slope adaptation enabled.



(a) Robot posture w/o slope adaptation.

(b) Robot posture w/ slope adaptation.



(c) Foot-tip position errors $d_{l,\text{err}}$ for individual experiments. From left to right, static stability w/o slope adaptation, static stability w/ slope adaptation, dynamic stability w/o slope adaptation, and dynamic stability w/ slope adaptation.

Figure 4.7: HAnTR slope adaptation evaluation of the decoupled locomotion controller. (a), (b) snapshots of the robot. (c) foot-tip position errors $d_{l,\text{err}}$ for individual experiments.

4. MULTI-LEGGED LOCOMOTION CONTROL

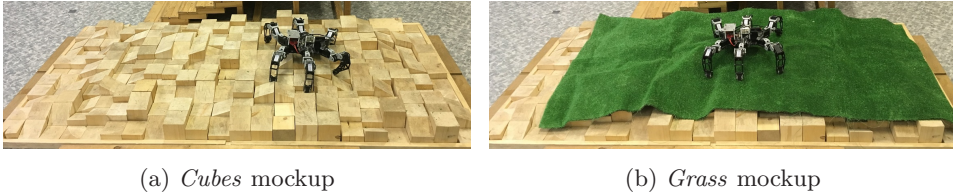


Figure 4.8: *Cubes* and *grass* terrain mockups used for the evaluation of the locomotion controllers performance.

4.3.3 Locomotion Performance

The performance of the developed locomotion controllers has been studied with SCARAB I and SCARAB II platforms on three different types of terrain in laboratory setup. The three used terrain mockups were the flat laboratory floor (denoted *floor*), testbed of the size 2.3×1.0 m composed of squared 0.1×0.1 cm wooden blocks with irregular height and slope, and with the maximum inter-block height difference of 9 cm (denoted *cubes*), and artificial grass laid on top of the testbed, simulating soft terrains (denoted *grass*), as shown in Figure 4.8.

We consider the CoT metric [86] as the locomotion performance indicator. The CoT formulation according to Equation (2.1) is used with the mean electric power \bar{P} , calculated as the average of the instantaneous electric power P estimated from the battery voltage measured by the robot actuators and the current measurements from the dedicated Hall-effect-based current sensor, both measured with the sampling frequency of 250 Hz. The mean speed \bar{v} estimated from the pose tracking data is provided by the active marker motion capture system PTI Phoenix Visualeyex III VZ10k with 100 Hz tracking frequency and millimeter accuracy. The mean speed \bar{v} is calculated from time taken by the robot to traverse the experimental mockup.

During the experiments, each robot was placed in an approximately similar position at the beginning of the given terrain mockup. Then, the robot was manually guided by the operator over the terrain with the fixed linear speed of 0.10 ms^{-1} with an option for the operator to adjust the heading of the robot $\dot{\Phi}_z$ to keep the robot within the terrain mockup. The groundwork controller [2c] and the proposed decoupled controller (Section 4.1), both with position-based contact detection, were used on the SCARAB I and SCARAB II platforms. The proposed closed-form controller (Section 4.2) was used with the force threshold-based contact sensing on the SCARAB II platform.

Each experiment has been performed five times and the mean CoT results with standard deviation for each robot, controller, and terrain are listed in Table 4.3. The presented results indicate an improvement between the groundwork controller [2c] and the two developed controllers, presumably due to the shift from discrete body motion to continuous body motion. The two proposed controllers achieve similar performance with slightly better performance of the closed-form

controller. The difference in **CoT** values between the different terrains is due to the inability of the platform to maintain the desired locomotion speed of 0.10 m s^{-1} over the terrain, rather than a significant increase in power consumption. Finally, the comparison between the experimental platforms indicates that the more powerful actuators and the packed construction of the SCARAB II platform support lower **CoT**, since the power consumption of the robot is similar, although the SCARAB II platform is almost twice as heavy as the SCARAB I.

In comparison to other approaches presented in the literature, the authors of [86] report values of **CoT** around 25 for the locomotion over flat ground with a locomotion speed of 0.10 m s^{-1} using a robotic platform similar to SCARAB I. In [67], which uses the closest approach to the proposed decoupled locomotion controller, the authors report slightly lower **CoT** values around 8.2 compared to the SCARAB II for the target locomotion speed and the tripod insectoid gait. However, the experimental platform Bullet used in [67] is almost twice the size of the SCARAB II platform, and therefore the locomotion at similar speed is achieved with twice the gait cycle time, which implies lower joint torques due to the slower leg swings, and thus correspondingly lower power consumption.

Table 4.3: Locomotion control evaluation results.

Terrain	Controller	$\overline{\text{CoT}}$ [-]	
		SCARAB I	SCARAB II
<i>Flat</i>	Groundwork [2c]	21.56 ± 2.12	12.03 ± 1.08
	Decoupled (Section 4.1)	16.60 ± 1.57	8.93 ± 0.77
	Closed-form (Section 4.2)	–	9.20 ± 0.89
<i>Cubes</i>	Groundwork [2c]	43.30 ± 4.18	23.87 ± 2.15
	Decoupled (Section 4.1)	33.04 ± 2.81	18.72 ± 1.50
	Closed-form (Section 4.2)	–	18.46 ± 1.53
<i>Grass</i>	Groundwork [2c]	32.88 ± 2.96	18.55 ± 1.74
	Decoupled (Section 4.1)	26.00 ± 2.26	14.36 ± 1.30
	Closed-form (Section 4.2)	–	14.05 ± 1.21

4. MULTI-LEGGED LOCOMOTION CONTROL

Chapter 5

Model-based Contact Detection

The main challenge addressed in this work is the interaction of the robot with the environment. This chapter describes a model-based contact detection approach based on monitoring of the virtual elasticity in the robot's joints using position feedback only. The method relies on the derived leg dynamics model, including the actuator and controller model, to estimate the leg motion, which is compared with the actual position of the leg to detect the leg contact events. Detection of leg contact events is critical for terrain negotiation, as failure to detect the contact events results in high loads on the robot's structure and joints. As detailed in Section 2.3, there are many different ways to incorporate sensory feedback into contact event sensing; however, most of these approaches require additional sensory equipment that is not available on affordable robotic platforms, or they work only locally by detecting the contact events only at the foot-tips. Furthermore, additional sensors attached to the legs represent an additional potential failure point in the overall robot design. Therefore, we have based our approach only on the position feedback from the joint actuators. Thus it represents a minimalistic approach to the problem that is applicable to a wide range of robotic platforms. Furthermore, the developed method allows the detection of tactile events anywhere along the leg morphology and in any direction.

The proposed contact event detection approach together with its limitations is described in Section 5.1. The method has been experimentally verified using SCARAB I platform, as it represents an affordable platform equipped with proprioceptive sensing only. First, a contact detection experiment described in Section 5.2 using a single leg has been performed to test the capability of the approach to detect collision at any point of the swing trajectory. Next, the effect of the contact detection on the locomotion performance of the robot has been studied, described in Section 5.3. Finally, Section 5.4 describes the deployment of the proposed approach on a small robotic manipulator. This chapter incorporates material from the publications [2c] and [5a].

5.1 Position Feedback-based Terrain Sensing

The proposed contact event detection is tightly coupled with the position control of the joint actuators and is based on the idea of monitoring the virtual elasticity in the joints using only the position feedback of the joint actuators. For the P-type position-controlled actuators in steady state, the output torque τ of the joint actuator is proportional to the joint angular error err between the desired setpoint

5. MODEL-BASED CONTACT DETECTION

angle and the actual joint angle as it is shown in Figure 5.1a. Therefore, for quasistatic motion, the actuator torque can be directly estimated from the joint angular error and such torque readings can be used in a force threshold-based detection of ground contacts.

It is the main principle of the groundwork [125] which uses a fixed threshold value of the joint angular error of the femur joint to detect contact events only during the vertical swing-down phase of the leg motion. The leg motion is stopped by the threshold-based controller whenever an increase in the joint angular error beyond a certain fixed threshold is detected, to achieve stable locomotion in irregular terrains.

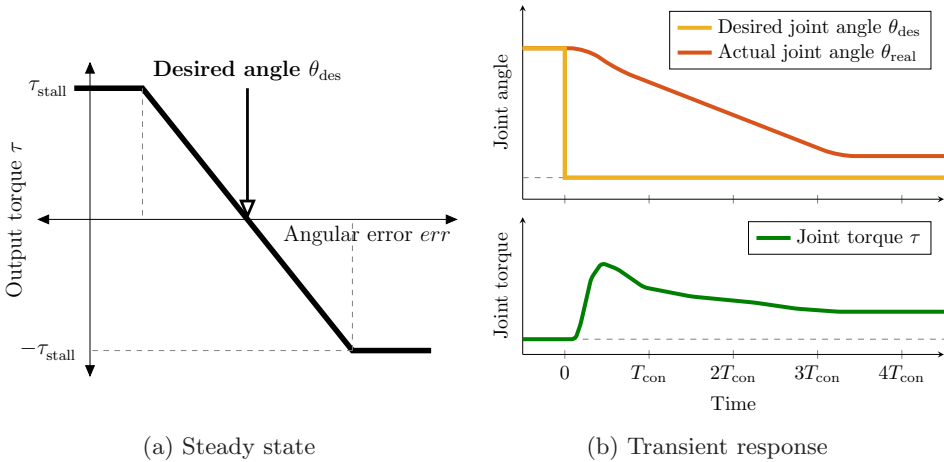


Figure 5.1: Visualization of the relation between the output torque τ and angular error err at (a) steady state and (b) during the transient response to the change in the desired joint angle θ_{des} for the Dynamixel AX12-A actuator. Note, the value of τ is limited by the actuator stall torque value τ_{stall} .

However, when the joint is in motion, the proportional relationship between the torque and joint angular error no longer holds, as it is shown in Figure 5.1b. In addition, the joint angular error depends on various factors, such as controller parameterisation, motion speed, control period and hardware communication latency. On top of that, dynamic effects from other robot links, friction, and other dynamic effects also affect the resulting joint torque values.

Torque observers are used to estimate the joint torque [77] based on the joint torque sensors. However, a direct estimation of the torque τ only from position feedback would require double differentiation, which introduces non-negligible noise into the estimation process [32].

In our approach, we use a high-fidelity leg dynamics model presented in Section 3.2.1 together with the model of actuator dynamics, control loop, and communication (see Section 3.2.2) to model the leg motion and the expected joint angles $\mathbf{q}_{l,est} = [\theta_{l,c,est}, \theta_{l,f,est}, \theta_{l,t,est}]^T$ and compare the predicted angles to the

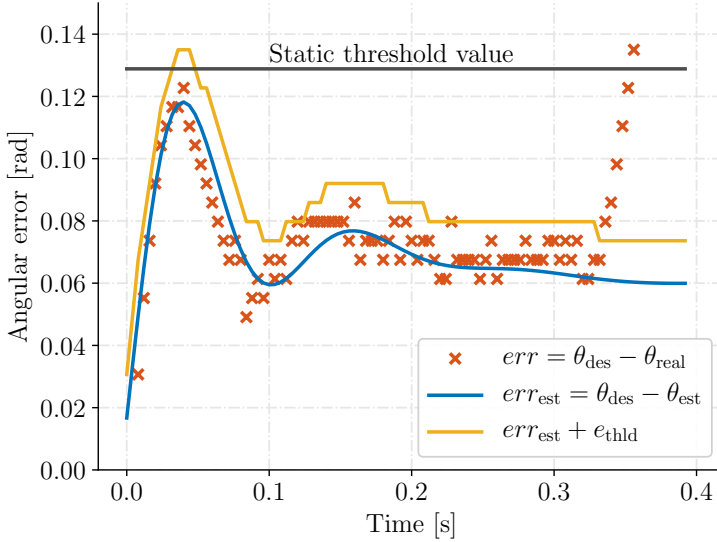


Figure 5.2: Position feedback-based contact detection operation. Example of measured and estimated joint angular errors of the femur actuator during leg motion. The dynamic threshold value is derived from the estimated error increased for three joint angle quantization units and rounded up to take into account imperfections in the model identifications and the joint angle quantization.

actual measured actuator angles $\mathbf{q}_{l,\text{real}} = [\theta_{l,c,\text{real}}, \theta_{l,f,\text{real}}, \theta_{l,t,\text{real}}]^T$. If the absolute difference between the expected and measured joint angles is greater than the static threshold $e_{l,i,\text{thld}}$, the contact event is detected.

The main idea of the proposed method and its comparison with the groundwork [125] is illustrated in Figure 5.2. It shows a single joint actuator error plot between the desired $\theta_{l,i,\text{des}}$ and measured $\theta_{l,i,\text{real}}$ joint angle together with the difference between the desired $\theta_{l,i,\text{des}}$ joint angle and joint angle estimated using the dynamic model $\theta_{l,i,\text{est}}$ where

$$err_{l,i} = \theta_{l,i,\text{des}} - \theta_{l,i,\text{real}}, \quad (5.1)$$

$$err_{l,i,\text{est}} = \theta_{l,i,\text{des}} - \theta_{l,i,\text{est}}, \quad (5.2)$$

are the current measured, and estimated joint angular errors, respectively. As can be seen, the dynamic effects influence the instantaneous angular error value. Furthermore, when the leg makes contact with an obstacle, the **GRF** begins to act on the robot leg causing the joint torque to increase, and thus the joint angular error to diverge. At around time $t = 0.35\text{s}$, the error plot of the measured joint angular error diverges, indicating the presence of a contact event.

The figure also illustrates the fixed threshold and the dynamically set model-based threshold. The dynamically set threshold allows for the detection of contact event six control periods earlier in comparison to the fixed threshold. Hence, the

5. MODEL-BASED CONTACT DETECTION

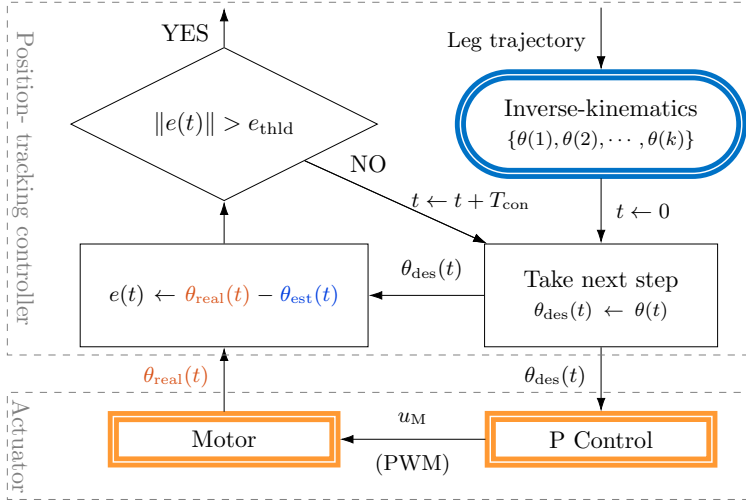


Figure 5.3: Schema of the integration of the proposed model-based contact detection into the motion controller. At every step of the control cycle of a single actuator, a new desired joint angle θ_{des} is retrieved, commanded to the actuator, and used to calculate the estimated joint angle value θ_{est} , that is then compared with the actual joint angle θ_{real} . If the joint angular error is above the given threshold, it is interpreted as the leg motion has been obstructed; otherwise the procedure is repeated for the next iteration.

dynamically set threshold enables faster reaction to the contact event, which, in effect, results in less torque build-up in the joint and therefore its lower wear and tear. Note that the discrete values of the measured $\theta_{l,i,\text{real}}$ are due to the quantization of the joint angle by the real actuator encoder sensor².

The proposed contact detection approach is integrated into the locomotion controller as shown in Figure 5.3. The contact detection is integrated directly into the position tracker, which tracks the desired leg trajectory given by the leg joint angles $\mathbf{q}_{l,\text{des}}(t)$ at the time t of the control loop. In each incremental step of the control cycle, the joint actuators are set with the desired joint angles $\mathbf{q}_{l,\text{des}}$ and their current angles $\mathbf{q}_{l,\text{real}}$ are immediately read by the controller. In parallel, the estimated joint angles $\mathbf{q}_{l,\text{est}}$ are calculated using the leg dynamic model according to Equation (3.60). If the absolute difference between the expected estimated joint angles $\mathbf{q}_{l,\text{est}}$ and the actual joint angles $\mathbf{q}_{l,\text{real}}$ exceeds the predefined fixed threshold value $e_{l,i,\text{thld}}$, the leg contact is detected and the leg motion is stopped. The expected joint angles are estimated with the assumption of no external disturbance.

The particular value of the error threshold is experimentally determined for each robot joint, based on the maximum joint angular error observed for typical collision-

²Real examples from the SCARAB I robot equipped with the Dynamixel AX-12A servos with 10bit joint angle encoders are used in this section.

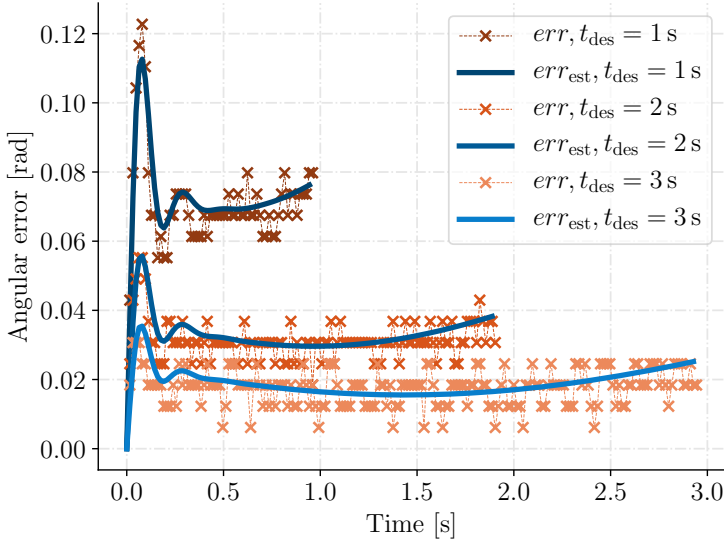


Figure 5.4: Visualization of the motion speed effect on the measured and estimated joint angular error of a single actuator for a similar leg motion with different desired motion execution time t_{des} .

free leg motions as can be observed in locomotion controllers parameterisation in Table 4.1. Such a setting takes into account the quantization precision of the joint encoder and the fidelity of the dynamic model, and maximizes the sensitivity of the proposed approach. For high-fidelity dynamic models, the error threshold collapses to compensation of quantization error of the utilized joint encoder sensor. The approach specifically compares the real and estimated joint angles $\|\mathbf{q}_{l,\text{real}} - \mathbf{q}_{l,\text{est}}\|$ rather than the euclidean distance between the real and estimated foot-tip positions $\|\mathbf{r}_{l,\text{real}} - \mathbf{r}_{l,\text{est}}\|$, as the error threshold for the comparison based on the joint configurations is tighter and inherently considers the quantization of the joint angle by the real actuator encoder sensor. The comparison based on the foot-tip positions would be asymmetric depending on the leg stretch, as for the distant foot-tip positions, it might fall under the available quantization of the joint angle sensor, while being unnecessarily loose for the close positions.

Hence, the main factors influencing the reliability of the proposed approach are the dynamic model fidelity, the control interpolation period T_{con} , and the latency δT between setting the desired joint angle and retrieving the actual joint angle [3a], [5a]. A high-fidelity model allows to set a tighter error threshold $e_{l,i,\text{thld}}$ while allowing for high variation of the locomotion control parameters. The effect of the locomotion speed on the measured and estimated error is shown in Figure 5.4 for three different motion speeds of a similar leg swing. The figure also shows the main drawback of the fixed threshold-based approach [125], which does not scale with changes in locomotion gait parameters, as the joint angular error err can be substantial, especially during rapid leg motions.

5. MODEL-BASED CONTACT DETECTION

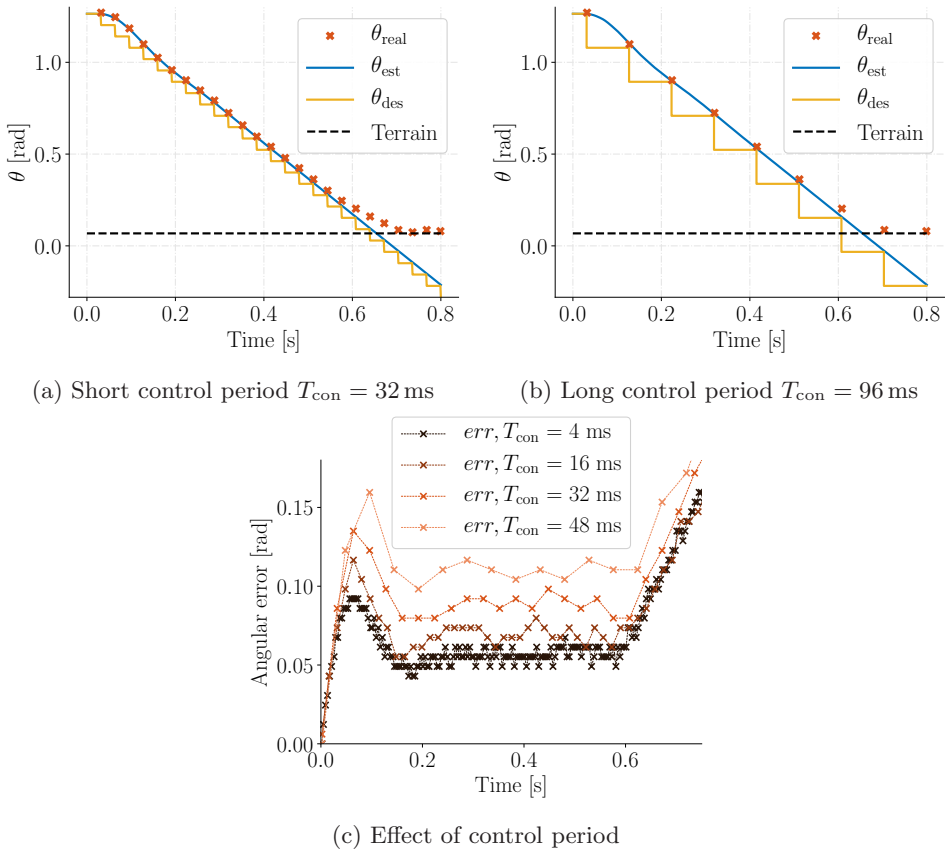


Figure 5.5: Visualization of the control period effect on the desired and real joint angles of the femur actuator for a similar leg motion with (a) short control period $T_{\text{con}} = 32$ ms and (b) long control period $T_{\text{con}} = 96$ ms. (c) effect of control period on the angular error.

The proposed contact detection approach rely on monitoring of the virtual elasticity in the joints caused by the desired commands produced by the locomotion controller; therefore, the two other factors influencing the performance of the proposed approach are the length of the control period T_{con} and the latency δT between setting the desired joint angles and retrieving their actual value. As already shown in Figure 5.1b, there is a dynamic evolution of the torque and also of the joint angular error, whenever the actuator is set with a new desired joint angle θ_{des} . Figure 5.5 shows how the control period T_{con} affects the joint motion and also the evolution of the joint angular error. Especially for longer control period, there are fewer readings throughout the leg motion, and thus higher forces can arise during the leg contact event, which can further cause joint wear and tear, or actuator overheating, but it primarily affects the stability of the locomotion.

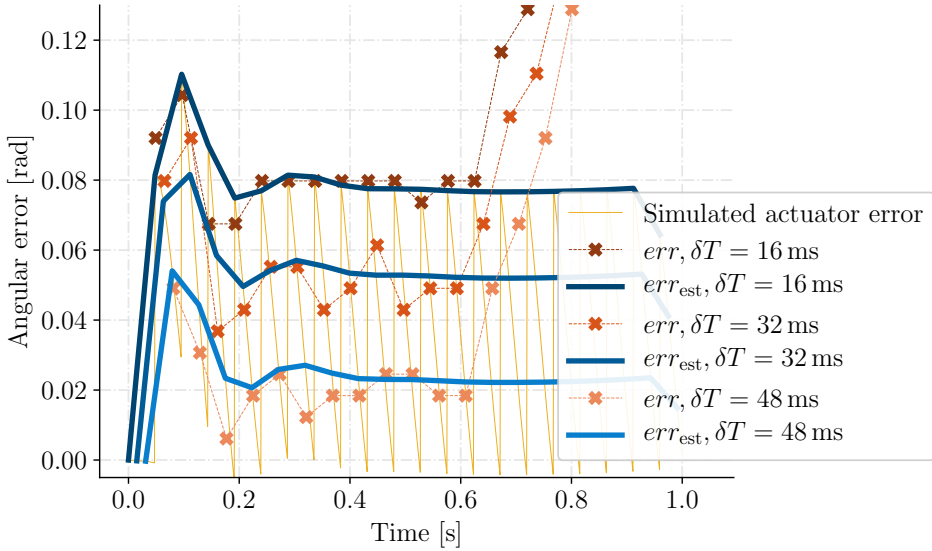


Figure 5.6: Visualization of the latency effect between setting the new desired joint angle θ_{des} and retrieving the current joint angle θ_{real} on the measured and estimated joint angular error of a femur actuator for a similar leg motion but different latencies.

Furthermore, Figure 5.6 shows the effect of the latency δT between commanding the new desired joint angle θ_{des} and retrieving the current joint angle θ on the measured and estimated joint angular error. The latency variations can be observed when retrieving joint angles from multiple actuators simultaneously, which is often realized as a sequential read operation with increasing delay. The figure shows, that with a higher latency, the actuator has more time to drive into the desired setpoint. Therefore, the overall joint angular error is lower, which has to be taken into account during the estimation of the joint angle θ_{est} . The example further signifies the importance of a high-fidelity dynamic model of the leg, together with the model of the joint controller internal operation, including communication interfacing. Notice that the simulated actuator error presented in Figure 5.6 shows the full simulation of the leg dynamic model while err_{est} already assumes correct sampling of the model to match the sampling and latency of the real measurements.

The main benefit of the proposed method is the ability to augment contact sensing to sensory-restricted platforms utilizing only the position feedback of its actuators. It enables the multi-legged platform to negotiate individual footsteps, and thus overcome irregular terrain. The presented results of both the T_{con} and δT influence on the dynamics and subsequent contact detection underline the importance of fast and deterministic control loop in control of multi-legged robots, especially in irregular terrains.

■ 5.1.1 Approach Limitations

The main limitation of the proposed approach is its reliance on a high-fidelity dynamic model of the system. Especially during long-term operation, or deployments in harsh conditions the robot characteristics might change significantly. Automated parameter identification and online adaptation of models are beneficial strategies because they can capture non-stationarities in the mechanical properties of the robot [175]. Such non-stationarities include the adverse changes of the leg parameters such as friction changes due to the joint wear, increased weight of the leg due to the mud deposits, or leg morphology change because of damage. Incorporating dynamic model identification and machine learning-based approaches into the system is considered future work.

■ 5.2 Anyangle Contact Detection

This experiment tests the ability of the proposed approach to detect collision at any point of the swing trajectory. During the experiment, the SCARAB I robot has been elevated so that the robot leg can move freely in the air without colliding with the environment. The leg has been tasked to follow a circular trajectory defined as

$${}^{B_l} \mathbf{q}_{l,\text{des}}(t) = \left[0.15, \frac{1}{2}d \cos(t), \frac{1}{2}d \sin(t) - \frac{1}{2}d \right]^T, \quad (5.3)$$

with the diameter $d = 10$ cm and 1 s motion time that is regularly sampled to 250 desired configurations for the control period $T_{\text{con}} = 4$ ms as shown in Figure 5.7.

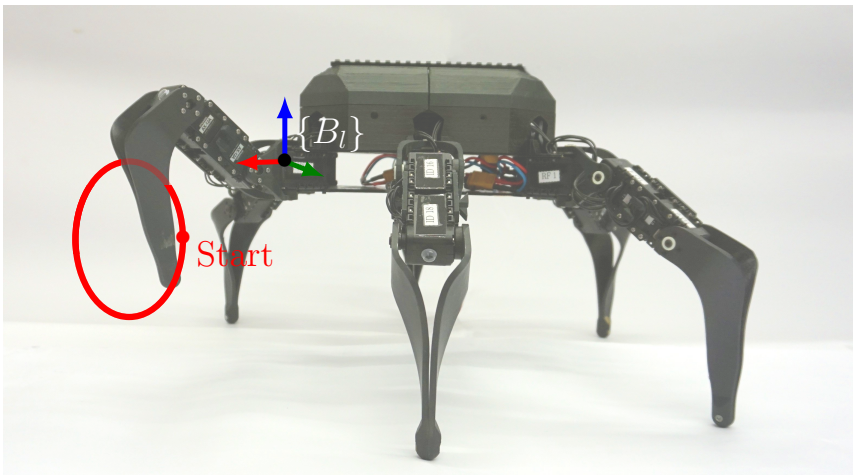


Figure 5.7: Anyangle contact detection experimental setup. The robot has been elevated to support collision-free motion of the leg. The desired circular leg trajectory is shown in red together with its starting point.

Table 5.1: Anyangle contact detection evaluation scenarios description and results.

Scenario	Description	$\sigma(T_{\text{det}})$ [ms]
A1	Collision-free trajectory.	
A2	Vertical obstacle. Collision at 75 % of the trajectory.	19.24
A3	Horizontal obstacle. Collision at 50 % of the trajectory.	12.49
A4	Vertical obstacle. Collision at 25 % of the trajectory.	18.95
A5	Leg motion is obstructed by hand at the beginning.	29.87

Within each control period, the leg position tracking controller sets the actuators with the desired joint angles $\mathbf{q}_{l,\text{des}}$ and retrieves the actual joint angles $\mathbf{q}_{l,\text{real}}$. The error threshold for the experiment has been set to $e_{\text{thld}} = 0.03$ rad.

A dataset consisting of five different scenarios, each with 100 trials, has been collected with the individual scenarios augmenting leg contact at the different part of the leg trajectory, as listed in Table 5.1. Figure 5.8 shows examples of error plots for individual scenarios.

The overall reliability of the detection for scenario A1 has been evaluated to be 91 %, i.e., at nine out of 100 trials the contact detection is triggered, although the scenario is collision free. For the remaining scenarios, we have measured the time to contact detection T_{det} and evaluated its standard deviation $\sigma(T_{\text{det}})$. The standard deviations for each scenario are listed in Table 5.1. Given the control period T_{con} , the resulting values correspond to three to seven control periods to detect the contact event. The results support that the proposed approach allows to detect contact events at any point of the leg swing trajectory.

■ 5.3 Model-based Contact Detection within Locomotion Control

The main goal of the proposed contact detection is to improve the ability of the robot to negotiate individual footsteps and cope with the terrain irregularities. The proposed contact detection has been experimentally verified with the SCARAB I robot with the decoupled locomotion controller described in Section 4.1. Within the controller code given by Algorithm 1, the proposed contact detection approach acts as a method at line number 23, `ContactSensed()`, for stopping the leg motion during the swing phase upon contact of the leg with the environment. Three types of situations occur during the locomotion of the robot *w.r.t.* the explicit contact detection. Namely, early, in-time, and late contact detection. The desired mode of operation is the in-time contact detection where the contact is detected as soon as it appears. On the other hand, the early and late contact detection negatively affect the robot attitude and the torques in the robot joints. It can be critical for

5. MODEL-BASED CONTACT DETECTION

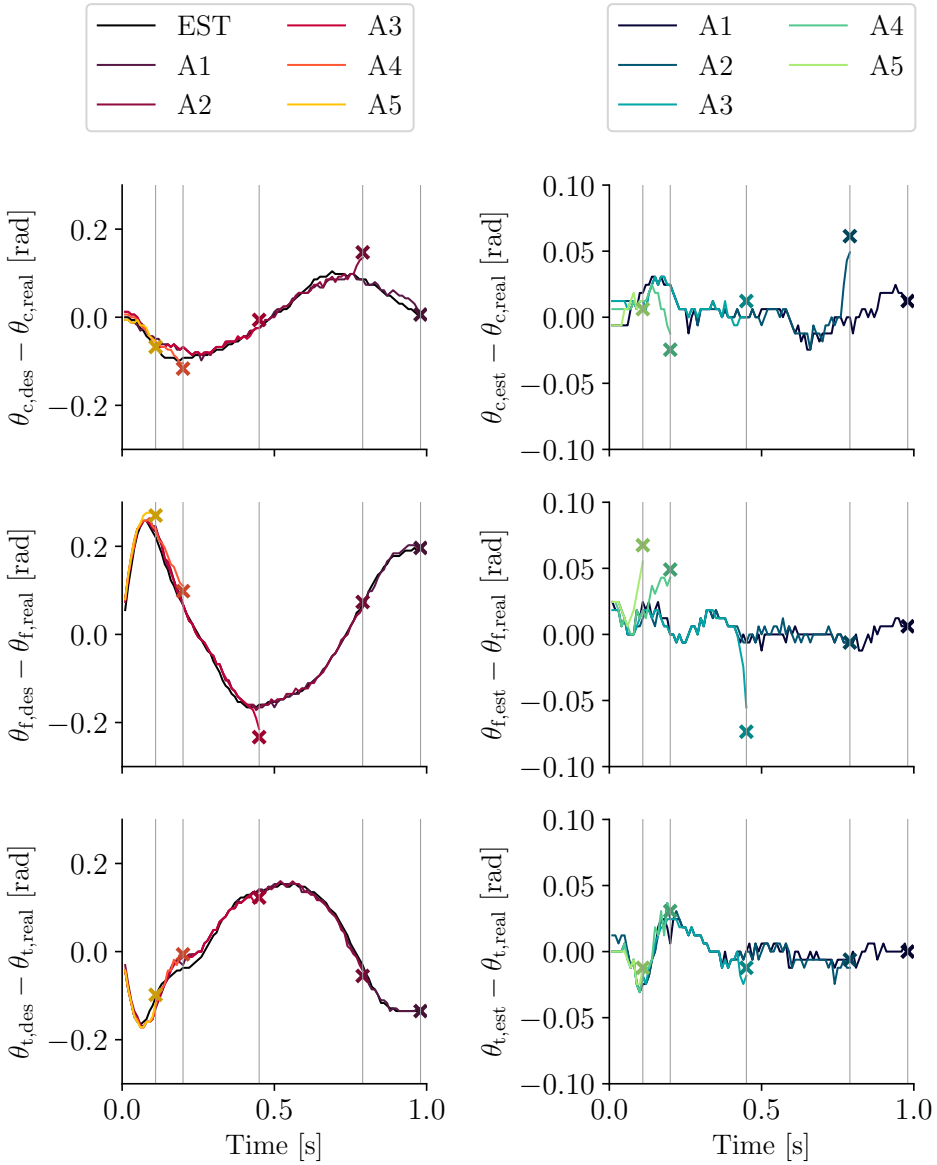


Figure 5.8: Anyangle contact detection experiment. Example of the error plots for individual joints in experimental verification of the proposed anyangle tactile detection on a circular trajectory using $e_{thld} = 0.03$ rad for the individual scenarios. From top to bottom, the error plots of coxa, femur, and tibia joints. The vertical lines in the plot represent the instant of collision detection for individual scenario examples.

the position controlled platforms without joint torque feedback, which can cause damage to the platform because of the undetectable excessive joint torques.

The early contact detection stops the leg motion while the leg is still in the air, resulting in a posture change and possible loss of balance in the following gait phases. Note that the posture change does not have to manifest itself immediately during the following gait phase but depending on the selected locomotion gait. It can manifest itself up to five gait phases later in the case of a six-legged robot walking using the pentapod locomotion gait. The late contact detection affects the robot attitude immediately as the increased GRF of the leg that failed to detect the contact is immediately reflected by the attitude change of the robot.

Hence, in the experimental evaluation we study the stability of the SCARAB I platform during locomotion. The robot has been tasked to locomote in place on a flat laboratory floor for 100 gait cycles of the decoupled locomotion controller (Section 4.1) using the tripod locomotion gait with the parameterisation according to Table 4.1. During the locomotion it collects the attitude data using XSens MTi-30 AHRS with 400 Hz sampling rate. Variance in the roll $\text{Var}(\Phi_x)$, and pitch $\text{Var}(\Phi_y)$ angles, and variance in the vertical acceleration $\text{Var}(\ddot{r}_{b,z})$ of the platform within each gait cycle are used as the performance indicators. Stable locomotion with reliable contact detection is characterized by low variance in the observed indicators. Therefore, we use an open-loop locomotion without contact detection as the baseline, as it knows exactly the height of the floor, and therefore it provides the lowest variance of the indicators.

Figure 5.9 shows the five-point summary for individual indicators for baseline without the ground detection, groundwork approach [125] utilizing the fixed threshold value of $e_{\text{thld}} = 0.06$ rad, and the proposed model-based contact detection approach with the threshold values $e_{c,\text{thld}} = 0.03$ rad, $e_{f,\text{thld}} = 0.05$ rad, $e_{t,\text{thld}} = 0.03$ rad. The results indicate that the proposed approach provides smoother locomotion in comparison to the groundwork approach utilizing the fixed detection threshold. Furthermore, the small variance difference between the baseline locomotion with perfect information about the terrain height and the proposed approach supports the feasibility of the proposed approach in augmenting contact sensing to sensory-restricted platforms like SCARAB I robot.

■ 5.4 Contact Detection with Robotic Manipulator

The proposed model-based contact detection approach has been deployed on an affordable off-the-shelf robotic manipulator Rotrics Dexarm with three DoF shown in Figure 5.10. The robotic manipulator shares the same morphology as the legs of our multi-legged platforms, thus a similar dynamic model can be used to determine the estimated configuration of the arm θ_{est} . Furthermore, the robotic manipulator features independent joint angle encoder sensors that provide the required joint angle feedback, but unlike our multi-legged platforms, it uses stepper motors for

5. MODEL-BASED CONTACT DETECTION

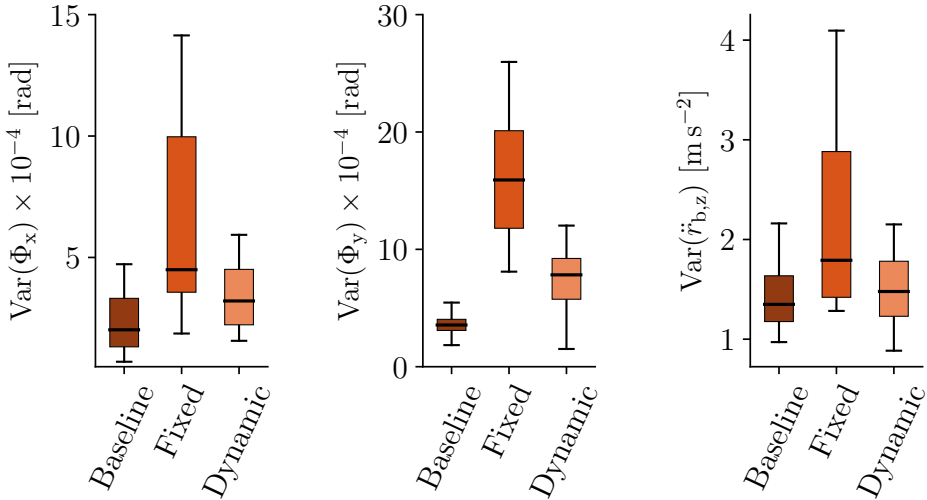


Figure 5.9: Evaluation of robot stability in contact detection during locomotion. Five-point summary of the variance in roll and pitch angles, and vertical acceleration of the robot body in baseline locomotion without contact detection, groundwork approach [125] utilizing the fixed threshold, and the proposed model-based contact detection approach.

actuation. The parameters of the used manipulator are listed in Table A.3 in Appendix A.

The used actuator model formalized in Equation (3.51) described in Section 3.2.2 can be substituted for the full stepper motor model such as presented in [176]. However, a sufficiently precise relation between the joint actuator command and joint angle trajectory is required to use the proposed contact detection approach. Note that the stepper motors are controlled in individual steps (microsteps) in an open-loop fashion. The internal manipulator controller first calculates the required number of steps to reach the new desired manipulator configuration \mathbf{q}_{new} from the current configuration \mathbf{q}_{curr} . Then, it executes the motion with a pre-defined trapezoid velocity profile that causes the velocity of the manipulator to ramp-up to the transfer speed and maintain the transfer speed. Finally, it slows down to stop at the desired configuration.

The output torque of the stepper motor is given as a function of the stepping rate, where the amount of the incremental motor torque $\tau_{\mu\text{step},M}$ generated per microstep can be expressed a:

$$\tau_{\mu\text{step},M} = \tau_{\text{step},M} \sin \frac{\pi}{N_{\text{poles}} N_{\mu\text{step}}}, \quad (5.4)$$

where $\tau_{\text{step},M}$ is the holding torque per full step, N_{poles} is the number of the motor pole pairs, and $N_{\mu\text{step}}$ is the number of the microsteps per full step. During the



Figure 5.10: Affordable robotic manipulator Rotrics DexAm used for deployment of the proposed model-based contact detection approach.

motion, the microstepping actuator needs to accumulate enough torque to overcome the rotor friction and load inertia, for the rotor to advance.

The described behavior is shown in Figure 5.11a that highlights the high repeatability of the manipulator motions between the fixed start configuration \mathbf{q}_{curr} and fixed new desired configuration \mathbf{q}_{new} . The maximum measured configuration difference $err = \mathbf{q}_{\text{des}} - \mathbf{q}_{\text{real}}$ for the individual trials gives us the estimate for best achievable e_{thld} . For the utilized robotic manipulator it is $e_{\text{thld}} = 0.006$ rad. For the motions originated from a different \mathbf{q}_{curr} , but with similar configuration difference $\mathbf{q}_{\text{curr}} - \mathbf{q}_{\text{new}}$, the motion is affected by the dynamic effects as it is shown in Figure 5.11b. Due to the low inertia and relatively low speed of the manipulator motions, a static detection threshold $e_{\text{thld}} = 0.03$ rad for error $err = \mathbf{q}_{\text{des}} - \mathbf{q}_{\text{real}}$ can be used directly without taking into account the dynamics of the robotic manipulator. Such error threshold is still lower than the joint angle error that would cause synchronism lost for the used stepper motors.

As the stepping rate of the actuator is known and there is no gearbox on the output shaft of the motor, we can substitute Equation (3.58) with the linearized model of the stepper motor dynamic characteristics [177]:

$$\boldsymbol{\tau}_l \simeq \boldsymbol{\tau}_{\text{step},M} - \mathbf{K}_{\text{step}} \dot{\mathbf{q}}_l, \quad (5.5)$$

where \mathbf{K}_{step} is a diagonal matrix of the linear coefficients that can be found experimentally. The adjusted leg dynamic model can be then used in the estimation

5. MODEL-BASED CONTACT DETECTION

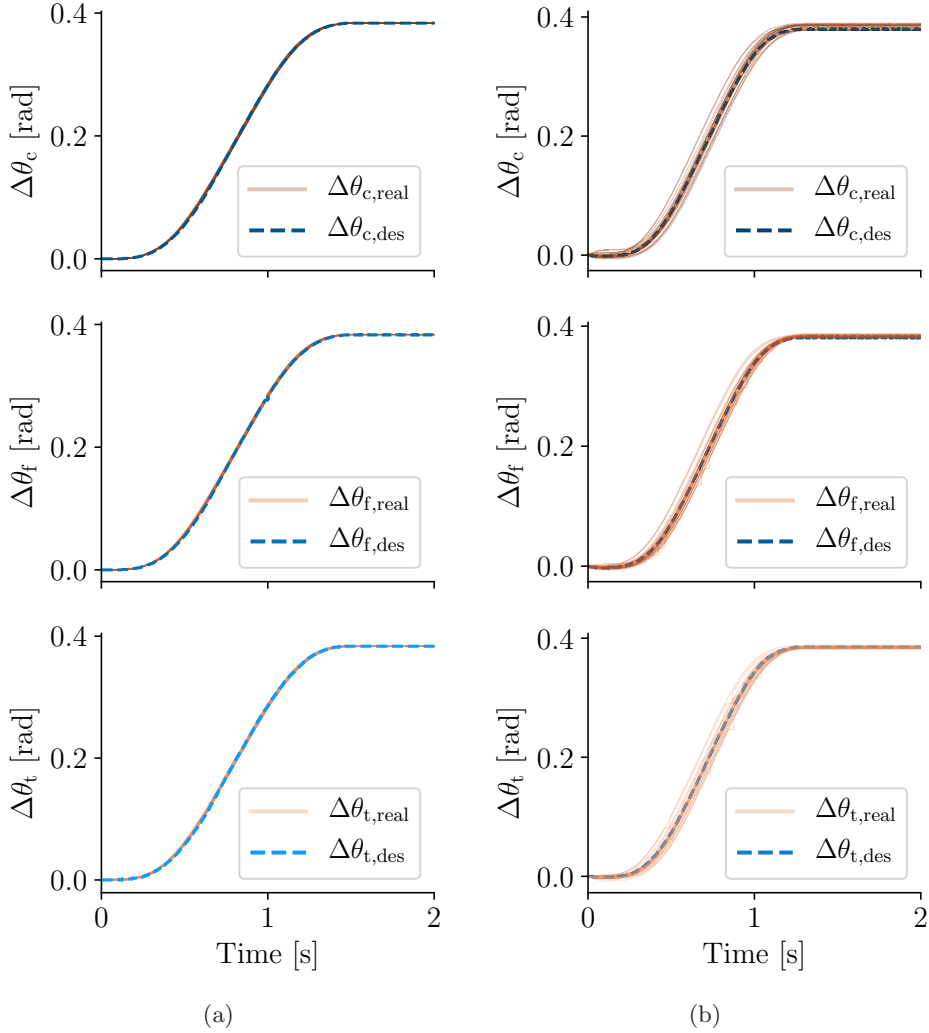


Figure 5.11: Example of the repeatability for 25 manipulator motions of similar configuration difference of $\Delta\theta_i = 0.38$ rad of every joint, for motions from (a) similar configuration, and (b) different configurations within the robot workspace.

of \mathbf{q}_{est} and detection of the contact similarly to the proposed approach.

Figure 5.12 shows an example of the contact detection using the proposed method with the set error threshold of $e_{\text{thld}} = 0.012$ rad. The experimental results support the generality of the proposed contact-detection approach in augmenting tactile sensing to different platforms.

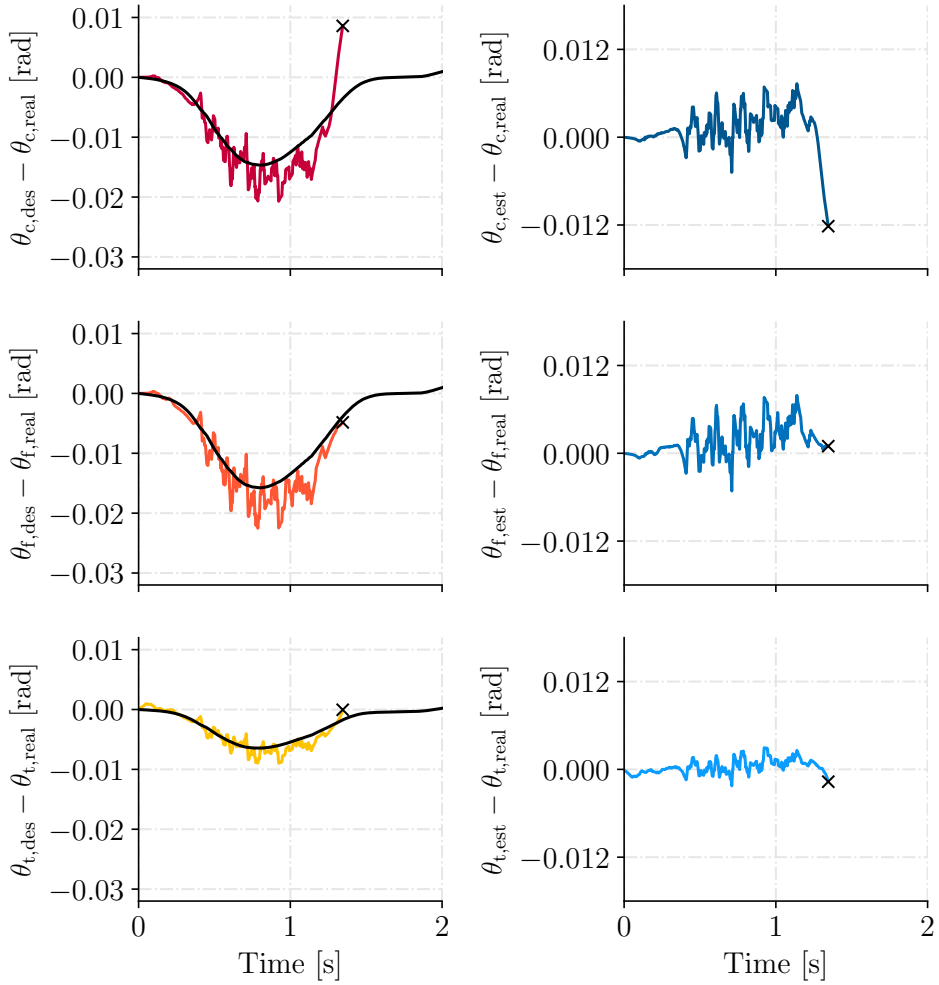


Figure 5.12: Contact detection with the small robotic manipulator. The error plots for individual joints of the robotic arm with collision detection visualization using $e_{thld} = 0.012$ rad at coxa joint.

5. MODEL-BASED CONTACT DETECTION

Chapter 6

Model-based External Wrench Estimation

As the robot interactions with the environment are not limited only to legs, we have developed an approach for continuous external wrench estimation using proprioceptive sensing. The approach utilizes the derived whole-body dynamic model of the robot described in Section 3.2.3 and provide an analytical formula for deriving the external wrench and GRF.

The proposed approach is detailed in Section 6.1 followed by the experimental evaluation. The approach requires joint torque measurements and therefore it has been primarily developed and tested on the SCARAB II platform described in Section 2.2. Furthermore, the developed approach has been deployed on the HEBI Lily platform as well, that further supports the generality of the proposed approach. The experimental setup is described in Section 6.2, followed by the verification of the model simplifications introduced during the deriving of the whole-body dynamic model of the robot presented in Section 6.3. Finally, the results of the experimental evaluation of the wrench estimation on the SCARAB II robot controlled by the proposed closed-form locomotion controller and HEBI Lily robot controlled by the decoupled locomotion controller are presented in Section 6.4 and Section 6.5, respectively.

6.1 External wrench estimation

The analytical solution for the estimation of the external wrench acting on the robot body $\tau_{e,b}$ is formulated from the whole-body dynamic model described by Equation (3.80) as:

$$\begin{aligned} \tau_{e,b} = & \sum_{l=1}^6 \mathbf{J}_b^{TB_i} \mathbf{R}_B^B \mathbf{R}_A \mathbf{f}_{\text{GRF},l} - \left(\mathbf{M}_b + \sum_{l=1}^6 \mathbf{M}_{b,l} \right) \ddot{\mathbf{q}}_b - \\ & \sum_{l=1}^6 \mathbf{M}_{b,j,l} \ddot{\mathbf{q}}_l - \sum_{l=1}^6 \mathbf{M}_{G,b,l} \mathbf{g} - \mathbf{C}_b \dot{\mathbf{q}}_b - \mathbf{G}_b. \end{aligned} \quad (6.1)$$

Equation (6.1) shows that the calculation of the external wrench is based on the GRF of individual legs $\mathbf{f}_{\text{GRF},l}$ and the robot state \mathbf{q} . The GRF $\mathbf{f}_{\text{GRF},l}$ can be obtained either directly using the dedicated force/torque sensors in robot ankles [170], [171], which greatly simplifies the estimation process, or we can estimate them from joint torques τ_j using Equation (3.81). The joint torques can be estimated using

the joint actuators' current, as it is done in our experimental evaluation using SCARAB II platform, from slip of the elastic element in SEA actuators, or directly measured using dedicated torque sensors in robot joints.

The generalized body coordinates $\mathbf{q}_b, \dot{\mathbf{q}}_b, \ddot{\mathbf{q}}_b$ required to calculate the external wrench can be obtained using various approaches to robot state estimation. In our experimental evaluation we utilize the joint positions and commanded velocity to estimate the generalized body coordinates under the assumption of fixed footholds.

6.2 Benchmarking Setup for External Wrench Estimation

The experimental evaluation is based on applying known external wrench $\hat{\boldsymbol{\tau}}_{e,b} = [\hat{F}_x, \hat{F}_y, \hat{F}_z, \hat{\tau}_x, \hat{\tau}_y, \hat{\tau}_z]^T$ on the robot, and examining the estimated wrench $\boldsymbol{\tau}_{e,b} = [F_x, F_y, F_z, \tau_x, \tau_y, \tau_z]^T$. Each component of the external wrench $\boldsymbol{\tau}_{e,b}$ including fore-aft F_x , lateral F_y , and vertical F_z forces, and torques about each major axis τ_x , τ_y , and τ_z is examined individually. The wrench estimation has been verified in flat and irregular terrain locomotion, showing the ability of the proposed method to estimate the acting wrench while the robot is in motion.

The experimental testbed is to provide repeatable conditions for the experimental validation of the external wrench estimation. The benchmark setup consists of the robot operational area formed by a table, a rigid frame enclosure with 109×120 cm size and adjustable height built from 4 cm aluminum profiles, and a set of weights on a cord for inducing known external wrench $\hat{\boldsymbol{\tau}}_{e,b}$ on the robot. The area of the testbed is observed with active marker motion capture system PTI Phoenix Visualeyex III VZ10k with 100 Hz tracking frequency and millimeter accuracy. The motion capture system tracks the mutual position of the cord attachment point on the robot and the pulley. It provides the yaw orientation of the robot Φ_z w.r.t. the pulley, and thus the ground-truth of the acting wrench $\hat{\boldsymbol{\tau}}_{e,b}$.

Two experimental setups depicted in Figure 6.1 have been prepared to examine the performance of the external wrench estimation on flat and irregular terrains. The irregular terrain area is formed by 0.1×0.1 m wooden blocks with irregular height and slope, and with the maximum inter-block height difference of 9 cm. The external wrench $\hat{\boldsymbol{\tau}}_{e,b}$ has been induced on the robot by attaching different weights suspended on a cord over the edge of the rigid frame using a pulley as shown in Figure 6.1c. The purpose of the pulley is to eliminate the friction of the cord. The attachment handle on the robot, depicted in Figure 6.1d, is mounted about 10 cm above the robot CoM, providing three attachment points. In particular, one is in the middle of the handle for inducing the fore-aft and lateral forces on the robot, and two others are on the sides, both 10 cm apart from the center, for torque-inducing experiments. Five wooden blocks with the weight \hat{F}_w from the set {730 g, 754 g, 1247 g, 1253 g, 2019 g} have been used as suspended weights, see Figure 6.2.

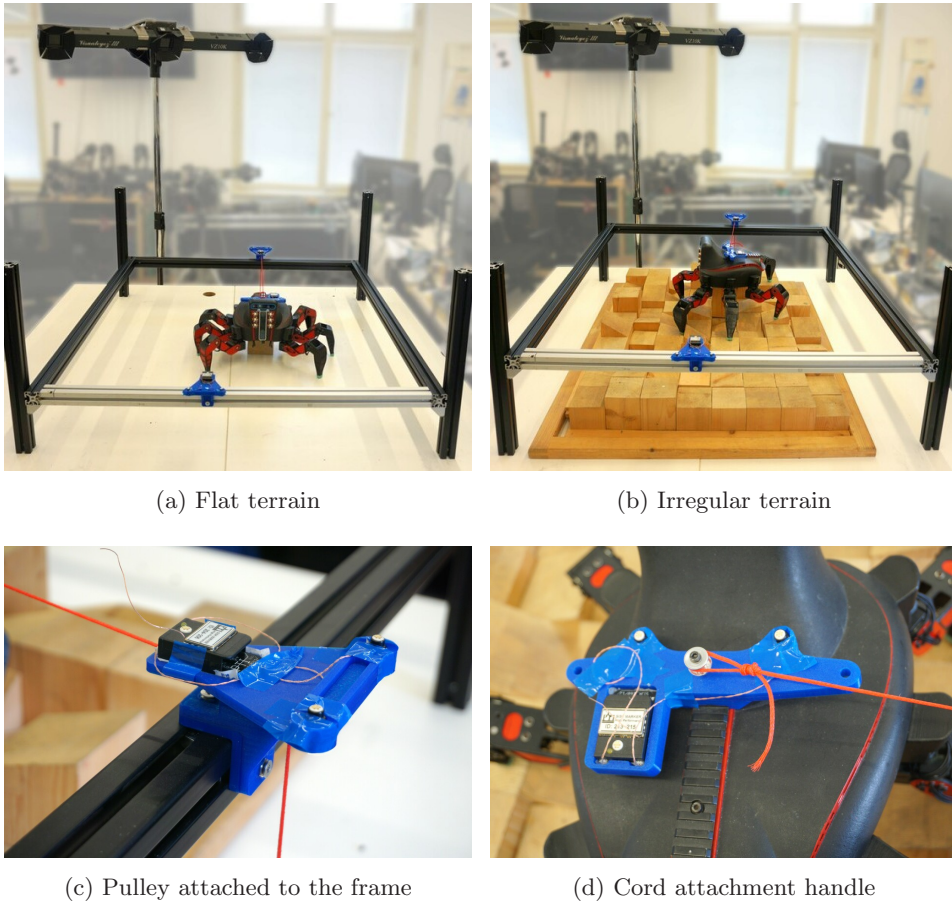


Figure 6.1: Experimental testbed for acting wrench estimation with the motion tracking system. Both the pulley and cord attachment handle have attached active motion tracking markers.

6.3 Verification of the Dynamic Model Simplifications

The baseline values of $\tau_{e,b}$ have been measured with the robot standing (the vertical velocity of the swinging legs set to 0), locomoting in place with zero velocity command, and locomoting with the maximum forward velocity $\dot{q}_b = [0.15, 0, 0, 0, 0, 0]^T$ on the flat terrain, named as experiments B1, B2, and B3, respectively. No explicit external wrench has been induced on the robot. The estimated value of $\tau_{e,b}$ has been measured for 10 s. The estimated baseline external wrench is shown in Figure 6.3, and the mean values with standard deviations are listed in Table 6.1.

6. MODEL-BASED EXTERNAL WRENCH ESTIMATION



Figure 6.2: The set of weights used in the experimental evaluation of acting wrench estimation.

Table 6.1: Baseline values of the estimated wrench $\tau_{e,b}$.

$\tau_{e,b}$ component	B1	B2	B3
\bar{F}_x [N]	-0.02 ± 0.02	-0.01 ± 0.09	-0.10 ± 0.13
\bar{F}_y [N]	-0.05 ± 0.06	-0.21 ± 0.26	-0.33 ± 0.31
\bar{F}_z [N]	-0.22 ± 0.21	-0.44 ± 0.38	-0.55 ± 0.48
$\bar{\tau}_x$ [N m^{-1}]	0.00 ± 0.00	0.01 ± 0.02	0.01 ± 0.02
$\bar{\tau}_y$ [N m^{-1}]	-0.00 ± 0.01	0.02 ± 0.02	0.02 ± 0.02
$\bar{\tau}_z$ [N m^{-1}]	0.00 ± 0.00	0.01 ± 0.02	0.01 ± 0.02

The results show that the mean values are not exactly zero because of the subtle parameter differences between the individual legs. There are also fluctuations in the estimation, partly caused by the sensory noise, as the joint torques are estimated from the servomotor current. The fluctuations are consistent with the locomotion gait cycle that can be observed as individual peaks in the data. It signifies the importance of further filtering the estimations, which we consider for future work. Further, the fluctuations in the experiment B1 are presumably caused by the utilized control approach detailed in Section 4.2. The stillstand is enforced by setting zero leg lift-off velocity, which still internally cycles between the triplets of swinging legs that are considered swinging until the force threshold ground contact is triggered. As can be seen from the results, the difference between the wrench estimation of the robot locomoting in place and locomoting with full forward velocity is negligible; hence, the introduced whole-body dynamic model simplifications of negligible Coriolis and centripetal effects of the leg motion are justified by the results.

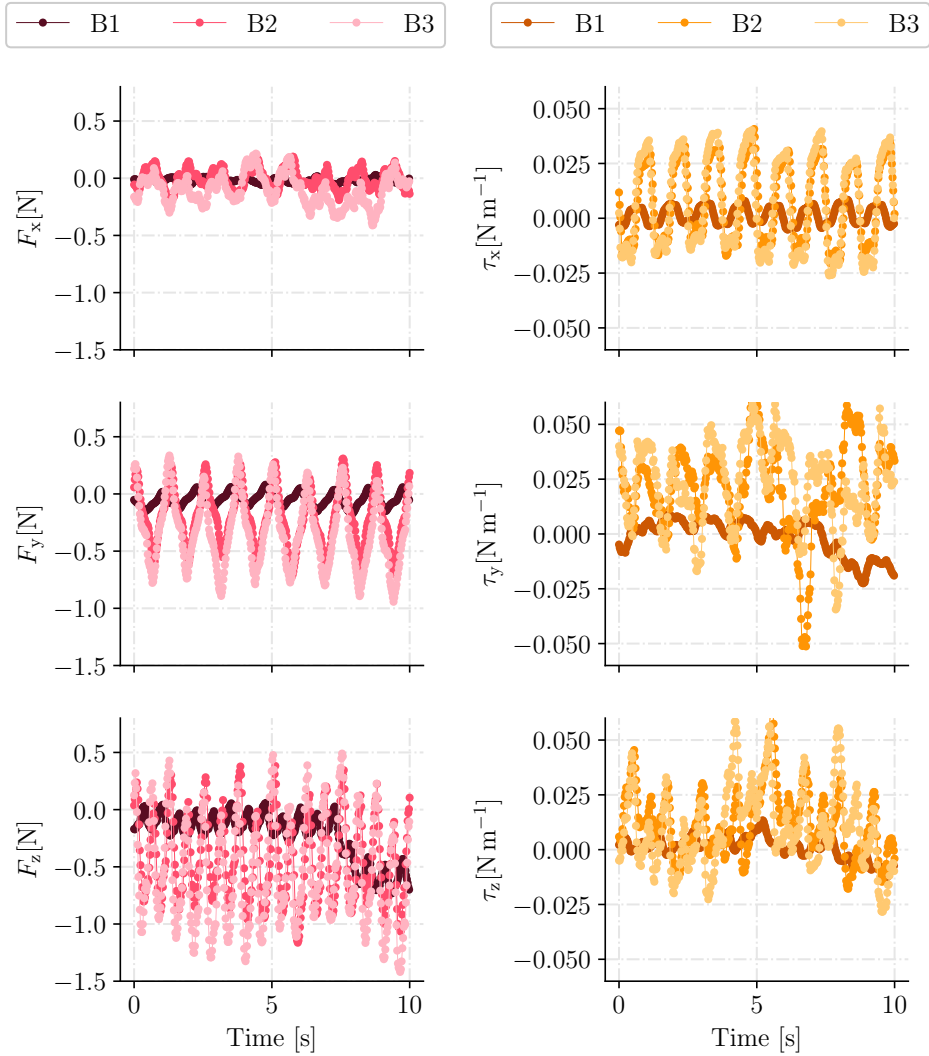


Figure 6.3: Raw, unfiltered, measured values of the estimated wrench $\tau_{e,b}$ without the acting wrench in the experiments B1, B2, and B3.

6.4 External Wrench Estimation on the SCARAB II Robot

The evaluation is based on examining the estimation of each component of the external wrench $\tau_{e,b}$. Altogether twenty different experimental trials have been performed with half of the trials performed on the flat and half on the irregular terrains denoted F and I, respectively. The trials are organized in three scenarios based on the principal acting component of the external wrench in that scenario.

6. MODEL-BASED EXTERNAL WRENCH ESTIMATION

The scenarios estimating the acting force (Scenario 1); torques (Scenario 2); and payload weight estimation (Scenario 3) are denoted F, T, and W for the reference, respectively.

During all the performed experiments, the robot locomotes in place or slowly turns around. The external wrench is estimated with the frequency 25 Hz. The parameters of the individual trials are summarized in Table 6.2.

Table 6.2: Ground truth wrench in experimental setup.

Trial Name	Weight $\hat{F}_w[\text{N}]$	Ground Truth Acting Wrench $\hat{\tau}_{e,b} = [\hat{F}_x, \hat{F}_y, \hat{F}_z, \hat{\tau}_x, \hat{\tau}_y, \hat{\tau}_z]^T$
FF1 / IF1	7.54	} $\hat{F}_w[\cos \Phi_z, \sin \Phi_z, 0, 0.1 \sin \Phi_z, 0.1 \cos \Phi_z, 0]^T$
FF2 / IF2	12.53	
FF3 / IF3	20.19	
FT1 / IT1	1.48	} $\hat{F}_w[0, 0, 0, 0, 0, 1]^T$
FT2 / IT2	-1.48	
FT3 / IT3	2.50	
FT4 / IT4	-2.50	
FW1 / IW1	-7.54	} $\hat{F}_w[0, 0, 1, 0, 0, 0]^T$
FW2 / IW2	-12.53	
FW3 / IW3	-20.19	

Trial name is formed from Flat/Irrregular and Force/Torque/Weight indicating the terrain and scenario as FF, FT, FW, IF, IT, and IW, and the trial number.

Scenario 1

Force estimation scenario consists of the trials FF1, FF2, FF3, IF1, IF2, and IF3 in which the robot has been placed in the middle of the testbed, with either flat or irregular terrains. A suspended weight according to Table 6.2 has been attached to the robot using a cord. The robot has been given the input velocity command $\dot{\mathbf{q}}_b = [0, 0, 0, 0, 0, 0.1]^T$ to slowly turn around in the counterclockwise direction while estimating the acting wrench. During the locomotion, the mutual position of the robot and the pulley has been tracked using the motion capture system to determine the heading Φ_z under which $\hat{\tau}_{e,b}$ acts. The ground truth wrench thus depends on the heading Φ_z as described in Table 6.2. Note that the experimental setup induces both forces and torques due to the vertical offset 0.1 m of the cord attachment point w.r.t. the robot CoM.

Figure 6.4 and Figure 6.5 show the plots of forces and torques given the heading of the robot w.r.t. the direction Φ_z of the acting weight \hat{F}_w for the flat and irregular terrains. The estimated forces and torques are plotted with the general sine function fitted to the raw, unfiltered data using the least squares method. The

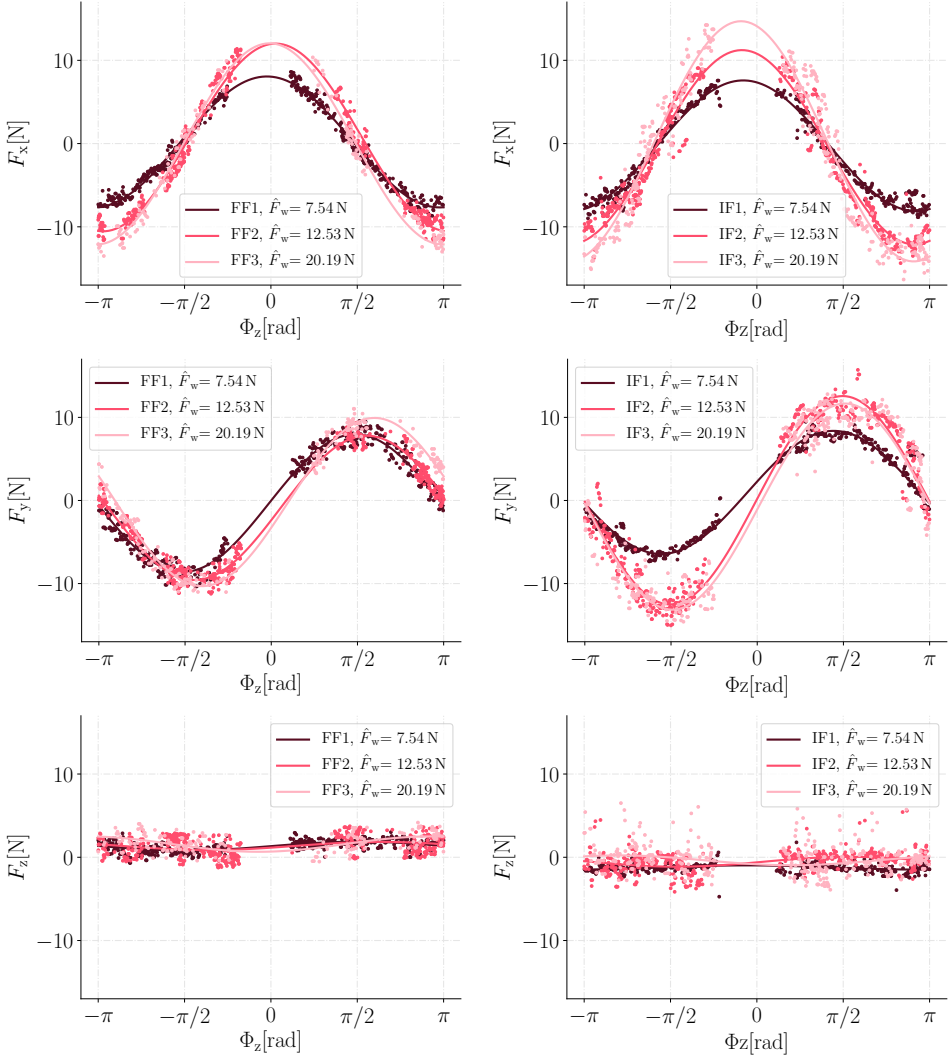


Figure 6.4: Estimated force values of the external wrench in Scenario 1 trials for the flat (left) and irregular (right) terrains. The plotted values are raw estimations fitted with the general sine function.

results match the expected behavior of the individual wrench components given the ground truth wrench $\hat{\tau}_{e,b}$ listed in Table 6.2. The results correctly show the dependence of the individual wrench components on the direction Φ_z of the acting wrench, together with the correct estimation of the magnitudes for the trials FF1, FF2, IF1, and IF2 with lighter weights.

The results show increased acting force for the heaviest weight (FF3 and IF3 trials) compared to the two lighter weights. However, the magnitude of the estimated

6. MODEL-BASED EXTERNAL WRENCH ESTIMATION

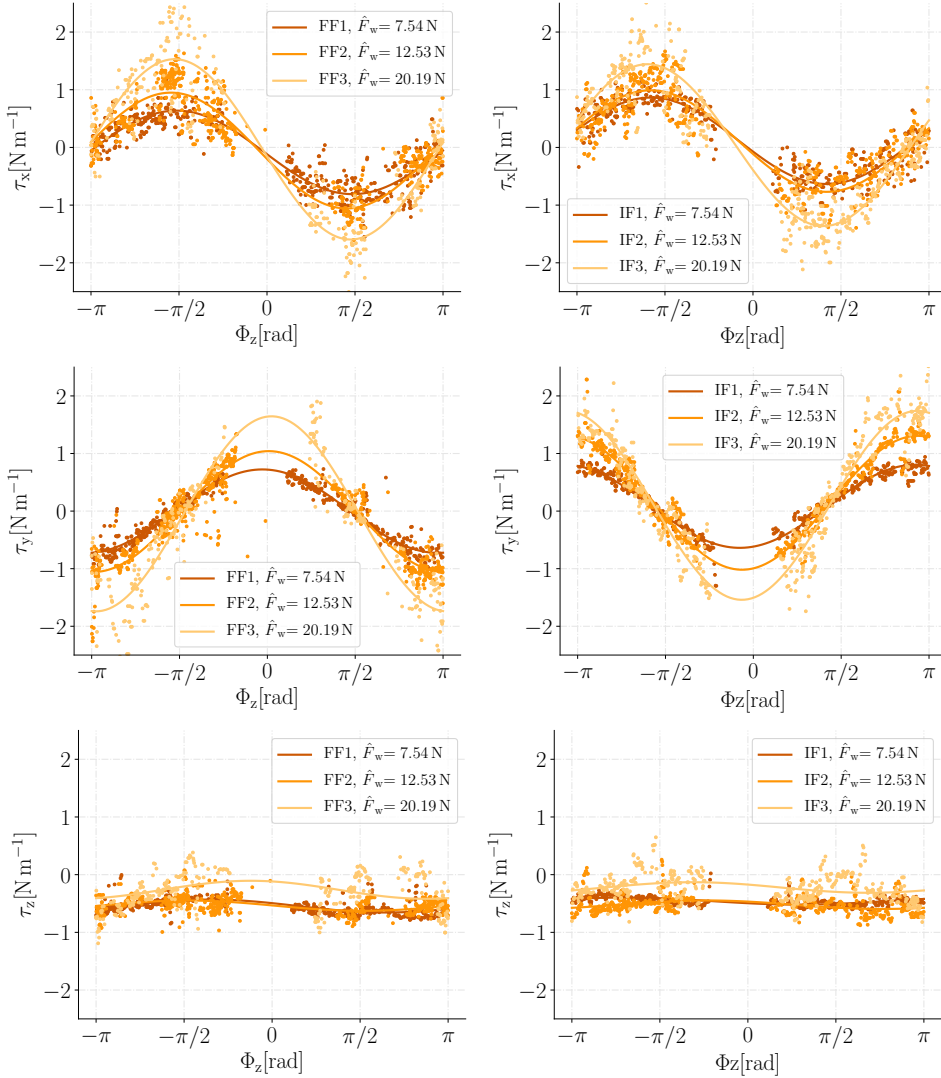


Figure 6.5: Estimated torque values of the external wrench in Scenario 1 trials for the flat (left) and irregular (right) terrains. The plotted values are raw estimations fitted with the general sine function.

forces and torques are incorrect, caused by the violation of the static footholds assumption. The robot feet start to slip because of the increased acting weight, and the whole robot moves inadvertently in the direction of the acting weight, negatively influencing the joint sensor readings and thus affecting the absolute value of the wrench estimate.

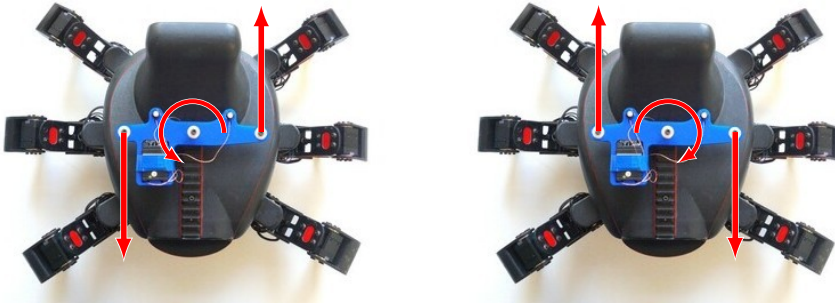


Figure 6.6: Experimental setup of the cord attachments for the torque τ_z examination in Scenario 2 with the induced positive torque (left) and negative torque (right).

Scenario 2

In the torque estimation scenario, we focus on the examination of the torque estimation τ_z in each of the FT1, FT2, FT3, FT4, IT1, IT2, IT3, and IT4 trials, where the robot has been placed in the middle of the testbed, with either flat or irregular terrains. Inducing the acting torque $\hat{\tau}_z$ is achieved by suspending the attached weight simultaneously on the opposite sides of the testbed. The swap in the direction of the torque has been achieved by swapping the attachment points of the weights on the robot handle, as it is shown in Figure 6.6. The robot has been tasked to locomote in place with the zero velocity command to maintain the direction of the acting force inducing the desired torque on the robot. The estimated acting wrench has been measured for the duration of 10s, and its mean values, together with the standard deviations, are listed in Table 6.3 with highlighted values of τ_z wrench component as the experiment targets evaluation of its estimation performance.

The results indicate a general trend in the increased absolute value of the estimated torque with the major influence on τ_z for the increased weight of the suspended weights. Relatively high differences from the acting $\hat{\tau}_z$ are noticeable for the heavier weights and the irregular terrain, where the legs experience forced side contacts with the terrain affecting the estimation precision. The issue with the sliding footholds has been noticed during the experiment, specifically for the heavier weights, which is the subject of further investigation. Nevertheless, the trend corresponds to the expected behavior and therefore, we consider the results supporting the proposed external wrench approach and made assumptions.

Scenario 3

The payload weight identification evaluation is based on a similar setup as the baseline scenario. In each of the six trials FW1, FW2, FW3, IW1, IW2, and IW3,

6. MODEL-BASED EXTERNAL WRENCH ESTIMATION

Table 6.3: Scenario 2: Estimated external wrench in acting torque $\hat{\tau}_z$ experimental trials.

Trial	FT1	FT2	FT3	FT4
$\hat{\tau}_z$ [N m ⁻¹]	1.48	-1.48	2.50	-2.50
\bar{F}_x [N]	-0.52 ± 0.73	0.13 ± 0.88	-0.49 ± 0.58	0.03 ± 0.82
\bar{F}_y [N]	0.11 ± 1.27	0.13 ± 1.08	0.31 ± 1.21	0.16 ± 1.03
\bar{F}_z [N]	-0.19 ± 0.25	-0.15 ± 0.21	-0.20 ± 0.26	-0.14 ± 0.19
$\bar{\tau}_x$ [N m ⁻¹]	0.00 ± 0.82	-0.15 ± 0.83	-0.00 ± 0.76	-0.05 ± 0.87
$\bar{\tau}_y$ [N m ⁻¹]	-0.26 ± 0.35	-0.03 ± 0.26	-0.32 ± 0.37	-0.06 ± 0.23
$\bar{\tau}_z$ [N m ⁻¹]	1.51 ± 0.34	-0.81 ± 0.34	1.85 ± 0.36	-1.19 ± 0.26

Trial	IT1	IT2	IT3	IT4
$\hat{\tau}_z$ [N m ⁻¹]	1.48	-1.48	2.50	-2.50
\bar{F}_x [N]	0.18 ± 0.99	0.07 ± 0.55	0.66 ± 0.98	-0.03 ± 3.55
\bar{F}_y [N]	-1.45 ± 2.93	0.25 ± 3.08	2.19 ± 2.33	-0.81 ± 1.09
\bar{F}_z [N]	0.23 ± 0.30	0.20 ± 0.26	0.04 ± 0.25	0.30 ± 0.76
$\bar{\tau}_x$ [N m ⁻¹]	-0.07 ± 1.72	0.23 ± 1.45	0.77 ± 1.10	-0.34 ± 1.04
$\bar{\tau}_y$ [N m ⁻¹]	0.10 ± 0.38	-0.29 ± 0.36	-0.02 ± 0.44	-0.65 ± 2.11
$\bar{\tau}_z$ [N m ⁻¹]	2.97 ± 0.72	-2.14 ± 0.53	3.18 ± 0.63	-2.79 ± 1.73

the robot has been tasked to locomote in place with the zero velocity command. A weight according to Table 6.2 has been placed directly on the back of the robot, inducing primarily the vertical acting force \hat{F}_z . The estimated external wrench has been measured for the duration of 10s, and the resulting mean values, together with the standard deviations, are reported in Table 6.4, where the values of \bar{F}_z are highlighted as they directly correspond to the payload weight.

The results match the expected behavior with the prevalent wrench component estimated to be the vertical acting force F_z . A higher variance in the force component of the resulting data in irregular terrain experiments is most likely due to the changes in the robot attitude during the locomotion.

With the known position of the payload on the back of the robot, we can use the proposed external wrench estimation method for payload weight estimation directly from the estimated value \bar{F}_z . The determined payload weights as the mean values with standard deviations from the collected data for flat terrain and gravitational acceleration 9.81 m s⁻² are listed in Table 6.5. Although the results do not perfectly match with the weight of the payload, the method is capable of providing a rough estimate of the payload weight.

Table 6.4: Scenario 3: Estimated wrench in payload weight identification experimental trials.

Trial	FW1	FW2	FW3
\hat{F}_z [N]	-7.54	-12.53	-20.19
\bar{F}_x [N]	-0.29 ± 0.28	-0.81 ± 0.44	-0.44 ± 0.67
\bar{F}_y [N]	-0.45 ± 0.26	-0.28 ± 0.24	-0.34 ± 0.44
\bar{F}_z [N]	-7.71 ± 0.40	-11.53 ± 0.34	-17.96 ± 0.63
$\bar{\tau}_x$ [N m ⁻¹]	0.30 ± 0.10	0.31 ± 0.15	0.09 ± 0.17
$\bar{\tau}_y$ [N m ⁻¹]	-0.33 ± 0.03	-0.45 ± 0.05	-0.63 ± 0.10
$\bar{\tau}_z$ [N m ⁻¹]	-0.52 ± 0.03	-0.54 ± 0.03	-0.67 ± 0.02
Trial	IW1	IW2	IW3
\hat{F}_z [N]	-7.54	-12.53	-20.19
\bar{F}_x [N]	-2.43 ± 1.93	-3.56 ± 2.67	-1.90 ± 2.04
\bar{F}_y [N]	0.14 ± 1.46	-0.19 ± 1.90	0.70 ± 1.86
\bar{F}_z [N]	-7.13 ± 0.60	-11.76 ± 4.86	-21.53 ± 6.21
$\bar{\tau}_x$ [N m ⁻¹]	0.23 ± 0.38	-0.30 ± 0.62	0.58 ± 0.54
$\bar{\tau}_y$ [N m ⁻¹]	-0.43 ± 0.12	-0.54 ± 0.34	-1.12 ± 0.23
$\bar{\tau}_z$ [N m ⁻¹]	-0.43 ± 0.10	-0.63 ± 0.13	-0.70 ± 0.15

Table 6.5: Estimated payload weight experimental results.

Payload weight [kg]	0.75	1.25	2.19	3.44
Estimated weight [kg]	0.77 ± 0.04	1.15 ± 0.03	1.79 ± 0.06	3.21 ± 0.14
Payload error	2.7%	8.0%	18.3%	6.7%

6.5 External Wrench Estimation on the HEBI Lily Robot

The external wrench estimation approach has been deployed on a HEBI Lily platform shown in Figure 6.7. As the construction of the robot features spring dampers that offloads part of the torque from the femur actuators, it introduces non-linearities into the RBD model. Therefore, without model adjustment, the quantitative results of external wrench estimation are imprecise. Hence, to verify the feasibility of the approach, the wrench estimate has been used to directly control the robot by the velocity command $\dot{\mathbf{q}}_b$ to follow the induced external wrench and comply to the interaction. The performance of the robot can be seen in the accompanying video³.

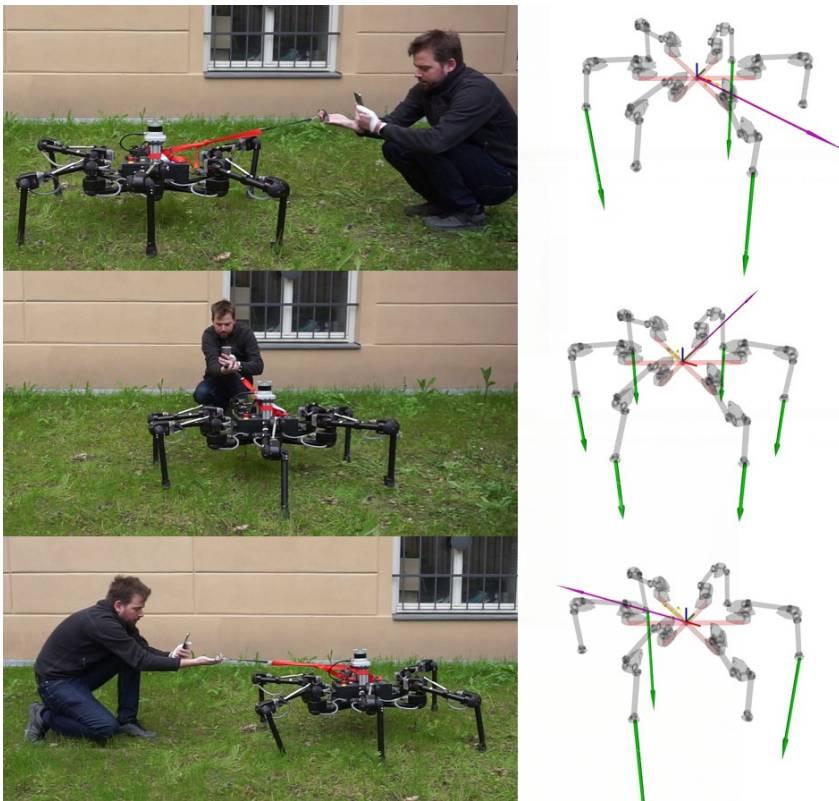


Figure 6.7: Interaction experiment with the HEBI Lily six-legged walking robot. From top to bottom, different directions of applied external wrench and its corresponding visualization. The force component and torque component of the acting wrench are visualized using magenta and yellow color, respectively. The GRF are visualized using green color.

³<https://youtu.be/EW8LqwRBtr4>

Chapter 7

Conclusion & Future Directions

This thesis addresses the topics of locomotion control and explicit interaction handling of multi-legged walking robots utilizing only proprioceptive sensing. We propose a model-based approach to leg-contact detection that uses only the position feedback of the joint actuators to monitor the virtual elasticity in the joints, and thus detect the instant of the leg contact with the environment. We leveraged on the idea of the groundwork [125] that uses a fixed threshold to detect the contact events only during the swing-down motion of the leg. We formulated the leg dynamic model and generalized the approach to detect leg contact events in any direction. The proposed approach has been integrated into a newly developed decoupled locomotion controller [1c] and allows the blind robot adaptive locomotion in irregular terrains using only the joint position feedback. The whole control system has been extensively tested over the years and provided the means for the follow-up research. It already includes the work on traversability assessment [13a] with the follow-up terrain-aware planning [14a], transfer learning [178], and deployment in the rough terrain of underground tunnels [15a]. The developed approach for contact event detection has been experimentally deployed, and its capabilities verified on a robotic manipulator, which further demonstrates its versatility. The proposed approach represents a minimalistic solution to the contact detection, applicable to a wide range of robotic platforms.

Further advancements were made in locomotion control by formulation of a closed-form locomotion controller for position-controlled robots that formalizes the relationship between the leg motion and body motion into a single equation. The developed controller allows for continuous commanding of the robot using the input twist in all six DoF up to the kinematic limits of the robot.

Finally, we have derived the whole-body dynamic model and utilized it in the explicit external wrench estimation [31a]. The proposed approach allows to explicitly estimate the external wrench acting on the robot while the robot is in motion, using only the joint feedback. We see a practical potential in the approach, as it enables different robot control strategies and applications including safer human-machine interaction, and collaborative manipulation.

Regarding the future work, our vision is for the robots not to avoid or oppose the environment interactions but to embrace their inevitable nature and make the interactions safer for the robot and humans to coexist with the robots. For the proposed external wrench estimation approach, the underlying assumption of non-slipping feet can be considered strong. Tightly coupled fusion with inertial

7. CONCLUSION & FUTURE DIRECTIONS

measurements is expected to improve the method's performance in cases of slipping feet or moving inertial frame while still relying only on proprioception.

However, a major shortcoming of model-based approaches is the need for accurate analytical model identification, which is demanding, and there is a low tolerance to changes of model parameters due to the adverse changes of the leg parameters. The changes can be in friction due to the joint wear, increased weight of the leg due to the mud deposits, and possible leg morphology due to damage [3a]. Incorporating dynamic model identification and machine learning-based approaches [3a] into the system is expected to improve the overall robustness of the system in the presence of dynamic parameter changes.

Appendix A

Experimental Platforms’ Parameters

This appendix lists the main characteristics and kinematic and dynamic parameters of the experimental platforms used for the verification of the derived approaches presented in this thesis. Five six-legged walking robots and a robotic manipulator have been used for evaluation. Namely, SCARAB I, SCARAB II, HAntR, HEBI Daisy, and HEBI Lily six-legged platforms and Rotrics DexArm small robotic arm.

We collect the main characteristics and kinematic and dynamic parameters of the six-legged platforms in Table A.1. We exploit the fact, that all the platforms have similar morphology, except of HAntR platform, that has one additional DoF per leg, and that each platform has all its legs similar. Therefore, we list the kinematic and dynamic parameters for a single leg of each platform in Table A.1. The reported lengths, and angles, and inertia values are obtained from Computer Assisted Design software. The weights are measured using scales with the precision of tenth of gram. Note, only the non-zero values of inertia matrices are reported in Table A.1.

Further, characteristics and parameters of the joint actuators of individual platforms are listed in Table A.2. These parameters are obtained from the actuator documentation provided by the manufacturer or experimentally identified using the real actuator.

Parameters of the small robotic manipulator Rotrics DexArm, used for the experiments evaluation of the model-based contact detection approach described in Section 5.4, are listed in Table A.3

A. EXPERIMENTAL PLATFORMS' PARAMETERS

Table A.1: Characteristics, kinematic and dynamic parameters of the experimental platforms.

Parameter	SCARAB I	SCARAB II	HAnTR	HEBI Daisy	HEBI Lily	
Characteristics						
DoF no.	18	18	24	18	18	
Actuator vendor	Dynamixel	Dynamixel	Dynamixel	HEBI	HEBI	
Actuator model	AX-12A	XM430-W350	AX-12A	X8-9 (c,t) X8-16 (f)	R8-9 (c,t) R8-16(f)	
Battery cap.	48 W h	115 W h	62 W h	200 W h	400 W h	
Kinematic parameters						
$a_{l,c}$	[mm]	52.0	16.0	0.0	0.0	0.0
$a_{l,f}$	[mm]	66.0	93.0	25.4	325.0	325.0
$a_{l,t}$	[mm]	130.0	122.0	81.6	325.0	325.0
$a_{l,tr}$	[mm]	–	–	205.5	–	–
$\alpha_{l,c}$	[rad]	$\pi/2$	$\pi/2$	$\pi/2$	$\pi/2$	$\pi/2$
$\alpha_{l,f}$	[rad]	0.0	0.0	$-\pi/2$	0.0	0.0
$\alpha_{l,t}$	[rad]	0.0	0.0	0.0	0.0	0.0
$\alpha_{l,tr}$	[rad]	–	–	0.0	–	–
$d_{l,c}$	[mm]	0.0	0.0	0.0	0.0	0.0
$d_{l,f}$	[mm]	0.0	0.0	-18.5	0.0	0.0
$d_{l,t}$	[mm]	0.0	0.0	0.0	0.0	0.0
$d_{l,tr}$	[mm]	–	–	0.0	–	–
$a_{c,l,c}$	[mm]	25.0	0.0	0.0	0.0	0.0
$a_{c,l,f}$	[mm]	20.0	62.0	0.0	206.0	218.0
$a_{c,l,t}$	[mm]	50.0	42.0	59.0	147.0	147.0
$a_{c,l,tr}$	[mm]	–	–	96.0	–	–
$p_{1,x}$	[mm]	120.0	120.0	88.0	205.0	313.0
$p_{1,y}$	[mm]	-60.0	-100.0	-51.0	-118.0	-181.0
β_1	[rad]	$\pi/4$	$3\pi/8$	$\pi/6$	$\pi/6$	$\pi/6$
$p_{2,x}$	[mm]	0.0	0.0	0.0	0.0	0.0
$p_{2,y}$	[mm]	-100.0	-120.0	-102.0	-187.5	-262.5
β_2	[rad]	$\pi/2$	$\pi/2$	$\pi/2$	$\pi/2$	$\pi/2$
$p_{3,x}$	[mm]	-120.0	-120.0	-88.0	-205.0	-313.0
$p_{3,y}$	[mm]	-60.0	-100.0	-51.0	-118.0	-181.0
β_3	[rad]	$3\pi/4$	$5\pi/8$	$5\pi/6$	$5\pi/6$	$5\pi/6$
$p_{4,x}$	[mm]	120.0	120.0	88.0	205.0	313.0
$p_{4,y}$	[mm]	60.0	100.0	51.0	118.0	181.0
β_4	[rad]	$-\pi/4$	$-3\pi/8$	$-\pi/6$	$-\pi/6$	$-\pi/6$
$p_{5,x}$	[mm]	0.0	0.0	0.0	0.0	0.0
$p_{5,y}$	[mm]	100.0	120.0	102.0	187.5	262.5
β_5	[rad]	$-\pi/2$	$-\pi/2$	$-\pi/2$	$-\pi/2$	$-\pi/2$
$p_{6,x}$	[mm]	-120.0	-120.0	-88.0	-205.0	-313.0
$p_{6,y}$	[mm]	60.0	100.0	51.0	118.0	181.0
β_6	[rad]	$-3\pi/4$	$-5\pi/8$	$-5\pi/6$	$-5\pi/6$	$-5\pi/6$

Continued on next page.

Table A.1: Characteristics, kinematic and dynamic parameters of the experimental platforms – (Continued).

Parameter	SCARAB I	SCARAB II	HAntR	HEBI Daisy	HEBI Lily
Dynamic parameters					
m_b [g]	1200	2132	1020	9626	14810
${}^B I_{b,1,1}$ [g mm ²]	–	10.67×10^6	–	80.22×10^6	209.83×10^6
${}^B I_{b,2,2}$ [g mm ²]	–	7.55×10^6	–	136.36×10^6	456.64×10^6
${}^B I_{b,3,3}$ [g mm ²]	–	17.34×10^6	–	200.54×10^6	641.77×10^6
$m_{l,c}$ [g]	62	90	12	540	820
$m_{l,f}$ [g]	71	202	175	1109	1315
$m_{l,t}$ [g]	100	136	86	580	580
$m_{l,tr}$ [g]	–	–	43	–	–
${}^C I_{l,c,3,3}$ [g mm ²]	1.39×10^4	3.63×10^3	1.44×10^4	1.80×10^6	2.73×10^6
${}^F I_{l,f,2,2}$ [g mm ²]	2.57×10^4	1.45×10^5	9.41×10^3	9.76×10^6	11.57×10^6
${}^F I_{l,f,3,3}$ [g mm ²]	2.57×10^4	1.45×10^5	9.41×10^3	9.76×10^6	11.57×10^6
${}^T I_{l,t,2,2}$ [g mm ²]	1.41×10^5	1.69×10^5	4.77×10^4	5.11×10^6	5.11×10^6
${}^T I_{l,t,3,3}$ [g mm ²]	1.41×10^5	1.69×10^5	4.77×10^4	5.11×10^6	5.11×10^6
${}^{TR} I_{l,tr,2,2}$ [g mm ²]	–	–	1.51×10^5	–	–
${}^{TR} I_{l,tr,3,3}$ [g mm ²]	–	–	1.51×10^5	–	–

Table A.2: Parameters of used actuators.

Parameter	Dynamixel		HEBI			
	AX-12A	XM430-W350	X8-9	X8-16	R8-9	R8-16
Actuator type	LRG	LRG	SEA	SEA	SEA	SEA
Mass [g]	54.6	82.0	479.0	490.0	685.0	715.0
Nominal input voltage [V]	12.6	16.0	42.0	42.0	42.0	42.0
Motion limits	0° – 300°	0° – 360°	4-turn continuous	4-turn continuous	4-turn continuous	4-turn continuous
Encoder resolution n_{enc}	1024	4096	65536	65536	65536	65536
Gearbox ratio Γ	1/254	1/353.5	1/762.2	1/1462.2	1/762.2	1/1462.2
Rotor inertia I_M [kg m ²]	$1.03 \cdot 10^{-7}$	$1.55 \cdot 10^{-7}$	–	–	–	–
Rotor damping B_M [N m s]	$3.12 \cdot 10^{-6}$	$3.78 \cdot 10^{-6}$	–	–	–	–
Back EMF K_M [N m A ⁻¹]	$3.91 \cdot 10^{-3}$	$4.12 \cdot 10^{-3}$	–	–	–	–
Resistance R_M [Ω]	6.5	5.9	5.3	5.3	5.3	5.3
Friction F_M [Nm]	$2.37 \cdot 10^{-4}$	$5.60 \cdot 10^{-4}$	–	–	–	–

Table A.3: Parameters of the small robotic manipulator Rotrics DexArm.

Parameter	Value	Parameter	Value
$a_{l,c}$	[mm] 0.0	$m_{l,c}$	[g] 720
$a_{l,f}$	[mm] 150.0	$m_{l,f}$	[g] 136
$a_{l,t}$	[mm] 150.0	$m_{l,t}$	[g] 190
$\alpha_{l,c}$	[rad] $\pi/2$	$C_l I_{l,c,3,3}$	[g mm ²] 8.64×10^5
$\alpha_{l,f}$	[rad] 0.0	$F_l I_{l,f,2,2}$	[g mm ²] 2.55×10^5
$\alpha_{l,t}$	[rad] 0.0	$F_l I_{l,f,3,3}$	[g mm ²] 2.55×10^5
$d_{l,c}$	[mm] 0.0	$T_l I_{l,t,2,2}$	[g mm ²] 3.56×10^5
$d_{l,f}$	[mm] 0.0	$T_l I_{l,t,3,3}$	[g mm ²] 3.56×10^5
$d_{l,t}$	[mm] 0.0	$\tau_{\text{step,M}}$	[N m ⁻¹] 0.48
$a_{c,l,c}$	[mm] 0.0	N_{poles}	[-] 200
$a_{c,l,f}$	[mm] 75.0	$N_{\mu\text{step}}$	[-] 64
$a_{c,l,t}$	[mm] 75.0		

List of Figures

1.1	Examples of environment interactions	2
1.2	Verification multi-legged platforms	3
2.1	Visualization of the support polygon	8
2.2	Examples of different 3-DoF leg morphologies	10
2.3	Showcase of multi-legged robotic platforms	16
2.4	Deployments of SCARAB I robot	17
2.5	Deployments of HAntR robot	18
2.6	Multi-legged robot locomotion control concepts	21
2.7	Overview of locomotion-control architecture	22
2.8	Example of bio-inspired locomotion control	25
3.1	Schema of the multi-legged robot leg with parameters	32
3.2	Multi-legged robot schema with parameters	33
4.1	Leg IDs assignment to individual legs	48
4.2	Overview of the operation of the proposed decoupled locomotion controller	51
4.3	The foot-tip trajectory	52
4.4	Slope adaptation in decoupled controller	54
4.5	Closed-form locomotion controller robot motion example	58
4.6	Body speed profiles	61
4.7	HAntR Slope adaptation evaluation	63
4.8	Terrain mockups used for locomotion controllers benchmarking	64
5.1	Relation between the output torque and joint angular error of P-type position-controlled actuator	68

A. LIST OF FIGURES

5.2	Position feedback-based contact detection operation	69
5.3	Integration of the model-based contact detection into the motion controller	70
5.4	Effect of motion speed on the joint angular error	71
5.5	Effect of control period on the angular error	72
5.6	Effect of latency on the joint angular error	73
5.7	Anyangle contact detection experimental setup	74
5.8	Anyangle contact detection experiment	76
5.9	Evaluation of robot stability in contact detection scenario	78
5.10	Affordable robotic manipulator used for deployment of model-based contact detection approach	79
5.11	Repeatability of manipulator motions.	80
5.12	Contact detection with the small robotic manipulator.	81
6.1	Experimental testbed for acting wrench estimation	85
6.2	The set of weights used in the experimental evaluation	86
6.3	Baseline values of estimated wrench	87
6.4	Estimated force values of the external wrench	89
6.5	Estimated torque values of the external wrench	90
6.6	Experimental setup for the acting torque estimation experiment	91
6.7	Experimental deployment of external wrench estimation on the HEBI Lily robot	95

List of Tables

2.1	Main characteristics of the selected multi-legged platforms	14
4.1	Locomotion control approaches parameterisation	59
4.2	Slope adaptation evaluation results	62
4.3	Locomotion control evaluation results	65
5.1	Anyangle contact detection evaluation scenarios description and results	75
6.1	Baseline values of the estimated wrench $\tau_{e,b}$	86
6.2	Ground truth wrench in experimental setup	88
6.3	Estimated wrench in acting torque experiments	92
6.4	Estimated wrench in payload weight identification	93
6.5	Payload weight estimation	93
A.1	Characteristics, kinematic and dynamic parameters of the experi- mental platforms	100
A.2	Parameters of used actuators	101
A.3	Parameters of the small robotic manipulator Rotrics DexArm	102

References

References to the author's work are listed first, followed by other references cited within this work. The authored references contain contribution and the number of citations based on Web of Science (WoS), Scopus, and Google Scholar (GS) with non-zero entries. The author has reached h-index 9 WoS. The citation counts were gathered on March 1st, 2023.

Author's Core Publications

- [1c] P. Čížek, M. Zoula, and J. Faigl, "Design, construction, and rough-terrain locomotion control of novel hexapod walking robot with four degrees of freedom per leg," *IEEE Access*, vol. 9, pp. 17 866–17 881, 2021. DOI: [10.1109/ACCESS.2021.3053492.](https://doi.org/10.1109/ACCESS.2021.3053492), **34% contribution, IF: 3.47, citations WoS: 4, Scopus: 6, GS: 10**
- [2c] J. Faigl and P. Čížek, "Adaptive locomotion control of hexapod walking robot for traversing rough terrains with position feedback only," *Robotics and Autonomous Systems*, vol. 116, pp. 136–147, 2019. DOI: [10.1016/j.robot.2019.03.008.](https://doi.org/10.1016/j.robot.2019.03.008), **50% contribution, IF: 3.70, citations WoS: 37, Scopus 46, GS: 72**

Author's Thesis-related Publications

- [3a] J. Kubík, P. Čížek, R. Szadkowski, and J. Faigl, "Experimental leg inverse dynamics learning of multi-legged walking robot," in *2020 Modelling and Simulation for Autonomous Systems (MESAS)*, 2021, pp. 154–168. DOI: [10.1007/978-3-030-70740-8_10.](https://doi.org/10.1007/978-3-030-70740-8_10), **25% contribution, citations Scopus: 1, GS: 1**
- [4a] M. Forouhar, P. Čížek, and J. Faigl, "SCARAB II: A small versatile six-legged walking robot," in *5th Full-Day Workshop on Legged Robots at IEEE International Conference on Robotics and Automation (ICRA)*, 2021, pp. 1–2., **33% contribution**
- [5a] P. Čížek and J. Faigl, "On locomotion control using position feedback only in traversing rough terrains with hexapod crawling robot," in *IOP Conference Series: Materials Science and Engineering*, vol. 428, 2018, p. 012 065. DOI: [10.1088/1757-899x/428/1/012065.](https://doi.org/10.1088/1757-899x/428/1/012065), **50% contribution, citations WoS: 5, Scopus: 8, GS: 7**

- [6a] **P.Čížek**, J. Kubík, and J. Faigl, “Online foot-strike detection using inertial measurements for multi-legged walking robot,” in *IEEE/RSJ International Conference on Intelligent Robots and Systems (IROS)*, 2018, pp. 7622–7627. DOI: [10.1109/IROS.2018.8594010.](https://doi.org/10.1109/IROS.2018.8594010), **33% contribution, citations WoS: 2, Scopus: 2, GS: 4**
- [7a] **P. Čížek**, J. Faigl, and D. Masri, “Foothold placement planning with a hexapod crawling robot,” in *IEEE/RSJ International Conference on Intelligent Robots and Systems (IROS)*, 2017, pp. 4096–4101. DOI: [10.1109/IROS.2017.8206267.](https://doi.org/10.1109/IROS.2017.8206267), **40% contribution, citations WoS: 13, Scopus: 15, GS: 17**
- [8a] R. J. Szadkowski, **P.Čížek**, and J. Faigl, “Learning central pattern generator network with back-propagation algorithm,” in *Conference Information Technologies - Applications and Theory (ITAT)*, 2018, pp. 116–123., **33% contribution, citations Scopus: 2, GS: 4**
- [9a] M. T. Nguyenová, **P.Čížek**, and J. Faigl, “Modeling proprioceptive sensing for locomotion control of hexapod crawling robot in robotic simulator,” in *2018 Modelling and Simulation for Autonomous Systems (MESAS)*, 2019, pp. 215–225. DOI: [10.1007/978-3-030-14984-0_17.](https://doi.org/10.1007/978-3-030-14984-0_17), **33% contribution, citations WoS: 2, Scopus: 2, GS: 4**

■ Author’s Thesis-unrelated Publications

- [10a] T. Rouček, M. Pecka, **P. Čížek**, *et al.*, “Darpa subterranean challenge: Multi-robotic exploration of underground environments,” in *2019 Modelling and Simulation for Autonomous Systems (MESAS)*, 2020, pp. 274–290. DOI: [10.1007/978-3-030-43890-6_22.](https://doi.org/10.1007/978-3-030-43890-6_22), **5% contribution, citations WoS: 21, Scopus 27, GS: 72**
- [11a] P. Milička, **P. Čížek**, and J. Faigl, “On chaotic oscillator-based central pattern generator for motion control of hexapod walking robot,” in *Conference Information Technologies - Applications and Theory (ITAT)*, 2016, pp. 131–137., **33% contribution, citations Scopus: 8, GS: 7**
- [12a] **P.Čížek** and J. Faigl, “Self-supervised learning of the biologically-inspired obstacle avoidance of hexapod walking robot,” *Bioinspiration & Biomimetics*, vol. 14, no. 4, p. 046002, 2019. DOI: [10.1088/1748-3190/ab1a9c.](https://doi.org/10.1088/1748-3190/ab1a9c), **50% contribution, IF: 2.98, citations WoS: 3, Scopus: 4, GS: 8**
- [13a] M. Prágr, **P.Čížek**, and J. Faigl, “Cost of transport estimation for legged robot based on terrain features inference from aerial scan,” in *IEEE/RSJ International Conference on Intelligent Robots and Systems (IROS)*, 2018, pp. 1745–1750. DOI: [10.1109/IROS.2018.8593374.](https://doi.org/10.1109/IROS.2018.8593374), **33% contribution, citations WoS: 15, Scopus: 19, GS: 22**

A. REFERENCES

- [14a] M. Prágr, **P. Čížek**, J. Bayer, and J. Faigl, “Online incremental learning of the terrain traversal cost in autonomous exploration,” in *Robotics: Science and Systems (RSS)*, 2019. DOI: [10.15607/RSS.2019.XV.040.](https://doi.org/10.15607/RSS.2019.XV.040), **25% contribution, citations WoS: 10, Scopus: 14, GS: 22**
- [15a] T. Rouček, M. Pecka, **P. Čížek**, *et al.*, “System for multi-robotic exploration of underground environments CTU-CRAS-NORLAB in the DARPA subterranean challenge,” *Field Robotics*, vol. 2, pp. 1779–1818, 2022. DOI: [10.55417/fr.2022055.](https://doi.org/10.55417/fr.2022055), **3% contribution, citations GS: 20**
- [16a] J. Bayer, **P. Čížek**, and J. Faigl, “Autonomous multi-robot exploration with ground vehicles in DARPA subterranean challenge finals,” *Field Robotics*, vol. 3, pp. 266–300, 2023., **33% contribution**
- [17a] M. Prágr, **P. Čížek**, and J. Faigl, “Traversal cost modeling based on motion characterization for multi-legged walking robots,” in *European Conference on Mobile Robots (ECMR)*, 2019, pp. 1–6. DOI: [10.1109/ECMR.2019.8870912.](https://doi.org/10.1109/ECMR.2019.8870912), **33% contribution**
- [18a] M. Prágr, **P. Čížek**, and J. Faigl, “Incremental learning of traversability cost for aerial reconnaissance support to ground units,” in *2018 Modelling and Simulation for Autonomous Systems (MESAS)*, 2019, pp. 412–421. DOI: [10.1007/978-3-030-14984-0_30.](https://doi.org/10.1007/978-3-030-14984-0_30), **33% contribution, citations WoS 8, Scopus: 7, GS: 9**
- [19a] **P. Čížek** and J. Faigl, “Real-time FPGA-based detection of Speeded-Up Robust Features using separable convolution,” *IEEE Transactions on Industrial Informatics*, vol. 14, no. 3, pp. 1155–1163, 2018. DOI: [10.1109/TII.2017.2764485.](https://doi.org/10.1109/TII.2017.2764485), **60% contribution, IF: 11.64, citations WoS 10, Scopus 12, GS: 14**
- [20a] **P. Čížek** and J. Faigl, “RNN-based visual obstacle avoidance with a CPG controlled hexapod walking robot,” in *IEEE/RSJ International Conference on Intelligent Robots and Systems (IROS)*, 2017, p. 3146., **50% contribution**
- [21a] **P. Čížek**, P. Milička, and J. Faigl, “Neural based obstacle avoidance with CPG controlled hexapod walking robot,” in *International Joint Conference on Neural Networks (IJCNN)*, 2017, pp. 650–656. DOI: [10.1109/IJCNN.2017.7965914.](https://doi.org/10.1109/IJCNN.2017.7965914), **60% contribution, citations WoS: 10, Scopus: 14, GS: 12**
- [22a] **P. Čížek**, J. Faigl, and J. Bayer, “Enhancing neural based obstacle avoidance with CPG controlled hexapod walking robot,” in *Conference Information Technologies - Applications and Theory (ITAT)*, 2017, pp. 65–70., **40% contribution, citations Scopus: 1**
- [23a] M. Nowicki, D. Belter, A. Kostusiak, **P. Čížek**, J. Faigl, and P. Skrzypczyński, “An experimental study on feature-based SLAM for multi-legged robots with RGB-D sensors,” *Industrial Robot*, vol. 44, no. 4, pp. 428–441, 2017. DOI: [10.1108/IR-11-2016-0340.](https://doi.org/10.1108/IR-11-2016-0340), **16% contribution, citations WoS: 12, Scopus: 15, GS: 20**

- [24a] P. Čížek, J. Faigl, and D. Masri, “Low-latency image processing for vision-based navigation systems,” in *IEEE International Conference on Robotics and Automation (ICRA)*, 2016, pp. 781–786. DOI: [10.1109/ICRA.2016.7487207](https://doi.org/10.1109/ICRA.2016.7487207)., **33% contribution, citations WoS: 3, Scopus: 6, GS: 11**
- [25a] T. Fischer, T. Pire, P. Čížek, P. D. Cristóforis, and J. Faigl, “Stereo vision-based localization for hexapod walking robots operating in rough terrains,” in *IEEE/RSJ International Conference on Intelligent Robots and Systems (IROS)*, 2016, pp. 2492–2497. DOI: [10.1109/IROS.2016.7759388](https://doi.org/10.1109/IROS.2016.7759388)., **20% contribution, citations WoS: 9, Scopus: 9, GS: 18**
- [26a] P. Čížek and J. Faigl, “On localization and mapping with RGB-D sensor and hexapod walking robot in rough terrains,” in *IEEE International Conference on Systems, Man, and Cybernetics (SMC)*, 2016, pp. 2273–2278. DOI: [10.1109/SMC.2016.7844577](https://doi.org/10.1109/SMC.2016.7844577)., **50% contribution, citations WoS: 6, Scopus: 14, GS: 19**
- [27a] J. Bayer, P. Čížek, and J. Faigl, “On construction of a reliable ground truth for evaluation of visual slam algorithms,” in *Acta Polytechnica CTU Proceedings*, 2016, pp. 1–5. DOI: [10.14311/APP.2016.6.0001](https://doi.org/10.14311/APP.2016.6.0001)., **33% contribution, citations GS: 6**
- [28a] L. Černý, P. Čížek, and J. Faigl, “On evaluation of motion gaits energy efficiency with a hexapod crawling robot,” in *Acta Polytechnica CTU Proceedings*, 2016, pp. 6–10. DOI: [10.14311/APP.2016.6.0006](https://doi.org/10.14311/APP.2016.6.0006)., **33% contribution, citations GS: 4**
- [29a] P. Čížek and J. Faigl, “On FPGA based acceleration of image processing in mobile robotics,” in *Acta Polytechnica CTU Proceedings*, 2015, pp. 8–14. DOI: [10.14311/APP.2015.1.0008](https://doi.org/10.14311/APP.2015.1.0008)., **50% contribution**
- [30a] T. Krajník, J. Šváb, S. Pedre, P. Čížek, and L. Přeučil, “FPGA-based module for SURF extraction,” *Machine Vision and Applications*, vol. 25, no. 3, pp. 787–800, 2014. DOI: [10.1007/s00138-014-0599-0](https://doi.org/10.1007/s00138-014-0599-0)., **10% contribution, citations WoS: 14, Scopus: 16, GS: 19**

■ Author’s Publications in Review

- [31a] P. Čížek, M. Forouhar, J. Faigl, and J. Baltes, “External wrench estimation in adaptive locomotion of multi-legged robot,” in *submitted to IEEE Transactions on Robotics*, Jan. 2023., **25% contribution**

■ Cited references

- [32] S. Haddadin, A. De Luca, and A. Albu-Schaffer, “Robot collisions: A survey on detection, isolation, and identification,” *IEEE Transactions on Robotics*, vol. 33, no. 6, pp. 1292–1312, 2017. DOI: [10.1109/TR0.2017.2723903](https://doi.org/10.1109/TR0.2017.2723903).

A. REFERENCES

- [33] F. Tedeschi and G. Carbone, “Design issues for hexapod walking robots,” *Robotics*, vol. 3, pp. 181–206, 2014. DOI: [10.3390/robotics3020181](https://doi.org/10.3390/robotics3020181).
- [34] A. Mahapatra, S. S. Roy, and D. K. Pratihar, *Multi-legged robots – A review*. Springer, Singapore, 2020, pp. 11–32. DOI: [10.1007/978-981-15-2953-5](https://doi.org/10.1007/978-981-15-2953-5).
- [35] A. Roennau, G. Heppner, L. Pfotzer, and R. Dillmann, “LAURON V: Optimized leg configuration for the design of a bio-inspired walking robot,” in *Nature-Inspired Mobile Robotics*, 2013, pp. 563–570. DOI: [10.1142/9789814525534_0071](https://doi.org/10.1142/9789814525534_0071).
- [36] M. Bjelonic, N. Kottege, T. Homberger, P. Borges, P. Beckerle, and M. Chli, “Weaver: Hexapod robot for autonomous navigation on unstructured terrain,” *Journal of Field Robotics*, vol. 35, no. 7, pp. 1063–1079, 2018. DOI: [10.1002/rob.21795](https://doi.org/10.1002/rob.21795).
- [37] A. Roennau, G. Heppner, M. Nowicki, and R. Dillmann, “LAURON V: A versatile six-legged walking robot with advanced maneuverability,” in *IEEE/ASME International Conference on Advanced Intelligent Mechatronics*, 2014, pp. 82–87. DOI: [10.1109/AIM.2014.6878051](https://doi.org/10.1109/AIM.2014.6878051).
- [38] U. Saranlı, M. Buehler, and D. E. Koditschek, “RHex: A simple and highly mobile hexapod robot,” *International Journal of Robotics Research*, vol. 20, no. 7, pp. 616–631, 2001. DOI: [10.1177/02783640122067570](https://doi.org/10.1177/02783640122067570).
- [39] K. Galloway, G. Clark Haynes, D. Ilhan, *et al.*, “X-RHex: A highly mobile hexapedal robot for sensorimotor tasks,” University of Pennsylvania, Tech. Rep., 2010, Technical Reports (ESE).
- [40] G. Bledt, M. J. Powell, B. Katz, J. Di Carlo, P. M. Wensing, and S. Kim, “MIT Cheetah 3: Design and control of a robust, dynamic quadruped robot,” in *IEEE/RSJ International Conference on Intelligent Robots and Systems (IROS)*, 2018, pp. 2245–2252. DOI: [10.1109/IROS.2018.8593885](https://doi.org/10.1109/IROS.2018.8593885).
- [41] Boston Dynamics, (*@Online*), <https://www.bostondynamics.com/spot>, cited on 2022-12-14, 2022.
- [42] M. Hutter, C. Gehring, D. Jud, *et al.*, “ANYmal - a highly mobile and dynamic quadrupedal robot,” in *IEEE/RSJ International Conference on Intelligent Robots and Systems (IROS)*, 2016, pp. 38–44. DOI: [10.1109/IROS.2016.7758092](https://doi.org/10.1109/IROS.2016.7758092).
- [43] S. Fahmi, C. Mastalli, M. Focchi, and C. Semini, “Passive whole-body control for quadruped robots: Experimental validation over challenging terrain,” *IEEE Robotics and Automation Letters*, vol. 4, no. 3, pp. 2553–2560, 2019. DOI: [10.1109/LRA.2019.2908502](https://doi.org/10.1109/LRA.2019.2908502).
- [44] T. Bandyopadhyay, R. Steindl, F. Talbot, *et al.*, “Magneto: A versatile multi-limbed inspection robot,” in *IEEE/RSJ International Conference on Intelligent Robots and Systems (IROS)*, 2018, pp. 2253–2260. DOI: [10.1109/IROS.2018.8593891](https://doi.org/10.1109/IROS.2018.8593891).

- [45] E. Krotkov, R. Simmons, and W. L. Whittaker, “Ambler: Performance of a six-legged planetary rover,” *Acta Astronautica*, vol. 35, no. 1, pp. 75–81, 1995.
- [46] D. Belter and K. Walas, “A compact walking robot–flexible research and development platform,” in *Recent Advances in Automation, Robotics and Measuring Techniques*, Springer, 2014, pp. 343–352. DOI: [10.1007/978-3-319-05353-0_33](https://doi.org/10.1007/978-3-319-05353-0_33).
- [47] M. Gornier, T. Wimbock, A. Baumann, *et al.*, “The DLR-Crawler: A testbed for actively compliant hexapod walking based on the fingers of DLR-Hand II,” in *IEEE/RSJ International Conference on Intelligent Robots and Systems (IROS)*, 2008, pp. 1525–1531. DOI: [10.1109/IROS.2008.4650655](https://doi.org/10.1109/IROS.2008.4650655).
- [48] W. Cheah, H. H. Khalili, F. Arvin, P. Green, S. Watson, and B. Lennox, “Advanced motions for hexapods,” *International Journal of Advanced Robotic Systems*, vol. 16, no. 2, p. 1729881419841537, 2019. DOI: [10.1177/1729881419841537](https://doi.org/10.1177/1729881419841537).
- [49] M. Pitchai, X. Xiong, M. Thor, *et al.*, “CPG driven RBF network control with reinforcement learning for gait optimization of a dung beetle-like robot,” in *International Conference on Artificial Neural Networks (ICANN)*, 2019, pp. 698–710. DOI: [10.1007/978-3-030-30487-4_53](https://doi.org/10.1007/978-3-030-30487-4_53).
- [50] M. Thor, J. C. Larsen, and P. Manoonpong, “MORF – modular robot framework,” in *Proceedings of 2nd International Youth Conference on Bionic Engineering (IYCBE)*, 2018, pp. 23–25.
- [51] S. Kalouche, D. Rollinson, and H. Choset, “Modularity for maximum mobility and manipulation: Control of a reconfigurable legged robot with series-elastic actuators,” in *IEEE International Symposium on Safety, Security, and Rescue Robotics (SSRR)*, 2015, pp. 1–8. DOI: [10.1184/R1/6555620.v1](https://doi.org/10.1184/R1/6555620.v1).
- [52] HEBI Robotics, (*@Online*), <http://www.hebirobotics.com>, cited on 2022-12-14, 2022.
- [53] T. Horvat, K. Karakasiliotis, K. Melo, L. Fleury, R. Thandiackal, and A. J. Ijspeert, “Inverse kinematics and reflex based controller for body-limb coordination of a salamander-like robot walking on uneven terrain,” in *IEEE/RSJ International Conference on Intelligent Robots and Systems (IROS)*, 2015, pp. 195–201. DOI: [10.1109/IROS.2015.7353374](https://doi.org/10.1109/IROS.2015.7353374).
- [54] T. M. Roehr, F. Cordes, and F. Kirchner, “Reconfigurable integrated multi-robot exploration system (RIMRES): Heterogeneous modular reconfigurable robots for space exploration,” *Journal of Field Robotics*, vol. 31, no. 1, pp. 3–34, 2014. DOI: [10.1002/rob.21477](https://doi.org/10.1002/rob.21477).
- [55] O. A. Silva, P. Sigel, W. Eaton, *et al.*, “CRABOT: A six-legged platform for environmental exploration and object manipulation,” in *Proceedings of the 4th Congress on Robotics and Neuroscience*, 2018, pp. 46–51. DOI: [10.21428/8e2819f3](https://doi.org/10.21428/8e2819f3).

A. REFERENCES

- [56] S. Bartsch, M. Manz, P. Kampmann, *et al.*, “Development and control of the multi-legged robot MANTIS,” in *Proceedings of 47th International Symposium on Robotics*, 2016, pp. 1–8.
- [57] K. Hauser, T. Bretl, J.-C. Latombe, and B. Wilcox, “Motion planning for a six-legged lunar robot,” in *Algorithmic Foundation of Robotics VII: Selected Contributions of the Seventh International Workshop on the Algorithmic Foundations of Robotics*. Springer-Verlag Berlin, 2008, pp. 301–316. DOI: [10.1007/978-3-540-68405-3_19](https://doi.org/10.1007/978-3-540-68405-3_19).
- [58] M. Focchi, A. Del Prete, I. Havoutis, R. Featherstone, D. G. Caldwell, and C. Semini, “High-slope terrain locomotion for torque-controlled quadruped robots,” *Autonomous Robots*, vol. 41, no. 1, pp. 259–272, 2017. DOI: [10.1007/s10514-016-9573-1](https://doi.org/10.1007/s10514-016-9573-1).
- [59] R. Käslin, H. Kolvenbach, L. Paez, K. Lika, and M. Hutter, “Towards a passive adaptive planar foot with ground orientation and contact force sensing for legged robots,” in *IEEE/RSJ International Conference on Intelligent Robots and Systems (IROS)*, 2018, pp. 2707–2714. DOI: [10.1109/IROS.2018.8593875](https://doi.org/10.1109/IROS.2018.8593875).
- [60] A. M. Abat, “Mechanical design for robot locomotion,” Ph.D. dissertation, Oregon State University, 2018.
- [61] J. Norby, J. Y. Li, C. Selby, A. Patel, and A. M. Johnson, “Enabling dynamic behaviors with aerodynamic drag in lightweight tails,” *IEEE Transactions on Robotics*, vol. 37, no. 4, pp. 1144–1153, 2021. DOI: [10.1109/TR0.2020.3045644](https://doi.org/10.1109/TR0.2020.3045644).
- [62] A. J. Ijspeert, “Central pattern generators for locomotion control in animals and robots: A review,” *Neural Networks*, vol. 21, no. 4, pp. 642–653, 2008. DOI: [10.1016/j.neunet.2008.03.014](https://doi.org/10.1016/j.neunet.2008.03.014).
- [63] B. Zhong, S. Zhang, M. Xu, Y. Zhou, T. Fang, and W. Li, “On a CPG-based hexapod robot: AmphiHex-II with variable stiffness legs,” *IEEE/ASME Transactions on Mechatronics*, vol. 23, no. 2, pp. 542–551, 2018. DOI: [10.1109/TMECH.2018.2800776](https://doi.org/10.1109/TMECH.2018.2800776).
- [64] Y. Tian and F. Gao, “Efficient motion generation for a six-legged robot walking on irregular terrain via integrated foothold selection and optimization-based whole-body planning,” *Robotica*, vol. 36, pp. 1–20, 2017. DOI: [10.1017/S0263574717000418](https://doi.org/10.1017/S0263574717000418).
- [65] G. Kenneally, A. De, and D. E. Koditschek, “Design principles for a family of direct-drive legged robots,” *IEEE Robotics and Automation Letters*, vol. 1, no. 2, pp. 900–907, 2016. DOI: [10.1109/LRA.2016.2528294](https://doi.org/10.1109/LRA.2016.2528294).
- [66] S. S. Roy and D. K. Pratihar, “Effects of turning gait parameters on energy consumption and stability of a six-legged walking robot,” *Robotics and Autonomous Systems*, vol. 60, no. 1, pp. 72–82, 2012. DOI: [10.1016/j.robot.2011.08.013](https://doi.org/10.1016/j.robot.2011.08.013).

- [67] B. Tam, F. Talbot, R. Steindl, A. Elfes, and N. Kottege, “OpenSHC: A versatile multilegged robot controller,” *IEEE Access*, vol. 8, pp. 188 908–188 926, 2020. DOI: [10.1109/ACCESS.2020.3031019](https://doi.org/10.1109/ACCESS.2020.3031019).
- [68] H. Zhuang, H. Gao, L. Ding, Z. Liu, and Z. Deng, “Method for analyzing articulated torques of heavy-duty six-legged robot,” *Chinese Journal of Mechanical Engineering*, vol. 26, no. 4, pp. 801–812, 2013. DOI: [10.3901/cjme.2013.04.801](https://doi.org/10.3901/cjme.2013.04.801).
- [69] B. Kennedy, H. Aghazarian, Y. Cheng, *et al.*, “LEMUR: Legged excursion mechanical utility rover,” *Autonomous Robots*, vol. 11, pp. 201–205, 2001. DOI: [10.1023/A:1012474603861](https://doi.org/10.1023/A:1012474603861).
- [70] A. Mahapatra, S. S. Roy, and D. K. Pratihar, *Multi-body Inverse Dynamic Modeling and Analysis of Six-Legged Robots*. Springer, Singapore, 2020, pp. 77–135. DOI: [10.1007/978-981-15-2953-5_4](https://doi.org/10.1007/978-981-15-2953-5_4).
- [71] D. Grzelczyk, B. Stanczyk, and J. Awrejcewicz, “Kinematics, dynamics and power consumption analysis of the hexapod robot during walking with tripod gait,” *International Journal of Structural Stability and Dynamics*, vol. 17, no. 5, p. 1 740 010, 2017. DOI: [10.1142/S0219455417400107](https://doi.org/10.1142/S0219455417400107).
- [72] H. Deng, G. Xin, G. Zhong, and M. Mistry, “Gait and trajectory rolling planning and control of hexapod robots for disaster rescue applications,” *Robotics and Autonomous Systems*, vol. 95, pp. 13–24, 2017. DOI: [10.1016/j.robot.2017.05.007](https://doi.org/10.1016/j.robot.2017.05.007).
- [73] S. S. Roy and D. K. Pratihar, “Kinematics, dynamics and power consumption analyses for turning motion of a six-legged robot,” *Journal of Intelligent & Robotic Systems*, vol. 74, no. 3-4, pp. 663–688, 2014. DOI: [10.1007/s10846-013-9850-6](https://doi.org/10.1007/s10846-013-9850-6).
- [74] C. Li, A. Pullin, D. Haldane, H. K Lam, R. S Fearing, and R. J Full, “Terradynamically streamlined shapes in animals and robots enhance traversability through densely cluttered terrain,” *Bioinspiration & Biomimetics*, vol. 10, 2015. DOI: [10.1088/1748-3190/10/4/046003](https://doi.org/10.1088/1748-3190/10/4/046003).
- [75] H. Zhuang, H. Gao, Z. Deng, L. Ding, and Z. Liu, “A review of heavy-duty legged robots,” *Science China Technological Sciences*, vol. 57, no. 2, pp. 298–314, 2014. DOI: [10.1007/s11431-013-5443-7](https://doi.org/10.1007/s11431-013-5443-7).
- [76] B. H. Jun, H. Shim, B. Kim, *et al.*, “Development of seabed walking robot CR200,” in *OCEANS MTS/IEEE Bergen: The Challenges of the Northern Dimension*, 2013, pp. 1–5.
- [77] J. He and F. Gao, “Mechanism, actuation, perception, and control of highly dynamic multilegged robots: A review,” *Chinese Journal of Mechanical Engineering*, vol. 33, no. 1, 2020. DOI: [10.1186/s10033-020-00485-9](https://doi.org/10.1186/s10033-020-00485-9).
- [78] Y. Zhong, R. Wang, H. Feng, and Y. Chen, “Analysis and research of quadruped robot’s legs: A comprehensive review,” *International Journal of Advanced Robotic Systems*, vol. 16, no. 3, p. 1 729 881 419 844 148, 2019. DOI: [10.1177/1729881419844148](https://doi.org/10.1177/1729881419844148).

A. REFERENCES

- [79] G. Bledt, P. M. Wensing, S. Ingersoll, and S. Kim, “Contact model fusion for event-based locomotion in unstructured terrains,” in *IEEE International Conference on Robotics and Automation (ICRA)*, 2018, pp. 4399–4406. DOI: [10.1109/ICRA.2018.8460904](https://doi.org/10.1109/ICRA.2018.8460904).
- [80] L. Campanaro, S. Gangapurwala, W. Merkt, and I. Havoutis, “Learning and deploying robust locomotion policies with minimal dynamics randomization,” *arXiv preprint arXiv:2209.12878*, 2022.
- [81] G. A. Pratt and M. M. Williamson, “Series elastic actuators,” in *IEEE/RSJ International Conference on Intelligent Robots and Systems (IROS)*, vol. 1, 1995, pp. 399–406. DOI: [10.1109/IROS.1995.525827](https://doi.org/10.1109/IROS.1995.525827).
- [82] D. Drotman, S. Jadhav, D. Sharp, C. Chan, and M. T. Tolley, “Electronics-free pneumatic circuits for controlling soft-legged robots,” *Science Robotics*, vol. 6, no. 51, eaay2627, 2021. DOI: [10.1126/scirobotics.aay2627](https://doi.org/10.1126/scirobotics.aay2627).
- [83] M. Raibert, K. Blankespoor, G. Nelson, and R. Playter, “BigDog, the rough-terrain quadruped robot,” *IFAC Proceedings Volumes*, vol. 41, no. 2, pp. 10 822–10 825, 2008. DOI: [10.3182/20080706-5-KR-1001.01833](https://doi.org/10.3182/20080706-5-KR-1001.01833).
- [84] Boston Dynamics, (*@Online*), <https://www.bostondynamics.com/atlas>, cited on 2022-12-14, 2022.
- [85] J. O’Reilly, “Performance metrics and their application to legged robots,” Ph.D. dissertation, ETH Zürich, Dec. 2020. DOI: [10.13140/RG.2.2.25834.95686](https://doi.org/10.13140/RG.2.2.25834.95686).
- [86] N. Kottege, C. Parkinson, P. Moghadam, A. Elfes, and S. P. N. Singh, “Energetics-informed hexapod gait transitions across terrains,” in *IEEE International Conference on Robotics and Automation (ICRA)*, 2015, pp. 5140–5147. DOI: [10.1109/ICRA.2015.7139915](https://doi.org/10.1109/ICRA.2015.7139915).
- [87] A. Elfes, R. Steindl, F. Talbot, *et al.*, “The Multilegged Autonomous Explorer (MAX),” in *IEEE International Conference on Robotics and Automation (ICRA)*, 2017, pp. 1050–1057. DOI: [10.1109/ICRA.2017.7989126](https://doi.org/10.1109/ICRA.2017.7989126).
- [88] J. Coelho, F. Ribeiro, B. Dias, G. Lopes, and P. Flores, “Trends in the control of hexapod robots: A survey,” *Robotics*, vol. 10, no. 3, 2021. DOI: [10.3390/robotics10030100](https://doi.org/10.3390/robotics10030100).
- [89] M. Bjelonic, “Planning and control for hybrid locomotion of wheeled-legged robots,” Ph.D. dissertation, ETH Zürich, 2021. DOI: [10.3929/ethz-b-000515694](https://doi.org/10.3929/ethz-b-000515694).
- [90] Unitree Robotics, (*@Online*), <https://www.unitree.com/en/a1>, cited on 2022-12-14, 2022.
- [91] ANYBotics - Anymal C robot specifications, (*@Online*), https://www.anybotics.com/wp-content/uploads/2022/09/anymal_specifications_sheet.pdf, cited on 2022-12-14, 2022.

- [92] J. Bayer and J. Faigl, “On autonomous spatial exploration with small hexapod walking robot using tracking camera intel realsense t265,” in *European Conference on Mobile Robots (ECMR)*, 2019, pp. 1–6. DOI: [10.1109/ECMR.2019.8870968](https://doi.org/10.1109/ECMR.2019.8870968).
- [93] A. Winkler, “Optimization-based motion planning for legged robots,” Ph.D. dissertation, ETH Zürich, 2019. DOI: [10.3929/ethz-b-000272432](https://doi.org/10.3929/ethz-b-000272432).
- [94] N. Porcino, “Hexapod gait control by a neural network,” in *International Joint Conference on Neural Networks (IJCNN)*, 1990, pp. 189–194. DOI: [10.1109/IJCNN.1990.137567](https://doi.org/10.1109/IJCNN.1990.137567).
- [95] G. Dudek and M. Jenkin, *Computational Principles of Mobile Robotics*. New York, NY, USA: Cambridge University Press, 2000, ISBN: 0-521-56876-5.
- [96] D. Valouch and J. Faigl, “Gait-free planning for hexapod walking robot,” in *European Conference on Mobile Robots (ECMR)*, 2021, pp. 1–8. DOI: [10.1109/ECMR50962.2021.9568834](https://doi.org/10.1109/ECMR50962.2021.9568834).
- [97] S.-M. Song and Y.-D. Chen, “A free gait algorithm for quadrupedal walking machines,” *Journal of Terramechanics*, vol. 28, no. 1, pp. 33–48, 1991. DOI: [10.1016/0022-4898\(91\)90005-Q](https://doi.org/10.1016/0022-4898(91)90005-Q).
- [98] M. R. Fielding and G. R. Dunlop, “Omnidirectional hexapod walking and efficient gaits using restrictedness,” *International Journal of Robotics Research*, vol. 23, no. 10-11, pp. 1105–1110, 2004. DOI: [10.1177/0278364904047396](https://doi.org/10.1177/0278364904047396).
- [99] M. Hutter, “StarLETH & co. – design and control of legged robots with compliant actuation,” Ph.D. dissertation, ETH Zürich, 2013. DOI: [10.3929/ethz-a-009915229](https://doi.org/10.3929/ethz-a-009915229).
- [100] M. Hutter, *Keynote speech*, IEEE International Conference on Robotics and Automation (ICRA), cited on 2022-12-14, 2022., (@Online) <https://www.youtube.com/watch?v=abdLIF0zdRo>
- [101] F. C. Lynch Kevin M. and Park, *Modern robotics – mechanics, planning, and control*. Cambridge University Press, 2017.
- [102] J. C. Arevalo and E. Garcia, “Impedance control for legged robots: An insight into the concepts involved,” *IEEE Transactions on Systems, Man, and Cybernetics*, vol. 42, no. 6, pp. 1400–1411, 2012. DOI: [10.1109/TSMCC.2012.2187190](https://doi.org/10.1109/TSMCC.2012.2187190).
- [103] E. Tennakoon, T. Peynot, J. Roberts, and N. Kottege, “Probe-before-step walking strategy for multi-legged robots on terrain with risk of collapse,” in *IEEE International Conference on Robotics and Automation (ICRA)*, 2020, pp. 5530–5536. DOI: [10.1109/ICRA40945.2020.9197154](https://doi.org/10.1109/ICRA40945.2020.9197154).
- [104] J. Hwangbo, C. D. Bellicoso, P. Fankhauser, and M. Hutter, “Probabilistic foot contact estimation by fusing information from dynamics and differential/forward kinematics,” in *IEEE/RSJ International Conference on Intelligent Robots and Systems (IROS)*, 2016, pp. 3872–3878. DOI: [10.1109/IROS.2016.7759570](https://doi.org/10.1109/IROS.2016.7759570).

A. REFERENCES

- [105] M. Bloesch, C. Gehring, P. Fankhauser, M. Hutter, M. A. Hoepflinger, and R. Siegwart, “State estimation for legged robots on unstable and slippery terrain,” in *IEEE/RSJ International Conference on Intelligent Robots and Systems (IROS)*, 2013, pp. 6058–6064. DOI: [10.1109/IROS.2013.6697236](https://doi.org/10.1109/IROS.2013.6697236).
- [106] M. Camurri, M. Fallon, S. Bazeille, *et al.*, “Probabilistic contact estimation and impact detection for state estimation of quadruped robots,” *IEEE Robotics and Automation Letters*, vol. 2, no. 2, pp. 1023–1030, 2017. DOI: [10.1109/LRA.2017.2652491](https://doi.org/10.1109/LRA.2017.2652491).
- [107] R. Szadkowski and J. Faigl, “Neurodynamic sensory-motor phase binding for multi-legged walking robots,” in *International Joint Conference on Neural Networks (IJCNN)*, 2020, pp. 1–8. DOI: [10.1109/IJCNN48605.2020.9207507](https://doi.org/10.1109/IJCNN48605.2020.9207507).
- [108] S. Aoi, P. Manoonpong, Y. Ambe, F. Matsuno, and F. Wörgötter, “Adaptive control strategies for interlimb coordination in legged robots: A review,” *Frontiers in Neurobotics*, vol. 11, p. 39, 2017. DOI: [10.3389/fnbot.2017.00039](https://doi.org/10.3389/fnbot.2017.00039).
- [109] H.-Y. Chung, C.-C. Hou, and S.-Y. Hsu, “A CPG-inspired controller for a hexapod robot with adaptive walking,” in *Automatic Control Conference (CACs)*, 2014, pp. 117–121.
- [110] M. Focchi, V. Barasuol, I. Havoutis, J. Buchli, C. Semini, and D. G. Caldwell, “Local reflex generation for obstacle negotiation in quadrupedal locomotion,” *Nature-Inspired Mobile Robotics*, pp. 443–450, 2013. DOI: [10.1142/9789814525534_0056](https://doi.org/10.1142/9789814525534_0056).
- [111] K. S. Espenschied, R. D. Quinn, R. D. Beer, and H. J. Chiel, “Biologically based distributed control and local reflexes improve rough terrain locomotion in a hexapod robot,” *Robotics and Autonomous Systems*, vol. 18, no. 1, pp. 59–64, 1996. DOI: [10.1016/0921-8890\(96\)00003-6](https://doi.org/10.1016/0921-8890(96)00003-6).
- [112] M. Luneckas, T. Luneckas, D. Udriš, D. Plonis, R. Maskeliunas, and R. Damasevicius, “A hybrid tactile sensor-based obstacle overcoming method for hexapod walking robots,” *Intelligent Service Robotics*, vol. 14, no. 1, pp. 9–24, 2021. DOI: [10.1007/s11370-020-00340-9](https://doi.org/10.1007/s11370-020-00340-9).
- [113] W. A. Lewinger and R. D. Quinn, “A hexapod walks over irregular terrain using a controller adapted from an insect’s nervous system,” in *IEEE/RSJ International Conference on Intelligent Robots and Systems (IROS)*, 2010, pp. 3386–3391. DOI: [10.1109/IROS.2010.5650200](https://doi.org/10.1109/IROS.2010.5650200).
- [114] P. Arena, P. Furia, L. Patané, and M. Pollino, “Fly-inspired sensory feedback in a reaction-diffusion neural system for locomotion control in a hexapod robot,” in *International Joint Conference on Neural Networks (IJCNN)*, 2015, pp. 1–8. DOI: [10.1109/IJCNN.2015.7280544](https://doi.org/10.1109/IJCNN.2015.7280544).
- [115] L. Wagner, P. Fankhauser, M. Bloesch, and M. Hutter, “Foot contact estimation for legged robots in rough terrain,” in *Advances in Cooperative Robotics*. 2016, pp. 395–403. DOI: [10.1142/9789813149137_0047](https://doi.org/10.1142/9789813149137_0047).

- [116] A. Winkler, I. Havoutis, S. Bazeille, *et al.*, “Path planning with force-based foothold adaptation and virtual model control for torque controlled quadruped robots,” in *IEEE International Conference on Robotics and Automation (ICRA)*, 2014, pp. 6476–6482. DOI: [10.1109/ICRA.2014.6907815](https://doi.org/10.1109/ICRA.2014.6907815).
- [117] M. Travers, J. Whitman, and H. Choset, “Shape-based coordination in locomotion control,” *International Journal of Robotics Research*, vol. 37, no. 10, pp. 1253–1268, 2018. DOI: [10.1177/0278364918761569](https://doi.org/10.1177/0278364918761569).
- [118] H. Zhang, R. Wu, C. Li, *et al.*, “A force-sensing system on legs for biomimetic hexapod robots interacting with unstructured terrain,” *Sensors*, vol. 17, no. 7, p. 1514, 2017. DOI: [10.3390/s17071514](https://doi.org/10.3390/s17071514).
- [119] K. Walas, “Foot design for a hexapod walking robot,” *Pomiary, Automatyka, Robotyka*, vol. 17, no. 2, pp. 283–287, 2013.
- [120] X. A. Wu, T. M. Huh, R. Mukherjee, and M. Cutkosky, “Integrated ground reaction force sensing and terrain classification for small legged robots,” *IEEE Robotics and Automation Letters*, vol. 1, no. 2, pp. 1125–1132, 2016. DOI: [10.1109/LRA.2016.2524073](https://doi.org/10.1109/LRA.2016.2524073).
- [121] V. Barasuol, J. Buchli, C. Semini, M. Frigerio, E. R. De Pieri, and D. G. Caldwell, “A reactive controller framework for quadrupedal locomotion on challenging terrain,” in *IEEE International Conference on Robotics and Automation (ICRA)*, 2013, pp. 2554–2561. DOI: [10.1109/ICRA.2013.6630926](https://doi.org/10.1109/ICRA.2013.6630926).
- [122] K. Walas, “Tactile sensing for ground classification,” *Journal of Intelligent & Robotic Systems*, vol. 7, no. 2, pp. 18–23, 2013.
- [123] M. Palankar, “A distributed local-leg feedback algorithm for robust walking on uneven terrain,” Ph.D. dissertation, University of South Florida, 2013, ISBN: 9781303263996.
- [124] M. Palankar and L. Palmer, “A force threshold-based position controller for legged locomotion: Toward local leg feedback algorithms for robust walking on uneven terrain,” *Autonomous Robots*, vol. 38, no. 3, pp. 301–316, 2015. DOI: [10.1007/s10514-014-9413-0](https://doi.org/10.1007/s10514-014-9413-0).
- [125] J. Mrva and J. Faigl, “Tactile sensing with servo drives feedback only for blind hexapod walking robot,” in *10th International Workshop on Robot Motion and Control (RoMoCo)*, 2015, pp. 240–245. DOI: [10.1109/RoMoCo.2015.7219742](https://doi.org/10.1109/RoMoCo.2015.7219742).
- [126] P. Fankhauser, M. Bloesch, and M. Hutter, “Probabilistic terrain mapping for mobile robots with uncertain localization,” *IEEE Robotics and Automation Letters*, vol. 3, no. 4, pp. 3019–3026, 2018. DOI: [10.1109/LRA.2018.2849506](https://doi.org/10.1109/LRA.2018.2849506).
- [127] A. Stelzer, H. Hirschmüller, and M. Görner, “Stereo-vision-based navigation of a six-legged walking robot in unknown rough terrain,” *International Journal of Robotics Research*, vol. 31, no. 4, pp. 381–402, 2012. DOI: [10.1177/0278364911435161](https://doi.org/10.1177/0278364911435161).

A. REFERENCES

- [128] D. Belter, P. Labecki, P. Fankhauser, and R. Siegwart, “RGB-D terrain perception and dense mapping for legged robots,” *International Journal of Applied Mathematics and Computer Science*, vol. 26, pp. 81–97, Mar. 2016. DOI: [10.1515/amcs-2016-0006](https://doi.org/10.1515/amcs-2016-0006).
- [129] D. Belter and P. Skrzypczyński, “Rough terrain mapping and classification for foothold selection in a walking robot,” *Journal of Field Robotics*, vol. 28, no. 4, pp. 497–528, 2011. DOI: [10.1002/rob.20397](https://doi.org/10.1002/rob.20397).
- [130] D. Wettergreen, “Robotic walking in natural terrain: Gait planning and behavior-based control for statically-stable walking robots,” Ph.D. dissertation, Carnegie Mellon University, 1995.
- [131] N. Perrin, C. Ott, J. Engelsberger, O. Stasse, F. Lamiroux, and I. D. G. Caldwell, “Continuous legged locomotion planning,” *IEEE Transactions on Robotics*, vol. 33, no. 1, pp. 234–239, 2017. DOI: [10.1109/TR0.2016.2623329](https://doi.org/10.1109/TR0.2016.2623329).
- [132] A. W. Winkler, C. Mastalli, I. Havoutis, M. Focchi, D. G. Caldwell, and C. Semini, “Planning and execution of dynamic whole-body locomotion for a hydraulic quadruped on challenging terrain,” in *IEEE International Conference on Robotics and Automation (ICRA)*, 2015, pp. 5148–5154. DOI: [10.1109/ICRA.2015.7139916](https://doi.org/10.1109/ICRA.2015.7139916).
- [133] R. Buchanan, T. Bandyopadhyay, M. Bjelonic, L. Wellhausen, M. Hutter, and N. Kottege, “Walking posture adaptation for legged robot navigation in confined spaces,” *IEEE Robotics and Automation Letters*, vol. 4, no. 2, pp. 2148–2155, 2019. DOI: [10.1109/LRA.2019.2899664](https://doi.org/10.1109/LRA.2019.2899664).
- [134] P. Manoonpong, L. Patanè, X. Xiong, *et al.*, “Insect-inspired robots: Bridging biological and artificial systems,” *Sensors*, vol. 21, no. 22, 2021. DOI: [10.3390/s21227609](https://doi.org/10.3390/s21227609).
- [135] T. G. Brown, “On the nature of the fundamental activity of the nervous centres; together with an analysis of the conditioning of rhythmic activity in progression, and a theory of the evolution of function in the nervous system,” *The Journal of Physiology*, vol. 48, no. 1, pp. 18–46, 1914.
- [136] C. Mantziaris, T. Bockemühl, and A. Büschges, “Central pattern generating networks in insect locomotion,” *Developmental Neurobiology*, vol. 80, no. 1-2, pp. 16–30, 2020. DOI: [10.1002/dneu.22738](https://doi.org/10.1002/dneu.22738).
- [137] G. Zhong, L. Chen, Z. Jiao, J. Li, and H. Deng, “Locomotion control and gait planning of a novel hexapod robot using biomimetic neurons,” *IEEE Transactions on Control Systems Technology*, vol. 26, no. 2, pp. 624–636, 2018. DOI: [10.1109/TCST.2017.2692727](https://doi.org/10.1109/TCST.2017.2692727).
- [138] S. Steingrube, M. Timme, F. Wörgötter, and P. Manoonpong, “Self-organized adaptation of a simple neural circuit enables complex robot behaviour,” *Nature Physics*, vol. 6, no. 3, pp. 224–230, 2010. DOI: [10.1038/nphys1508](https://doi.org/10.1038/nphys1508).

- [139] H. Cruse, T. Kindermann, M. Schumm, J. Dean, and J. Schmitz, “Walknet - a biologically inspired network to control six-legged walking,” *Neural Networks*, vol. 11, no. 7, pp. 1435–1447, 1998. DOI: [10.1016/S0893-6080\(98\)00067-7](https://doi.org/10.1016/S0893-6080(98)00067-7).
- [140] K. Matsuoka, “Mechanisms of frequency and pattern control in the neural rhythm generators,” *Biological Cybernetics*, vol. 56, no. 5-6, pp. 345–353, 1987.
- [141] G. Sartoretti, S. Shaw, K. Lam, N. Fan, M. Travers, and H. Choset, “Central pattern generator with inertial feedback for stable locomotion and climbing in unstructured terrain,” in *IEEE International Conference on Robotics and Automation (ICRA)*, 2018, pp. 5769–5775. DOI: [10.1109/ICRA.2018.8461013](https://doi.org/10.1109/ICRA.2018.8461013).
- [142] P. Ngamkajornwiwat, J. Homchanthanakul, P. Teerakittikul, and P. Manoonpong, “Bio-inspired adaptive locomotion control system for online adaptation of a walking robot on complex terrains,” *IEEE Access*, vol. 8, pp. 91 587–91 602, 2020. DOI: [10.1109/ACCESS.2020.2992794](https://doi.org/10.1109/ACCESS.2020.2992794).
- [143] M. Vukobratović and B. Borovac, “Zero-moment point – thirty five years of its life,” *International Journal of Humanoid Robotics*, vol. 01, no. 01, pp. 157–173, 2004. DOI: [10.1142/S0219843604000083](https://doi.org/10.1142/S0219843604000083).
- [144] K. Masuya and K. Ayusawa, “A review of state estimation of humanoid robot targeting the center of mass, base kinematics, and external wrench,” *Advanced Robotics*, vol. 34, no. 21–22, pp. 1380–1389, 2020. DOI: [10.1080/01691864.2020.1835532](https://doi.org/10.1080/01691864.2020.1835532).
- [145] M. Raibert, M. Chepponis, and H. Brown, “Running on four legs as though they were one,” *IEEE Journal on Robotics and Automation*, vol. 2, no. 2, pp. 70–82, 1986. DOI: [10.1109/JRA.1986.1087044](https://doi.org/10.1109/JRA.1986.1087044).
- [146] J. Pratt, C.-M. Chew, A. Torres, P. Dilworth, and G. Pratt, “Virtual model control: An intuitive approach for bipedal locomotion,” *International Journal of Robotics Research*, vol. 20, no. 2, pp. 129–143, 2001. DOI: [10.1177/02783640122067309](https://doi.org/10.1177/02783640122067309).
- [147] C. Gonzalez, V. Barasuol, M. Frigerio, R. Featherstone, D. G. Caldwell, and C. Semini, “Line walking and balancing for legged robots with point feet,” in *IEEE/RSJ International Conference on Intelligent Robots and Systems (IROS)*, 2020, pp. 3649–3656. DOI: [10.1109/IROS45743.2020.9341743](https://doi.org/10.1109/IROS45743.2020.9341743).
- [148] M. Neunert, M. Stäuble, M. Giffthaler, *et al.*, “Whole-body nonlinear model predictive control through contacts for quadrupeds,” *IEEE Robotics and Automation Letters*, vol. 3, no. 3, pp. 1458–1465, 2018. DOI: [10.1109/LRA.2018.2800124](https://doi.org/10.1109/LRA.2018.2800124).

A. REFERENCES

- [149] C. Dario Bellicoso, C. Gehring, J. Hwangbo, P. Fankhauser, and M. Hutter, “Perception-less terrain adaptation through whole body control and hierarchical optimization,” in *IEEE/RAS International Conference on Humanoid Robots (Humanoids)*, 2016, pp. 558–564. DOI: [10.1109/HUMANOIDS.2016.7803330](https://doi.org/10.1109/HUMANOIDS.2016.7803330).
- [150] R. Grandia, F. Farshidian, R. Ranftl, and M. Hutter, “Feedback mpc for torque-controlled legged robots,” in *IEEE/RSJ International Conference on Intelligent Robots and Systems (IROS)*, 2019, pp. 4730–4737. DOI: [10.1109/IROS40897.2019.8968251](https://doi.org/10.1109/IROS40897.2019.8968251).
- [151] F. Farshidian, E. Jelavić, A. W. Winkler, and J. Buchli, “Robust whole-body motion control of legged robots,” in *IEEE/RSJ International Conference on Intelligent Robots and Systems (IROS)*, 2017, pp. 4589–4596. DOI: [10.1109/IROS.2017.8206328](https://doi.org/10.1109/IROS.2017.8206328).
- [152] T. Miki, J. Lee, J. Hwangbo, L. Wellhausen, V. Koltun, and M. Hutter, “Learning robust perceptive locomotion for quadrupedal robots in the wild,” *Science Robotics*, vol. 7, no. 62, eabk2822, 2022. DOI: [10.1126/scirobotics.abk2822](https://doi.org/10.1126/scirobotics.abk2822).
- [153] J. Tan, T. Zhang, E. Coumans, *et al.*, “Sim-to-Real: Learning agile locomotion for quadruped robots,” in *Robotics: Science and Systems (RSS)*, 2018.
- [154] T. Erez, Y. Tassa, and E. Todorov, “Simulation tools for model-based robotics: Comparison of Bullet, Havok, MuJoCo, ODE and PhysX,” in *IEEE International Conference on Robotics and Automation (ICRA)*, 2015, pp. 4397–4404. DOI: [10.1109/ICRA.2015.7139807](https://doi.org/10.1109/ICRA.2015.7139807).
- [155] T. Azayev and K. Zimmerman, “Blind hexapod locomotion in complex terrain with gait adaptation using deep reinforcement learning and classification,” *Journal of Intelligent & Robotic Systems*, vol. 99, no. 3–4, SI, pp. 659–671, 2020. DOI: [10.1007/s10846-020-01162-8](https://doi.org/10.1007/s10846-020-01162-8).
- [156] R. Featherstone, *Rigid Body Dynamics Algorithms*. Springer-Verlag, New York, 2008.
- [157] F. Flacco, A. Paolillo, and A. Kheddar, “Residual-based contacts estimation for humanoid robots,” in *IEEE/RAS International Conference on Humanoid Robots*, 2016, pp. 409–415. DOI: [10.1109/HUMANOIDS.2016.7803308](https://doi.org/10.1109/HUMANOIDS.2016.7803308).
- [158] V. Morlando, A. Teimoorzadeh, and F. Ruggiero, “Whole-body control with disturbance rejection through a momentum-based observer for quadruped robots,” *Mechanism and Machine Theory*, vol. 164, p. 104412, 2021. DOI: [10.1016/j.mechmachtheory.2021.104412](https://doi.org/10.1016/j.mechmachtheory.2021.104412).
- [159] T. Dudzik, M. Chignoli, G. Bledt, *et al.*, “Robust autonomous navigation of a small-scale quadruped robot in real-world environments,” in *IEEE/RSJ International Conference on Intelligent Robots and Systems (IROS)*, 2020, pp. 3664–3671. DOI: [10.1109/IROS45743.2020.9340701](https://doi.org/10.1109/IROS45743.2020.9340701).

- [160] Z. Cong, A. Honglei, C. Wu, L. Lang, Q. Wei, and M. Hongxu, “Contact force estimation method of legged-robot and its application in impedance control,” *IEEE Access*, vol. 8, pp. 161 175–161 187, 2020. DOI: [10.1109/ACCESS.2020.3021080](https://doi.org/10.1109/ACCESS.2020.3021080).
- [161] J. Lee, J. Ahn, D. Kim, S. H. Bang, and L. Sentis, “Online gain adaptation of whole-body control for legged robots with unknown disturbances,” *Frontiers in Robotics and AI*, vol. 8, 2022. DOI: [10.3389/frobt.2021.788902](https://doi.org/10.3389/frobt.2021.788902).
- [162] S. Haddadin, *Towards safe robots: approaching Asimov’s 1st law*. Springer-Verlag Berlin, 2013, vol. 90. DOI: [10.1007/978-3-642-40308-8](https://doi.org/10.1007/978-3-642-40308-8).
- [163] A. De Luca and R. Mattone, “Actuator failure detection and isolation using generalized momenta,” in *IEEE International Conference on Robotics and Automation (ICRA)*, vol. 1, 2003, pp. 634–639. DOI: [10.1109/ROBOT.2003.1241665](https://doi.org/10.1109/ROBOT.2003.1241665).
- [164] A. Wahrburg, J. Bös, K. D. Listmann, F. Dai, B. Matthias, and H. Ding, “Motor-current-based estimation of cartesian contact forces and torques for robotic manipulators and its application to force control,” *IEEE Transactions on Automation Science and Engineering*, vol. 15, no. 2, pp. 879–886, 2018. DOI: [10.1109/TASE.2017.2691136](https://doi.org/10.1109/TASE.2017.2691136).
- [165] G. Garofalo, N. Mansfeld, J. Jankowski, and C. Ott, “Sliding mode momentum observers for estimation of external torques and joint acceleration,” in *IEEE International Conference on Robotics and Automation (ICRA)*, 2019, pp. 6117–6123. DOI: [10.1109/ICRA.2019.8793529](https://doi.org/10.1109/ICRA.2019.8793529).
- [166] J. Dong, J. Xu, L. Wang, A. Liu, and L. Yu, “External force estimation of the industrial robot based on the error probability model and swvakf,” *IEEE Transactions on Instrumentation and Measurement*, vol. 71, pp. 1–11, 2022. DOI: [10.1109/TIM.2022.3209742](https://doi.org/10.1109/TIM.2022.3209742).
- [167] T. Tomić and S. Haddadin, “A unified framework for external wrench estimation, interaction control and collision reflexes for flying robots,” in *IEEE/RSJ International Conference on Intelligent Robots and Systems (IROS)*, 2014, pp. 4197–4204. DOI: [10.1109/IROS.2014.6943154](https://doi.org/10.1109/IROS.2014.6943154).
- [168] F. Ruggiero, V. Lippiello, and A. Ollero, “Aerial manipulation: A literature review,” *IEEE Robotics and Automation Letters*, vol. 3, no. 3, pp. 1957–1964, 2018. DOI: [10.1109/LRA.2018.2808541](https://doi.org/10.1109/LRA.2018.2808541).
- [169] H. A. O. Mohamed, G. Nava, G. L’Erario, *et al.*, “Momentum-based extended kalman filter for thrust estimation on flying multibody robots,” *IEEE Robotics and Automation Letters*, vol. 7, no. 1, pp. 526–533, 2022. DOI: [10.1109/LRA.2021.3129258](https://doi.org/10.1109/LRA.2021.3129258).
- [170] M. Benallegue, P. Gergondet, H. Audrerr, *et al.*, “Model-based external force/moment estimation for humanoid robots with no torque measurement,” in *IEEE International Conference on Robotics and Automation (ICRA)*, 2018, pp. 3122–3129. DOI: [10.1109/ICRA.2018.8460809](https://doi.org/10.1109/ICRA.2018.8460809).

A. REFERENCES

- [171] L. Hawley, R. Rahem, and W. Suleiman, “External force observer for small- and medium-sized humanoid robots,” *International Journal of Humanoid Robotics*, vol. 16, no. 06, p. 1950030, 2019. DOI: [10.1142/S0219843619500300](https://doi.org/10.1142/S0219843619500300).
- [172] S. Piperakis, M. Koskinopoulou, and P. Trahanias, “Nonlinear state estimation for humanoid robot walking,” *IEEE Robotics and Automation Letters*, vol. 3, no. 4, pp. 3347–3354, 2018. DOI: [10.1109/LRA.2018.2852788](https://doi.org/10.1109/LRA.2018.2852788).
- [173] K. S. Fu, R. Gonzalez, and C. G. Lee, *Robotics: Control, Sensing, Vision and Intelligence*. Tata McGraw-Hill Education, 1987.
- [174] L. Zaccarian, *DC motors: Dynamic model and control techniques*, Lecture notes, Roma, Italy, 2012., (@Online) <http://control.disp.uniroma2.it/~zack/LabRob/DCmotors.pdf>
- [175] O. Sigaud, C. Salaun, and V. Padois, “On-line regression algorithms for learning mechanical models of robots: A survey,” *Robotics and Autonomous Systems*, vol. 59, no. 12, pp. 1115–1129, 2011. DOI: [10.1016/j.robot.2011.07.006](https://doi.org/10.1016/j.robot.2011.07.006).
- [176] N. A. Iqteit, K. Yahya, F. M. Makahleh, *et al.*, “Simple mathematical and simulink model of stepper motor,” *Energies*, vol. 15, no. 17, 2022. DOI: [10.3390/en15176159](https://doi.org/10.3390/en15176159).
- [177] L. Wargula, P. Krawiec, J. M. Adamiec, and K. J. Walus, “The investigations of dynamic characteristics of a stepper motor,” *Procedia Engineering*, vol. 177, pp. 318–323, 2017. DOI: [10.1016/j.proeng.2017.02.232](https://doi.org/10.1016/j.proeng.2017.02.232).
- [178] J. Zelinka, M. Prágr, R. Szadkowski, J. Bayer, and J. Faigl, “Traversability transfer learning between robots with different cost assessment policies,” in *2021 Modelling and Simulation for Autonomous Systems (MESAS)*, vol. 13207, 2022, pp. 333–344. DOI: [10.1007/978-3-030-98260-7_21](https://doi.org/10.1007/978-3-030-98260-7_21).
- [179] W. Cheah, H. H. Khalili, S. Watson, P. Green, and B. Lennox, “Grid-based motion planning using advanced motions for hexapod robots,” in *IEEE/RSJ International Conference on Intelligent Robots and Systems (IROS)*, 2018, pp. 3573–3578. DOI: [10.1109/IROS.2018.8593964](https://doi.org/10.1109/IROS.2018.8593964).

Citations of Author's Publications

Citations of the author's work were extracted from the Web of Science. First- and second-order self-citations are excluded. The data were gathered on March 1st, 2023. The publications and their citations are sorted from the newest to the oldest.

[1c] P. Čížek, M. Zoula, and J. Faigl, "Design, construction, and rough-terrain locomotion control of novel hexapod walking robot with four degrees of freedom per leg," *IEEE Access*, vol. 9, pp. 17 866–17 881, 2021. DOI: [10.1109/ACCESS.2021.3053492](https://doi.org/10.1109/ACCESS.2021.3053492)

- A. Torres-Pardo, D. Pinto-Fernandez, M. Garabini, F. Angelini, D. Rodriguez-Cianca, S. Massardi, *et al.*, "Legged locomotion over irregular terrains: State of the art of human and robot performance," *Bioinspiration & Biomimetics*, vol. 17, no. 6, 2022. DOI: [10.1088/1748-3190/ac92b3](https://doi.org/10.1088/1748-3190/ac92b3)
- P. E. Schiebel, J. Shum, H. Cerbone, and R. J. Wood, "An insect-scale robot reveals the effects of different body dynamics regimes during open-loop running in feature-laden terrain," *Bioinspiration & Biomimetics*, vol. 17, no. 2, 2022. DOI: [10.1088/1748-3190/ac3f7d](https://doi.org/10.1088/1748-3190/ac3f7d)
- P. Manoonpong, L. Patanè, X. Xiong, I. Brodoline, J. Dupeyroux, S. Violette, *et al.*, "Insect-inspired robots: Bridging biological and artificial systems," *Sensors*, vol. 21, no. 22, 2021. DOI: [10.3390/s21227609](https://doi.org/10.3390/s21227609)
- W. Huang, J. Xiao, F. Zeng, P. Lu, G. Lin, W. Hu, *et al.*, "A quadruped robot with three-dimensional flexible legs," *Sensors*, vol. 21, no. 14, 2021. DOI: [10.3390/s21144907](https://doi.org/10.3390/s21144907)

[10a] T. Rouček, M. Pecka, P. Čížek, J. Bayer, V. Šalanský, D. Heřt, *et al.*, "Darpa subterranean challenge: Multi-robotic exploration of underground environments," in *2019 Modelling and Simulation for Autonomous Systems (MESAS)*, 2020, pp. 274–290. DOI: [10.1007/978-3-030-43890-6_22](https://doi.org/10.1007/978-3-030-43890-6_22)

- N. Aoki and G. Ishigami, "Autonomous tracking and landing of an unmanned aerial vehicle on a ground vehicle in rough terrain," *Advanced Robotics*, vol. 0, no. 0, pp. 1–12, DOI: [10.1080/01691864.2022.2141078](https://doi.org/10.1080/01691864.2022.2141078)
- R. Giubilato, W. Stuerzl, A. Wedler, and R. Triebel, "Challenges of SLAM in extremely unstructured environments: The DLR planetary stereo, solid-

A. CITATIONS OF AUTHOR'S PUBLICATIONS

- state LiDAR, inertial dataset,” *IEEE Robotics and Automation Letters*, vol. 7, no. 4, pp. 8721–8728, 2022. DOI: [10.1109/LRA.2022.3188118](https://doi.org/10.1109/LRA.2022.3188118)
- A. Singletary, M. Ahmadi, and A. D. Ames, “Safe control for nonlinear systems with stochastic uncertainty via risk control barrier functions,” *IEEE Control Systems Letters*, vol. 7, pp. 349–354, 2022. DOI: [10.1109/LCSYS.2022.3187458](https://doi.org/10.1109/LCSYS.2022.3187458)
 - B. Lindqvist, S. Karlsson, A. Koval, I. Tevetzidis, J. Haluska, C. Kanellakis, *et al.*, “Multimodality robotic systems: Integrated combined legged-aerial mobility for subterranean search-and-rescue,” *Robotics and Autonomous Systems*, vol. 154, 2022. DOI: [10.1016/j.robot.2022.104134](https://doi.org/10.1016/j.robot.2022.104134)
 - M. Etxeberria-Garcia, M. Zamalloa, N. Arana-Arexolaleiba, and M. Labayen, “Visual odometry in challenging environments: An urban underground railway scenario case,” *IEEE Access*, vol. 10, pp. 69 200–69 215, 2022. DOI: [10.1109/ACCESS.2022.3187209](https://doi.org/10.1109/ACCESS.2022.3187209)
 - J. Li, B. Yang, Y. Chen, W. Wu, Y. Yang, X. Zhao, *et al.*, “Evaluation of a compact helmet-based laser scanning system for aboveground and underground 3D mapping,” in *24th ISPRS Congress on Imaging Today, Foreseeing Tomorrow*, vol. 43–B2, 2022, pp. 215–220. DOI: [10.5194/isprs-archives-XLIII-B2-2022-215-2022](https://doi.org/10.5194/isprs-archives-XLIII-B2-2022-215-2022)
 - B. Bendris and J. Cayero Becerra, “Design and experimental evaluation of an aerial solution for visual inspection of tunnel-like infrastructures,” *Remote Sensing*, vol. 14, no. 1, 2022. DOI: [10.3390/rs14010195](https://doi.org/10.3390/rs14010195)
 - C. Azevedo, A. Matos, P. U. Lima, and J. Avendano, “Petri net toolbox for multi-robot planning under uncertainty,” *Applied Sciences*, vol. 11, no. 24, 2021. DOI: [10.3390/app112412087](https://doi.org/10.3390/app112412087)
 - A. Norton, P. Gavriel, B. Donoghue, and H. Yanco, “Test methods to evaluate mapping capabilities of small unmanned aerial systems in constrained indoor and subterranean environments,” in *IEEE International Symposium on Technologies for Homeland Security*, 2021. DOI: [10.1109/HST53381.2021.9619836](https://doi.org/10.1109/HST53381.2021.9619836)
 - A. Dixit, M. Ahmadi, and J. W. Burdick, “Risk-sensitive motion planning using entropic value-at-risk,” in *European Control Conference (ECC)*, 2021, pp. 1726–1732
 - M. Selden, J. Zhou, F. Campos, N. Lambert, D. Drew, and K. S. J. Pister, “BotNet: A simulator for studying the effects of accurate communication models on multi-agent and swarm control,” in *International Symposium on Multi-Robot and Multi-Agent Systems (MRS)*, 2021, pp. 101–109. DOI: [10.1109/MRS50823.2021.9620611](https://doi.org/10.1109/MRS50823.2021.9620611)

- L. Qingqing, Y. Xianjia, J. P. Queralta, and T. Westerlund, “Adaptive LiDAR scan frame integration: Tracking known MAVs in 3D point clouds,” in *International Conference on Advanced Robotics (ICAR)*, 2021, pp. 1079–1086. DOI: [10.1109/ICAR53236.2021.9659483](https://doi.org/10.1109/ICAR53236.2021.9659483)

[12a] P. Čížek and J. Faigl, “Self-supervised learning of the biologically-inspired obstacle avoidance of hexapod walking robot,” *Bioinspiration & Biomimetics*, vol. 14, no. 4, p. 046 002, 2019. DOI: [10.1088/1748-3190/ab1a9c](https://doi.org/10.1088/1748-3190/ab1a9c)

- Y. Zhou, A. Chen, X. He, and X. Bian, “Multi-target coordinated search algorithm for swarm robotics considering practical constraints,” *Frontiers in Neurobotics*, vol. 15, 2021. DOI: [10.3389/fnbot.2021.753052](https://doi.org/10.3389/fnbot.2021.753052)
- Q. Fu, X. Sun, T. Liu, C. Hu, and S. Yue, “Robustness of bio-inspired visual systems for collision prediction in critical robot traffic,” *Frontiers in Robotics and AI*, vol. 8, 2021. DOI: [10.3389/frobt.2021.529872](https://doi.org/10.3389/frobt.2021.529872)
- Y. Zhou, A. Chen, X. He, and X. Bian, “Multi-target coordinated search algorithm for swarm robotics considering practical constraints,” *Frontiers in Neurobotics*, vol. 15, 2021. DOI: [10.3389/fnbot.2021.753052](https://doi.org/10.3389/fnbot.2021.753052)
- Q. Fu, H. Wang, J. Peng, and S. Yue, “Improved collision perception neuronal system model with adaptive inhibition mechanism and evolutionary learning,” *IEEE Access*, vol. 8, pp. 108 896–108 912, 2020. DOI: [10.1109/ACCESS.2020.3001396](https://doi.org/10.1109/ACCESS.2020.3001396)

[14a] M. Prágr, P. Čížek, J. Bayer, and J. Faigl, “Online incremental learning of the terrain traversal cost in autonomous exploration,” in *Robotics: Science and Systems (RSS)*, 2019. DOI: [10.15607/RSS.2019.XV.040](https://doi.org/10.15607/RSS.2019.XV.040)

- H. Azpurua, A. F. M. Campos, and D. G. Macharet, “Three-dimensional terrain aware autonomous exploration for subterranean and confined spaces,” in *IEEE International Conference on Robotics and Automation (ICRA)*, 2021, pp. 2443–2449. DOI: [10.1109/ICRA48506.2021.9561099](https://doi.org/10.1109/ICRA48506.2021.9561099)
- M. Sivaprakasam, S. Triest, W. Wang, P. Yin, and S. Scherer, “Improving off-road planning techniques with learned costs from physical interactions,” in *IEEE International Conference on Robotics and Automation (ICRA)*, 2021, pp. 4844–4850. DOI: [10.1109/ICRA48506.2021.9561881](https://doi.org/10.1109/ICRA48506.2021.9561881)
- A. Kurobe, Y. Nakajima, K. Kitani, and H. Saito, “Audio-visual self-supervised terrain type recognition for ground mobile platforms,” *IEEE Access*, vol. 9, pp. 29 970–29 979, 2021. DOI: [10.1109/ACCESS.2021.3059620](https://doi.org/10.1109/ACCESS.2021.3059620)

A. CITATIONS OF AUTHOR'S PUBLICATIONS

- V. Karolj, A. Viseras, L. Merino, and D. Shutin, “An integrated strategy for autonomous exploration of spatial processes in unknown environments,” *Sensors*, vol. 20, no. 13, 2020. DOI: [10.3390/s20133663](https://doi.org/10.3390/s20133663)

[2c] J. Faigl and P. Čížek, “Adaptive locomotion control of hexapod walking robot for traversing rough terrains with position feedback only,” *Robotics and Autonomous Systems*, vol. 116, pp. 136–147, 2019. DOI: [10.1016/j.robot.2019.03.008](https://doi.org/10.1016/j.robot.2019.03.008)

- S. Halder, K. Afsari, J. Serdakowski, S. DeVito, M. Ensafi, and W. Thabet, “Real-time and remote construction progress monitoring with a quadruped robot using augmented reality,” *Buildings*, vol. 12, no. 11, 2022. DOI: [10.3390/buildings12112027](https://doi.org/10.3390/buildings12112027)
- A. Torres-Pardo, D. Pinto-Fernandez, M. Garabini, F. Angelini, D. Rodriguez-Cianca, S. Massardi, *et al.*, “Legged locomotion over irregular terrains: State of the art of human and robot performance,” *Bioinspiration & Biomimetics*, vol. 17, no. 6, 2022. DOI: [10.1088/1748-3190/ac92b3](https://doi.org/10.1088/1748-3190/ac92b3)
- L. M. Esteves, R. Cardim, M. C. M. Teixeira, D. R. de Oliveira, J. M. d. S. Ribeiro, E. Assuncao, *et al.*, “Implementations of full state feedback robust control designs for mechanical systems using only positions or velocities output feedback,” *IEEE Access*, vol. 10, pp. 23 234–23 247, 2022. DOI: [10.1109/ACCESS.2022.3154111](https://doi.org/10.1109/ACCESS.2022.3154111)
- Z. Chen, J. Liu, and F. Gao, “Real-time gait planning method for six-legged robots to optimize the performances of terrain adaptability and walking speed,” *Mechanism and Machine Theory*, vol. 168, 2022. DOI: [10.1016/j.mechmachtheory.2021.104545](https://doi.org/10.1016/j.mechmachtheory.2021.104545)
- J. Homchanchanakul and P. Manoonpong, “Continuous online adaptation of bioinspired adaptive neuroendocrine control for autonomous walking robots,” *IEEE Transactions on Neural Networks and Learning Systems*, vol. 33, no. 5, pp. 1833–1845, 2022. DOI: [10.1109/TNNLS.2021.3119127](https://doi.org/10.1109/TNNLS.2021.3119127)
- B. Wang, X. Cui, J. Sun, and Y. Gao, “Parameters optimization of central pattern generators for hexapod robot based on multi-objective genetic algorithm,” *International Journal of Advanced Robotic Systems*, vol. 18, no. 5, 2021. DOI: [10.1177/17298814211044934](https://doi.org/10.1177/17298814211044934)
- J. Coelho, F. Ribeiro, B. Dias, G. Lopes, and P. Flores, “Trends in the control of hexapod robots: A survey,” *Robotics*, vol. 10, no. 3, 2021. DOI: [10.3390/robotics10030100](https://doi.org/10.3390/robotics10030100)
- M. Thor, T. Kulvicius, and P. Manoonpong, “Generic neural locomotion control framework for legged robots,” *IEEE Transactions on Neural Networks*

- and Learning Systems*, vol. 32, no. 9, pp. 4013–4025, 2021. DOI: [10.1109/TNNLS.2020.3016523](https://doi.org/10.1109/TNNLS.2020.3016523)
- Z. Chen, Y. Tian, F. Gao, and J. Liu, “Locomotion speed capability analysis of six-legged robots: Optimization and application,” *Journal of Mechanical Engineering Science*, vol. 235, no. 21, pp. 5434–5449, 2021. DOI: [10.1177/0954406220981113](https://doi.org/10.1177/0954406220981113)
 - J. Li, B. You, L. Ding, X. Yu, W. Li, T. Zhang, *et al.*, “Dual-master/single-slave haptic teleoperation system for semiautonomous bilateral control of hexapod robot subject to deformable rough terrain,” *IEEE Transactions on Systems Man and Cybernetics-systems*, vol. 52, no. 4, pp. 2435–2449, 2022. DOI: [10.1109/TSMC.2021.3049848](https://doi.org/10.1109/TSMC.2021.3049848)
 - M. Ehrlich and E. E. Tsur, “Neuromorphic adaptive body leveling in a bioinspired hexapod walking robot,” in *IEEE Biomedical Circuits and Systems Conference (BioCAS)*, 2021. DOI: [10.1109/BIOCAS49922.2021.9644943](https://doi.org/10.1109/BIOCAS49922.2021.9644943)
 - M. Luneckas, T. Luneckas, D. Udris, D. Plonis, R. Maskeliunas, and R. Damasevicius, “A hybrid tactile sensor-based obstacle overcoming method for hexapod walking robots,” *Intelligent Service Robotics*, vol. 14, no. 1, pp. 9–24, 2021. DOI: [10.1007/s11370-020-00340-9](https://doi.org/10.1007/s11370-020-00340-9)
 - F. Zhang, S. Teng, Y. Wang, Z. Guo, J. Wang, and R. Xu, “Design of bionic goat quadruped robot mechanism and walking gait planning,” *International Journal of Agricultural and Biological Engineering*, vol. 13, no. 5, pp. 32–39, 2020. DOI: [10.25165/j.ijabe.20201305.5769](https://doi.org/10.25165/j.ijabe.20201305.5769)
 - H. H. Khalili, W. Cheah, T. B. Garcia-Nathan, J. Carrasco, S. Watson, and B. Lennox, “Tuning and sensitivity analysis of a hexapod state estimator,” *Robotics and Autonomous Systems*, vol. 129, p. 103 509, 2020. DOI: [10.1016/j.robot.2020.103509](https://doi.org/10.1016/j.robot.2020.103509)
 - L. Zhang, F. Wang, Z. Gao, S. Gao, and C. Li, “Research on the stationarity of hexapod robot posture adjustment,” *Sensors*, vol. 20, no. 10, 2020. DOI: [10.3390/s20102859](https://doi.org/10.3390/s20102859)
 - W. Li and F. Kang, “Design and analysis of steering and lifting mechanisms for forestry vehicle chassis,” *Mathematical Problems in Engineering*, vol. 2020, 2020. DOI: [10.1155/2020/5971746](https://doi.org/10.1155/2020/5971746)
 - H. Yu, H. Gao, and Z. Deng, “Enhancing adaptability with local reactive behaviors for hexapod walking robot via sensory feedback integrated central pattern generator,” *Robotics and Autonomous Systems*, vol. 124, 2020. DOI: [10.1016/j.robot.2019.103401](https://doi.org/10.1016/j.robot.2019.103401)
 - M. Tikam, D. Withey, and N. J. Theron, “Posture control for a low-cost commercially-available hexapod robot,” in *IEEE International Conference on Robotics and Automation (ICRA)*, 2020, pp. 4498–4504. DOI: [10.1109/ICRA40945.2020.9197147](https://doi.org/10.1109/ICRA40945.2020.9197147)

A. CITATIONS OF AUTHOR'S PUBLICATIONS

- M. A. Bell, L. Cattani, B. Gorissen, K. Bertoldi, J. C. Weaver, and R. J. Wood, “A soft, modular, and bi-stable dome actuator for programmable multi-modal locomotion,” in *IEEE/RSJ International Conference on Intelligent Robots and Systems (IROS)*, 2020, pp. 6529–6535. DOI: [10.1109/IROS45743.2020.9341138](https://doi.org/10.1109/IROS45743.2020.9341138)
- C. Ding, L. Zhou, Y. Li, and X. Rong, “Locomotion control of quadruped robots with online center of mass adaptation and payload identification,” *IEEE Access*, vol. 8, pp. 224578–224587, 2020. DOI: [10.1109/ACCESS.2020.3044933](https://doi.org/10.1109/ACCESS.2020.3044933)
- Z. Yan, H. Yang, W. Zhang, Q. Gong, and F. Lin, “Research on motion mode switching method based on CPG network reconstruction,” *IEEE Access*, vol. 8, pp. 224871–224883, 2020. DOI: [10.1109/ACCESS.2020.3045227](https://doi.org/10.1109/ACCESS.2020.3045227)
- L. Jia, Y. Wang, J. He, L. Liu, Z. Li, and Y. Shen, “Robust adaptive control based on machine learning and ntsmc for workpiece surface-grinding robot,” *International Journal of Robotics & Automation*, vol. 35, no. 6, pp. 444–453, 2020. DOI: [10.2316/J.2020.206-0449](https://doi.org/10.2316/J.2020.206-0449)
- Y. Xin, H. Chai, Y. Li, X. Rong, B. Li, and Y. Li, “Speed and acceleration control for a two wheel-leg robot based on distributed dynamic model and whole-body control,” *IEEE Access*, vol. 7, pp. 180630–180639, 2019. DOI: [10.1109/ACCESS.2019.2959333](https://doi.org/10.1109/ACCESS.2019.2959333)

[18a] M. Prágr, **P.Čížek**, and J. Faigl, “Incremental learning of traversability cost for aerial reconnaissance support to ground units,” in *2018 Modelling and Simulation for Autonomous Systems (MESAS)*, 2019, pp. 412–421. DOI: [10.1007/978-3-030-14984-0_30](https://doi.org/10.1007/978-3-030-14984-0_30)

- S. Sun, Y. Tong, B. Zhang, B. Yang, L. Yan, P. He, *et al.*, “A novel adaptive methodology for removing spurious components in a modified incremental gaussian mixture model,” *International Journal of Machine Learning and Cybernetics*, DOI: [10.1007/s13042-022-01649-w](https://doi.org/10.1007/s13042-022-01649-w)

[13a] M. Prágr, **P.Čížek**, and J. Faigl, “Cost of transport estimation for legged robot based on terrain features inference from aerial scan,” in *IEEE/RSJ International Conference on Intelligent Robots and Systems (IROS)*, 2018, pp. 1745–1750. DOI: [10.1109/IROS.2018.8593374](https://doi.org/10.1109/IROS.2018.8593374)

- S. Sun, Y. Tong, B. Zhang, B. Yang, L. Yan, P. He, *et al.*, “A novel adaptive methodology for removing spurious components in a modified incremental gaussian mixture model,” *International Journal of Machine Learning and Cybernetics*, DOI: [10.1007/s13042-022-01649-w](https://doi.org/10.1007/s13042-022-01649-w)

- Y. Chen, J. E. Grezmač, N. M. Graf, and K. A. Daltorio, "Sideways crab-walking is faster and more efficient than forward walking for a hexapod robot," *Bioinspiration & Biomimetics*, vol. 17, no. 4, 2022. DOI: [10.1088/1748-3190/ac6847](https://doi.org/10.1088/1748-3190/ac6847)
- P. Arena, L. Patane, and S. Taffara, "Energy efficiency of a quadruped robot with neuro-inspired control in complex environments," *Energies*, vol. 14, no. 2, 2021. DOI: [10.3390/en14020433](https://doi.org/10.3390/en14020433)
- J. Chen, C. Liu, H. Zhao, Y. Zhu, and J. Zhao, "Learning to identify footholds from geometric characteristics for a six-legged robot over rugged terrain," *Journal of Bionic Engineering*, vol. 17, no. 3, pp. 512–522, 2020. DOI: [10.1007/s42235-020-0041-4](https://doi.org/10.1007/s42235-020-0041-4)
- P. Ngamkajornwiwat, J. Homchanthanakul, P. Teerakittikul, and P. Manoonpong, "Bio-inspired adaptive locomotion control system for online adaptation of a walking robot on complex terrains," *IEEE Access*, vol. 8, pp. 91 587–91 602, 2020. DOI: [10.1109/ACCESS.2020.2992794](https://doi.org/10.1109/ACCESS.2020.2992794)

[19a] P. Čížek and J. Faigl, "Real-time FPGA-based detection of Speeded-Up Robust Features using separable convolution," *IEEE Transactions on Industrial Informatics*, vol. 14, no. 3, pp. 1155–1163, 2018. DOI: [10.1109/TII.2017.2764485](https://doi.org/10.1109/TII.2017.2764485)

- J. Ren, Z. Wang, Y. Zhang, and L. Liao, "YOLOv5-R: Lightweight real-time detection based on improved YOLOv5," *Journal of Electronic Imaging*, vol. 31, no. 3, 2022. DOI: [10.1117/1.JEI.31.3.033033](https://doi.org/10.1117/1.JEI.31.3.033033)
- V. Lomas-Barrie, R. Silva-Flores, A. Neme, and M. Pena-Cabrera, "A multi-view recognition method of predefined objects for robot assembly using deep learning and its implementation on an FPGA," *Electronics*, vol. 11, no. 5, 2022. DOI: [10.3390/electronics11050696](https://doi.org/10.3390/electronics11050696)
- E. Cho and Y. Kim, "Dynamic optimization of hessian determinant image pyramid for memory-efficient and high performance keypoint detection in surf," *IET Image Processing*, vol. 15, no. 13, pp. 3392–3399, 2021. DOI: [10.1049/ipr2.12336](https://doi.org/10.1049/ipr2.12336)
- Y. Zheng, Y. Sun, K. Muhammad, and V. H. C. de Albuquerque, "Weighted lic-based structure tensor with application to image content perception and processing," *IEEE Transactions on Industrial Informatics*, vol. 17, no. 3, pp. 2250–2260, 2021. DOI: [10.1109/TII.2020.2980577](https://doi.org/10.1109/TII.2020.2980577)
- V. Lomas-Barrie, M. Pena-Cabrera, I. Lopez-Juarez, and J. Luis Navarro-Gonzalez, "Fuzzy ARTMAP-based fast object recognition for robots using FPGA," *Electronics*, vol. 10, no. 3, 2021. DOI: [10.3390/electronics10030361](https://doi.org/10.3390/electronics10030361)

A. CITATIONS OF AUTHOR'S PUBLICATIONS

- S. G. Ali, Y. Chen, B. Sheng, H. Li, Q. Wu, P. Yang, *et al.*, “Cost-effective broad learning-based ultrasound biomicroscopy with 3D reconstruction for ocular anterior segmentation,” *Multimedia Tools and Applications*, vol. 80, no. 28–29, pp. 35 105–35 122, 2021. DOI: [10.1007/s11042-020-09303-9](https://doi.org/10.1007/s11042-020-09303-9)
- C. Wang, Y. Jiang, K. Wang, and F. Wei, “A field-programmable gate array system for sonar image recognition based on convolutional neural network,” *Journal of Systems and Control Engineering*, vol. 235, no. 10, SI, pp. 1808–1818, 2021. DOI: [10.1177/0959651820939345](https://doi.org/10.1177/0959651820939345)
- D.-J. Lee, S. G. Fuller, and A. S. McCown, “Optimization and implementation of synthetic basis feature descriptor on FPGA,” *Electronics*, vol. 9, no. 3, 2020. DOI: [10.3390/electronics9030391](https://doi.org/10.3390/electronics9030391)
- D. Liu, G. Zhou, D. Zhang, X. Zhou, and C. Li, “Ground control point automatic extraction for spaceborne georeferencing based on FPGA,” *IEEE Journal of Selected Topics in Applied Earth Observations and Remote Sensing*, vol. 13, pp. 3350–3366, 2020. DOI: [10.1109/JSTARS.2020.2998838](https://doi.org/10.1109/JSTARS.2020.2998838)
- P. Paces, W.-K. Yu, and J. Klesa, “Optical measurement methods for attitude determination of unmanned aerial systems,” in *IEEE-AIAA Digital Avionics Systems Conference (DASC)*, 2018, pp. 1287–1293

[5a] **P. Čížek** and J. Faigl, “On locomotion control using position feedback only in traversing rough terrains with hexapod crawling robot,” in *IOP Conference Series: Materials Science and Engineering*, vol. 428, 2018, p. 012065. DOI: [10.1088/1757-899x/428/1/012065](https://doi.org/10.1088/1757-899x/428/1/012065)

- A. Torres-Pardo, D. Pinto-Fernandez, M. Garabini, F. Angelini, D. Rodriguez-Cianca, S. Massardi, *et al.*, “Legged locomotion over irregular terrains: State of the art of human and robot performance,” *Bioinspiration & Biomimetics*, vol. 17, no. 6, 2022. DOI: [10.1088/1748-3190/ac92b3](https://doi.org/10.1088/1748-3190/ac92b3)
- J. Ma, G. Qiu, W. Guo, P. Li, and G. Ma, “Design, analysis and experiments of hexapod robot with six-link legs for high dynamic locomotion,” *Micromachines*, vol. 13, no. 9, 2022. DOI: [10.3390/mi13091404](https://doi.org/10.3390/mi13091404)
- V. Kalburgi, P. M. James, and P. Sreedharan, “Control system design for four-legged walking robot with insect type leg using ROS,” *Materials Today*, vol. 46, no. 10, pp. 5092–5097, 2021. DOI: [10.1016/j.matpr.2020.10.428](https://doi.org/10.1016/j.matpr.2020.10.428)
- T. Azayev and K. Zimmerman, “Blind hexapod locomotion in complex terrain with gait adaptation using deep reinforcement learning and classification,” *Journal of Intelligent & Robotic Systems*, vol. 99, no. 3–4, SI, pp. 659–671, 2020. DOI: [10.1007/s10846-020-01162-8](https://doi.org/10.1007/s10846-020-01162-8)

- J. Homchanthanakul, P. Ngamkajornwiwat, P. Teerakittikul, and P. Manoonpong, “Neural control with an artificial hormone system for energy-efficient compliant terrain locomotion and adaptation of walking robots,” in *IEEE/RSJ International Conference on Intelligent Robots and Systems (IROS)*, 2019, pp. 5475–5482. DOI: [10.1109/IROS40897.2019.8968580](https://doi.org/10.1109/IROS40897.2019.8968580)

[6a] P. Čížek, J. Kubík, and J. Faigl, “Online foot-strike detection using inertial measurements for multi-legged walking robot,” in *IEEE/RSJ International Conference on Intelligent Robots and Systems (IROS)*, 2018, pp. 7622–7627. DOI: [10.1109/IROS.2018.8594010](https://doi.org/10.1109/IROS.2018.8594010)

- J. Olensek, “A hexapod robot for an embedded system design and programming course,” *Elektrotehnicki vestnik*, vol. 89, no. 1-2, pp. 53–58, 2022
- H. Chang, J. Chang, G. Clifton, and N. Gravish, “Anisotropic compliance of robot legs improves recovery from swing-phase collisions,” *Bioinspiration & Biomimetics*, vol. 16, no. 5, 2021. DOI: [10.1088/1748-3190/ac0b99](https://doi.org/10.1088/1748-3190/ac0b99)

[7a] P. Čížek, J. Faigl, and D. Masri, “Foothold placement planning with a hexapod crawling robot,” in *IEEE/RSJ International Conference on Intelligent Robots and Systems (IROS)*, 2017, pp. 4096–4101. DOI: [10.1109/IROS.2017.8206267](https://doi.org/10.1109/IROS.2017.8206267)

- L. Ding, G. Wang, H. Gao, G. Liu, H. Yang, and Z. Deng, “Footstep planning for hexapod robots based on 3D quasi-static equilibrium support region,” *Journal of Intelligent & Robotic Systems*, vol. 103, no. 2, 2021. DOI: [10.1007/s10846-021-01469-0](https://doi.org/10.1007/s10846-021-01469-0)
- B. Xia, K. Che, Z. Tang, J. Wang, and M. Q. H. Meng, “Motion planning for hexapod robots in dynamic rough terrain environments,” in *IEEE International Conference on Robotics and Biomimetics (ROBIO)*, 2021, pp. 1611–1616. DOI: [10.1109/ROBIO54168.2021.9739381](https://doi.org/10.1109/ROBIO54168.2021.9739381)
- P. Wang, X. Zhou, Q. Zhao, J. Wu, and Q. Zhu, “Search-based kinodynamic motion planning for omnidirectional quadruped robots,” in *IEEE/ASME International Conference on Advanced Intelligent Mechatronics (AIM)*, 2021, pp. 823–829. DOI: [10.1109/AIM46487.2021.9517405](https://doi.org/10.1109/AIM46487.2021.9517405)
- J. E. Chamorro Fuertes, J. J. Marin Arciniegas, P. Bustos Garcia de Castro, and O. A. Vivas Alban, “Locomotion control of PhantomX hexapod robot with touch-pressure sensor and RoboComp,” in *IEEE Colombian Conference on Applications of Computational Intelligence (ColCACI)*, 2020

A. CITATIONS OF AUTHOR'S PUBLICATIONS

- W. Cheah, H. H. Khalili, S. Watson, P. Green, and B. Lennox, “Grid-based motion planning using advanced motions for hexapod robots,” in *IEEE/RSJ International Conference on Intelligent Robots and Systems (IROS)*, 2018, pp. 3573–3578. DOI: [10.1109/IROS.2018.8593964](https://doi.org/10.1109/IROS.2018.8593964)

[23a] M. Nowicki, D. Belter, A. Kostusiak, **P. Čížek**, J. Faigl, and P. Skrzypczyński, “An experimental study on feature-based SLAM for multi-legged robots with RGB-D sensors,” *Industrial Robot*, vol. 44, no. 4, pp. 428–441, 2017. DOI: [10.1108/IR-11-2016-0340](https://doi.org/10.1108/IR-11-2016-0340)

- A. Bento Filho, C. P. Tonetto, and R. M. de Andrade, “Four legged guara robot: From inspiration to implementation,” *Journal of Applied and Computational Mechanics*, vol. 7, no. 3, pp. 1425–1434, 2021. DOI: [10.22055/JACM.2021.35212.2613](https://doi.org/10.22055/JACM.2021.35212.2613)
- B. Li, Z. Mi, Y. Guo, Y. Yang, and M. S. Obaidat, “A high efficient multi-robot simultaneous localization and mapping system using partial computing offloading assisted cloud point registration strategy,” *Journal of Parallel and Distributed Computing*, vol. 149, pp. 89–102, 2021. DOI: [10.1016/j.jpdc.2020.10.012](https://doi.org/10.1016/j.jpdc.2020.10.012)
- H. H. Khalili, W. Cheah, T. B. Garcia-Nathan, J. Carrasco, S. Watson, and B. Lennox, “Tuning and sensitivity analysis of a hexapod state estimator,” *Robotics and Autonomous Systems*, vol. 129, p. 103509, 2020. DOI: [10.1016/j.robot.2020.103509](https://doi.org/10.1016/j.robot.2020.103509)
- J. Jiang, J. Wang, P. Wang, and Z. Chen, “POU-SLAM: Scan-to-model matching based on 3D voxels,” *Applied Sciences*, vol. 9, no. 19, 2019. DOI: [10.3390/app9194147](https://doi.org/10.3390/app9194147)
- M. T. K. Tsun, B. T. Lau, and H. S. Jo, “An improved indoor robot human-following navigation model using depth camera, active ir marker and proximity sensors fusion,” *Robotics*, vol. 7, no. 1, 2018. DOI: [10.3390/robotics7010004](https://doi.org/10.3390/robotics7010004)
- S. Xu, T. Wang, C. Lang, S. Feng, and Y. Jin, “Graph-based visual odometry for vslam,” *Industrial Robot*, vol. 45, no. 5, pp. 679–687, 2018. DOI: [10.1108/IR-04-2018-0061](https://doi.org/10.1108/IR-04-2018-0061)

[21a] **P. Čížek**, P. Milička, and J. Faigl, “Neural based obstacle avoidance with CPG controlled hexapod walking robot,” in *International Joint Conference on Neural Networks (IJCNN)*, 2017, pp. 650–656. DOI: [10.1109/IJCNN.2017.7965914](https://doi.org/10.1109/IJCNN.2017.7965914)

- C. Wu, F. Shuang, H. Wang, J. Zhao, and S. Yue, “Dynamic powerlines detection for uavs by attention fused looming detector,” in *International Joint Conference on Neural Networks (IJCNN)*, 2022. DOI: [10.1109/IJCNN55064.2022.9892035](https://doi.org/10.1109/IJCNN55064.2022.9892035)
- B. Wang, X. Cui, J. Sun, and Y. Gao, “Parameters optimization of central pattern generators for hexapod robot based on multi-objective genetic algorithm,” *International Journal of Advanced Robotic Systems*, vol. 18, no. 5, 2021. DOI: [10.1177/17298814211044934](https://doi.org/10.1177/17298814211044934)
- Q. Fu, X. Sun, T. Liu, C. Hu, and S. Yue, “Robustness of bio-inspired visual systems for collision prediction in critical robot traffic,” *Frontiers in Robotics and AI*, vol. 8, 2021. DOI: [10.3389/frobt.2021.529872](https://doi.org/10.3389/frobt.2021.529872)
- Q. Fu, C. Hu, J. Peng, F. C. Rind, and S. Yue, “A robust collision perception visual neural network with specific selectivity to darker objects,” *IEEE Transactions on Cybernetics*, vol. 50, no. 12, pp. 5074–5088, 2020. DOI: [10.1109/TCYB.2019.2946090](https://doi.org/10.1109/TCYB.2019.2946090)
- Q. Fu and S. Yue, “Complementary visual neuronal systems model for collision sensing,” in *IEEE International Conference on Advanced Robotics and Mechatronics (ICARM)*, 2020, pp. 609–615
- A. Spaeth, M. Tebyani, D. Haussler, and M. Teodorescu, “Neuromorphic closed-loop control of a flexible modular robot by a simulated spiking central pattern generator,” in *IEEE International Conference on Soft Robotics (RoboSoft)*, 2020, pp. 46–51
- Q. Fu, H. Wang, J. Peng, and S. Yue, “Improved collision perception neuronal system model with adaptive inhibition mechanism and evolutionary learning,” *IEEE Access*, vol. 8, pp. 108 896–108 912, 2020. DOI: [10.1109/ACCESS.2020.3001396](https://doi.org/10.1109/ACCESS.2020.3001396)
- Q. Fu, H. Wang, C. Hu, and S. Yue, “Towards computational models and applications of insect visual systems for motion perception: A review,” *Artificial Life*, vol. 25, no. 3, pp. 263–311, 2019. DOI: [10.1162/artl_a__00297](https://doi.org/10.1162/artl_a__00297)
- Y. Zhu, T. Guo, Q. Liu, Q. Zhu, X. Zhao, and B. Jin, “Turning and radius deviation correction for a hexapod walking robot based on an ant-inspired sensory strategy,” *Sensors*, vol. 17, no. 12, 2017. DOI: [10.3390/s17122710](https://doi.org/10.3390/s17122710)

[26a] P. Čížek and J. Faigl, “On localization and mapping with RGB-D sensor and hexapod walking robot in rough terrains,” in *IEEE International Conference on Systems, Man, and Cybernetics (SMC)*, 2016, pp. 2273–2278. DOI: [10.1109/SMC.2016.7844577](https://doi.org/10.1109/SMC.2016.7844577)

A. CITATIONS OF AUTHOR'S PUBLICATIONS

- A. Torres-Pardo, D. Pinto-Fernandez, M. Garabini, F. Angelini, D. Rodriguez-Cianca, S. Massardi, *et al.*, “Legged locomotion over irregular terrains: State of the art of human and robot performance,” *Bioinspiration & Biomimetics*, vol. 17, no. 6, 2022. DOI: [10.1088/1748-3190/ac92b3](https://doi.org/10.1088/1748-3190/ac92b3)

[25a] T. Fischer, T. Pire, **P. Čížek**, P. D. Cristóforis, and J. Faigl, “Stereo vision-based localization for hexapod walking robots operating in rough terrains,” in *IEEE/RSJ International Conference on Intelligent Robots and Systems (IROS)*, 2016, pp. 2492–2497. DOI: [10.1109/IROS.2016.7759388](https://doi.org/10.1109/IROS.2016.7759388)

- V. F. Vidal, L. M. Honorio, F. M. Dias, M. F. Pinto, A. L. Carvalho, and A. L. M. Marcato, “Sensors fusion and multidimensional point cloud analysis for electrical power system inspection,” *Sensors*, vol. 20, no. 14, 2020. DOI: [10.3390/s20144042](https://doi.org/10.3390/s20144042)
- H. H. Khalili, W. Cheah, T. B. Garcia-Nathan, J. Carrasco, S. Watson, and B. Lennox, “Tuning and sensitivity analysis of a hexapod state estimator,” *Robotics and Autonomous Systems*, vol. 129, p. 103 509, 2020. DOI: [10.1016/j.robot.2020.103509](https://doi.org/10.1016/j.robot.2020.103509)
- J. E. Chamorro Fuertes, J. J. Marin Arciniegas, P. Bustos Garcia de Castro, and O. A. Vivas Alban, “Locomotion control of PhantomX hexapod robot with touch-pressure sensor and RoboComp,” in *IEEE Colombian Conference on Applications of Computational Intelligence (ColCACI)*, 2020
- A. Zdesar, G. Klancar, and I. Skrjanc, “Vision-based localization of a wheeled mobile robot with a stereo camera on a pan-tilt unit,” in *International Conference on Informatics in Control, Automation and Robotics (ICINCO)*, 2019, pp. 544–551

[24a] **P. Čížek**, J. Faigl, and D. Masri, “Low-latency image processing for vision-based navigation systems,” in *IEEE International Conference on Robotics and Automation (ICRA)*, 2016, pp. 781–786. DOI: [10.1109/ICRA.2016.7487207](https://doi.org/10.1109/ICRA.2016.7487207)

- N. Hariri, H. Gutierrez, J. Rakoczy, R. Howard, and I. Bertaska, “Performance characterization of the smartphone video guidance sensor as vision-based positioning system,” *Sensors*, vol. 20, no. 18, 2020. DOI: [10.3390/s20185299](https://doi.org/10.3390/s20185299)
- D. Liu, G. Zhou, D. Zhang, X. Zhou, and C. Li, “Ground control point automatic extraction for spaceborne georeferencing based on FPGA,” *IEEE Journal of Selected Topics in Applied Earth Observations and Remote Sensing*, vol. 13, pp. 3350–3366, 2020. DOI: [10.1109/JSTARS.2020.2998838](https://doi.org/10.1109/JSTARS.2020.2998838)

[30a] T. Krajník, J. Šváb, S. Pedre, **P. Čížek**, and L. Přeučil, “FPGA-based module for SURF extraction,” *Machine Vision and Applications*, vol. 25, no. 3, pp. 787–800, 2014. DOI: [10.1007/s00138-014-0599-0](https://doi.org/10.1007/s00138-014-0599-0)

- D. Liu, G. Zhou, D. Zhang, X. Zhou, and C. Li, “Ground control point automatic extraction for spaceborne georeferencing based on FPGA,” *IEEE Journal of Selected Topics in Applied Earth Observations and Remote Sensing*, vol. 13, pp. 3350–3366, 2020. DOI: [10.1109/JSTARS.2020.2998838](https://doi.org/10.1109/JSTARS.2020.2998838)
- E. Azimi, A. Behrad, M. B. Ghaznavi-Ghouschi, and J. Shanbehzadeh, “A fully pipelined and parallel hardware architecture for real-time BRISK salient point extraction,” *Journal of Real-time Image Processing*, vol. 16, no. 5, pp. 1859–1879, 2019. DOI: [10.1007/s11554-017-0693-4](https://doi.org/10.1007/s11554-017-0693-4)
- M. Y. I. Idris, N. B. Abd Warif, H. Arof, N. M. Noor, A. W. A. Wahab, and Z. Razak, “Accelerating FPGA-SURF feature detection module by memory access reduction,” *Malaysian Journal of Computer Science*, vol. 32, no. 1, pp. 47–61, 2019. DOI: [10.22452/mjcs.vol32no1.4](https://doi.org/10.22452/mjcs.vol32no1.4)
- R. de Lima, J. Martinez-Carranza, A. Morales-Reyes, and R. Cumplido, “Improving the construction of orb through fpga-based acceleration,” *Machine Vision and Applications*, vol. 28, no. 5–6, pp. 525–537, 2017. DOI: [10.1007/s00138-017-0851-5](https://doi.org/10.1007/s00138-017-0851-5)
- J. Huang and G. Zhou, “On-board detection and matching of feature points,” *Remote Sensing*, vol. 9, no. 6, 2017. DOI: [10.3390/rs9060601](https://doi.org/10.3390/rs9060601)
- A. Luo, F. An, Y. Fujita, X. Zhang, L. Chen, and H. J. Mattausch, “Low-power coprocessor for Haar-like feature extraction with pixel-based pipelined architecture,” *Japanese Journal of Applied Physics*, vol. 56, no. 4, SI, 2017. DOI: [10.7567/JJAP.56.04CF06](https://doi.org/10.7567/JJAP.56.04CF06)
- E. Azimi, A. Behrad, M. B. Ghaznavi-Ghouschi, and J. Shanbehzadeh, “Hardware architecture for projective model calculation and false match refining using random sample consensus algorithm,” *Journal of Electronic Imaging*, vol. 25, no. 6, 2016. DOI: [10.1117/1.JEI.25.6.063014](https://doi.org/10.1117/1.JEI.25.6.063014)
- G. Lentaris, I. Stamoulias, D. Soudris, and M. Lourakis, “HW/SW codesign and FPGA acceleration of visual odometry algorithms for rover navigation on Mars,” *IEEE Transactions on Circuits and Systems for Video Technology*, vol. 26, no. 8, pp. 1563–1577, 2016. DOI: [10.1109/TCSVT.2015.2452781](https://doi.org/10.1109/TCSVT.2015.2452781)
- W. Chen, S. Ding, Z. Chai, D. He, W. Zhang, G. Zhang, *et al.*, “FPGA-based parallel implementation of SURF algorithm,” in *IEEE International Conference on Parallel and Distributed Systems*, 2016, pp. 308–315

A. CITATIONS OF AUTHOR'S PUBLICATIONS

- J. Heshmatpanah, S. Boroumand, and M. T. Masouleh, "FPGA design and implementation for real time vision applications on NTACO mobile robot," in *RSI/ISM International Conference on Robotics and Mechatronics (ICRoM)*, 2014, pp. 172–177

Short Biography

Petr Čížek (born 1990 in Prague, Czech Republic) received the Bc. and Ing. degrees in robotics and cybernetics from the Czech Technical University (CTU), Prague, Czech Republic, in 2013 and 2015, respectively. He is currently pursuing his Ph.D. degree in computer science within the Computational Robotics Laboratory (CRL), Artificial Intelligence Center, Faculty of Electrical Engineering, CTU under supervision of prof. Ing. Jan Faigl, Ph.D. In 2019–2021, he participated in the DARPA Subterranean Challenge within the team CTU-CRAS-NORLAB. His research interests are multi-legged walking robots and their locomotion control and efficient computation on Field-Programmable Gate Array (FPGA).



